STATE OF THE CLIMATE IN 2025

GLOBAL OCEANS

D. L. Volkov and R. C. Perez, Eds.

Special Online Supplement to the *Bulletin of the American Meteorological Society* Vol. 107, No. 8, August, 2026

https://doi.org/10.1175/BAMS-D-26-0100.1
Corresponding author: Denis L. Volkov / denis.volkov@noaa.gov

STATE OF THE CLIMATE IN 2025
Global Oceans

Editors

Jessica Blunden
James Reagan

Chapter Editors

Anthony Arguez
Josh Blannin
Peter Bissolli
Kyle R. Clem
Howard J. Diamond
Matthew L. Druckenmiller
Robert J. H. Dunn
Catherine Ganter
Nadine Gobron
Rodney Martinez
Twila A. Moon
Gary A. Morris
Marilyn N. Raphael
Renellys C. Perez
Carl J. Schreck III
Zewdu Segele
Laura Stevens
Richard L. Thoman
Denis L. Volkov
Zhiwei Zhu

Technical Editors

Lukas Noguchi
Laura Ohlmann

BAMS Special Editor for Climate

Timothy DelSole

American Meteorological Society

Cover Credit:
Skyline view from a research cruise in the Florida Straits, between Florida and the Bahamas, in September 2025. Photo credit: Denis L. Volkov.

How to cite this document:
Global Oceans is one chapter from the *State of the Climate in 2025* annual report and is available from https://doi.org/10.1175/BAMS-D-26-0100.1. Compiled by NOAA's National Centers for Environmental Information, *State of the Climate in 2025* is based on contributions from scientists from around the world. It provides a detailed update on global climate indicators, notable weather events, and other data collected by environmental monitoring stations and instruments located on land, water, ice, and in space. The full report is available from https://doi.org/10.1175/2026BAMSStateoftheClimate.1.

Citing the complete report:
Blunden, J.and J. Reagan, Eds., 2026: "State of the Climate in 2025". Bull. Amer. Meteor. Soc., 107 (8), Si–S512, https://doi.org/10.1175/2026BAMSStateoftheClimate.1.

Citing this chapter:
Volkov, D. L. and R. C. Perez, Eds., 2026: Global Oceans [in "State of the Climate in 2025"]. Bull. Amer. Meteor. Soc., 107 (8), S169–S228, https://doi.org/10.1175/BAMS-D-26-0100.1.

Citing a section (example):
Sharp, J. D., Z. Wang, T. Ito, S. Minobe, L. Cheng, J. Du, H. Garcia, C. J. Roach, B. Lu, Y. Xin, M. Han, Y. Zhou, and G. G. Navarra, 2026: Global ocean dissolved oxygen [in "State of the Climate in 2025"]. Bull. Amer. Meteor. Soc., 107 (8), S216–S220, https://doi.org/10.1175/BAMS-D-26-0100.1.

Editor and Author Affiliations (alphabetical by name)

Atkinson, Christopher P., Met Office Hadley Centre, Exeter, United Kingdom
Beckley, Brian, Earth Resources Technology, Inc., Greenbelt, Maryland
Carter, Brendan R., NOAA/OAR Pacific Marine Environmental Laboratory, Seattle, Washington
Cetinić, Ivona, NASA Goddard Space Flight Center, Greenbelt, Maryland; Universities Space Research Association, Columbia, Maryland
Chan, Duo, School of Ocean and Earth Science, University of Southampton, Southampton, United Kingdom
Cheng, Lijing, State Key Laboratory of Earth System Numerical Modeling and Application, Institute of Atmospheric Physics, Chinese Academy of Sciences, Beijing, China
Domingues, Catia M., Global Climate, National Oceanography Centre, Southampton, United Kingdom
Dong, Shenfu, NOAA/OAR Atlantic Oceanographic and Meteorological Laboratory, Miami, Florida
Du, Juan, International Center for Climate and Environment Sciences, Institute of Atmospheric Physics, Chinese Academy of Sciences, Beijing, China
Elipot, Shane, Rosenstiel School of Marine, Atmospheric, and Earth Science, University of Miami, Miami, Florida
Feely, Richard A., NOAA/OAR Pacific Marine Environmental Laboratory, Seattle, Washington
Franz, Bryan A., NASA Goddard Space Flight Center, Greenbelt, Maryland
Fu, Yao, College of Marine Science, University of South Florida, St. Petersburg, Florida
Gao, Meng, NASA Goddard Space Flight Center, Greenbelt, Maryland; Science Systems and Applications, Inc., Lanham, Maryland
Garcia, Hernan, NOAA/NESDIS National Centers for Environmental Information, Silver Spring, Maryland
Graham, Garrett, North Carolina Institute for Climate Studies, North Carolina State University, Asheville, North Carolina
Hamlington, Benjamin D., Jet Propulsion Laboratory, California Institute of Technology, Pasadena, California
Han, Mingyu, School of Oceanography, Shanghai Jiao Tong University, Shanghai, China
Hobbs, Will, Australian Antarctic Program Partnership (AAPP), Hobart, Tasmania, Australia; Institute for Marine and Antarctic Studies, University of Tasmania, Hobart, Tasmania, Australia
Hu, Zeng-Zhen, NOAA/NWS National Centers for Environmental Prediction Climate Prediction Center, College Park, Maryland
Huang, Boyin, NOAA/NESDIS National Centers for Environmental Information, Asheville, North Carolina
Ito, Takamitsu, School of Earth and Atmospheric Sciences, Georgia Institute of Technology, Atlanta, Georgia
Jersild, Annika, Earth System Science Interdisciplinary Center/Cooperative Institute for Satellite Earth System Studies, University of Maryland, College Park, Maryland
Jevrejeva, Svetlana, National Oceanography Centre, Liverpool, United Kingdom
Johnson, Gregory C., NOAA/OAR Pacific Marine Environmental Laboratory, Seattle, Washington; School of Oceanography, University of Washington, Seattle, Washington
Killick, Rachel. E., Met Office Hadley Centre, Exeter, United Kingdom
Landerer, Felix W., Jet Propulsion Laboratory, California Institute of Technology, Pasadena, California
Landschützer, Peter, Flanders Marine Institute, InnovOcean Campus, Ostend, Belgium
Le Hénaff, Matthieu, NOAA/OAR Atlantic Oceanographic and Meteorological Laboratory, Miami, Florida
Leuliette, Eric, NOAA/NWS NCWCP Laboratory for Satellite Altimetry, College Park, Maryland
Locarnini, Ricardo, NOAA/NESDIS National Centers for Environmental Information, Silver Spring, Maryland
Lozier, M. Susan, School of Earth and Atmospheric Sciences, Georgia Institute of Technology, Atlanta, Georgia
Lu, Bin, School of Information Science and Electronic Engineering, Shanghai Jiao Tong University, Shanghai, China
Lyman, John M., Cooperative Institute for Marine and Atmospheric Research, University of Hawaii, Honolulu, Hawaii; NOAA/OAR Pacific Marine Environmental Laboratory, Seattle, Washington
Minobe, Shoshiro, Faculty of Science, Hokkaido University, Sapporo, Japan
Mishonov, Alexey, Earth System Science Interdisciplinary Center/Cooperative Institute for Satellite Earth System Studies, University of Maryland, College Park, Maryland; NOAA/NESDIS National Centers for Environmental Information, Silver Spring, Maryland
Mitchum, Gary T., College of Marine Science, University of South Florida, St. Petersburg, Florida
Miyamoto, Masatoshi, Japan Meteorological Agency, Tokyo, Japan
Moat, Ben I., National Oceanography Centre, Southampton, United Kingdom
Monselesan, Didier P., CSIRO, Environment Research Unit, Climate Intelligence, Climate Variability and Hazards, Hobart, Tasmania, Australia
Navarra, Gian G., Atmospheric and Oceanic Sciences, Princeton University, Princeton, New Jersey
Nerem, R. Steven, Colorado Center for Astrodynamics Research, Cooperative Institute for Research in Environmental Sciences, University of Colorado Boulder, Boulder, Colorado
Perez, Renellys C., NOAA/OAR Atlantic Oceanographic and Meteorological Laboratory, Miami, Florida
Petit, Tyllis, National Oceanography Centre, Southampton, United Kingdom
Reagan, James, NOAA/NESDIS National Centers for Environmental Information, Silver Spring, Maryland
Roach, Christopher J., Institute for Marine and Antarctic Studies, University of Tasmania, Hobart, Tasmania, Australia
Savita, Abhishek, Centre for Atmospheric Sciences, Indian Institute of Technology Delhi, Delhi, India
Schlegel, Robert W., Laboratoire d'Océanographie de Villefranche, Sorbonne Université, Villefranche-sur-mer, France
Sharp, Jonathan D., Cooperative Institute for Climate, Ocean, and Ecosystem Studies, University of Washington, Seattle, Washington; NOAA/OAR Pacific Marine Environmental Laboratory, Seattle, Washington
Smeed, David A., National Oceanography Centre, Southampton, United Kingdom
Stackhouse, Paul W., NASA Langley Research Center, Hampton, Virginia
Steinberg, Jacob M., NOAA/OAR Geophysical Fluid Dynamics Laboratory, Princeton, New Jersey
Sweet, William, NOAA/NOS Center for Operational Oceanographic Products and Services, Silver Spring, Maryland
Thompson, Philip R., Cooperative Institute for Marine and Atmospheric Research, Department of Oceanography, University of Hawaii, Honolulu, Hawaii
Trinanes, Joaquin, Department of Electronics and Computer Science, Universidad de Santiago de Compostela, Santiago, Spain
Tuchen, Franz Philip, Rosenstiel School of Marine, Atmospheric, and Earth Science, University of Miami, Miami, Florida
Volkov, Denis L., Cooperative Institute for Marine and Atmospheric Studies, Rosenstiel School of Marine, Atmospheric, and Earth Science, University of Miami, Miami, Florida; NOAA/OAR Atlantic Oceanographic and Meteorological Laboratory, Miami, Florida
Wang, Zhankun, NOAA/NESDIS National Centers for Environmental Information, Dickinson, Texas
Wanninkhof, Rik, NOAA/OAR Atlantic Oceanographic and Meteorological Laboratory, Miami, Florida
Weller, Robert A., Department of Physical Oceanography, Woods Hole Oceanographic Institution, Woods Hole, Massachusetts
Westberry, Toby K., Oregon State University, Corvallis, Oregon

Editor and Author Affiliations (continued)

Widlansky, Matthew J., Cooperative Institute for Marine and Atmospheric Research, Department of Oceanography, University of Hawaii, Honolulu, Hawaii

Wijffels, Susan E., Department of Physical Oceanography, Woods Hole Oceanographic Institution, Woods Hole, Massachusetts

Willis, Joshua K., Jet Propulsion Laboratory, California Institute of Technology, Pasadena, California

Xin, Yi, School of Information Science and Electronic Engineering, Shanghai Jiao Tong University, Shanghai, China

Yin, Xungang, NOAA/NESDIS National Centers for Environmental Information, Asheville, North Carolina

Yu, Lisan, Department of Physical Oceanography, Woods Hole Oceanographic Institution, Woods Hole, Massachusetts

Zhou, Yuntao, School of Oceanography, Shanghai Jiao Tong University, Shanghai, China

Editorial and Production Team

Allen, Jessicca, Graphics Support, Cooperative Institute for Satellite Earth System Studies, North Carolina State University, Asheville, North Carolina

Camper, Amy V., Graphics Support, Innovative Consulting and Management Services, LLC, NOAA/NESDIS National Centers for Environmental Information, Asheville, North Carolina

Carroll, Lauren, Content Team Lead, Communications and Outreach, NOAA/NESDIS National Centers for Environmental Information, Asheville, North Carolina

Crossman, Jacquelyn, NCEI Librarian, MPF-ZAI, NOAA/NESDIS National Centers for Environmental Information, Asheville, North Carolina

Haley, Bridgette O., Graphics Support, NOAA/NESDIS National Centers for Environmental Information, Asheville, North Carolina

Noguchi, Lukas, Technical Editor, Innovative Consulting and Management Services, LLC, NOAA/NESDIS National Centers for Environmental Information, Asheville, North Carolina

Ohlmann, Laura, Technical Editor, Innovative Consulting and Management Services, LLC, NOAA/NESDIS National Centers for Environmental Information, Asheville, North Carolina

Veasey, Sara W., Visual Communications Team Lead, Communications and Outreach, NOAA/NESDIS National Centers for Environmental Information, Asheville, North Carolina

3. Table of Contents

3. GLOBAL OCEANS

D. L. Volkov and R. C. Perez, Eds.

a. Overview

—D. L. Volkov and R. C. Perez

This chapter synthesizes changes in the ocean's physical state and key biogeochemical indicators during 2025, highlighting the persistence of exceptional warmth following the record-breaking years of 2023 and 2024 and the continued influence of large-scale climate variability, particularly the El Niño–Southern Oscillation (ENSO). The strong El Niño that developed in 2023 and weakened through the spring of 2024, transitioned towards La Niña conditions by the second half of 2024 (see section 4b). Weak La Niña was prevalent for most of 2025 except later spring/summer when neutral conditions dominated. This transition influenced ocean–atmosphere exchanges, the redistribution of heat, freshwater, and momentum across ocean basins while the long-term warming trend continued.

Air–sea fluxes in 2025 reflected ongoing ocean heat uptake and ENSO-related variability. Compared to 2024, heat gain increased notably in the tropics and subtropics. Freshwater flux patterns were shaped by the developing La Niña conditions, with increased precipitation and freshening near the Maritime Continent and western tropical Pacific and enhanced freshwater loss and salinification across the central and eastern equatorial Pacific. These changes were driven mainly by precipitation anomalies rather than evaporation. Wind stress anomalies were generally weak in the tropics but showed strengthened westerlies in the Southern Ocean and North Atlantic and weaker winds over parts of the North Pacific, influencing regional circulation and wind-driven vertical velocity.

Global sea surface temperatures (SSTs) remained exceptionally high in 2025, marking the third consecutive year of extreme ocean warmth. Long-term warming has accelerated, increasing from approximately 0.12°C per decade over 1950–2025 to about 0.21°C per decade since 2000. Although the shift toward neutral and weak La Niña conditions produced some cooling in the tropical Pacific compared to the peak warmth of 2023/24, global SSTs remained elevated due to the continued accumulation of heat in the climate system. Marine heatwaves remained widespread, affecting about 87% of the ocean surface. While heatwave occurrence declined slightly relative to 2024, 2025 remained among the highest occurrence years on record. In contrast, marine cold spells became even less frequent, reaching their lowest occurrence in the observational record and highlighting the continued shift toward warmer ocean conditions.

Ocean heat content also remained at record highs, with continued warming in the upper 2000 m and detectable warming extending into deeper layers. The transition from El Niño to weak La Niña conditions redistributed heat within the tropical Pacific, reducing heat content in the eastern equatorial Pacific and increasing it in the western and central equatorial Pacific, but did not offset the long-term warming trend. Most ocean basins remained warmer than average. The Atlantic Ocean continued to exhibit widespread warm anomalies, though slightly cooler than the extreme conditions of 2024. The Indian Ocean remained warmer than the climatological average despite localized cooling in the southwestern Indian Ocean compared to 2024. The sustained heat uptake by the oceans contributes to accelerated sea level rise, enhanced tropical cyclone activity, amplified stratification, and increased marine heatwaves.

Ocean salinity patterns reflected both interannual variability and long-term hydrological changes. The equatorial Pacific generally became saltier under La Niña-related precipitation shifts, while high-latitude regions of the Atlantic experienced freshening that may influence deep water formation and overturning circulation. The Indian Ocean exhibited mixed salinity changes, with both freshening and salinification depending on location, and shifted from anomalously fresh to slightly salty relative to climatology. Subsurface salinity changes were most pronounced in the upper few hundred meters and varied by basin. Despite these interannual fluctuations, long-term trends remain consistent with an intensifying global hydrological cycle, in which salty regions become saltier and fresh regions fresher.

Global mean sea level reached a new record high in 2025, rising to 111.2 mm above the 1993 baseline and continuing a long-term increase of about 3.5 mm per year, with clear acceleration over recent decades. Although ocean warming drove a substantial thermosteric increase, the total annual rise from 2024 to 2025 was relatively modest, likely due to La Niña-related redistribution of water between the ocean and land. Regional patterns reflected ENSO-driven circulation changes, with lower sea levels in the central and eastern tropical Pacific and higher levels in the Indo–western Pacific. Long-term sea level rise continues to increase the frequency and severity of coastal flooding and extreme sea level events.

Ocean circulation patterns in 2025 showed strong regional variability linked to ENSO and atmospheric forcing. Surface currents in the equatorial Pacific exhibited enhanced westward flow associated with developing La Niña conditions, while the Kuroshio Extension remained displaced northward of its long-term mean position. Seasonal monsoon forcing drove pronounced circulation changes in the Indian Ocean, and variability in the Atlantic reflected regional climate modes. The Atlantic meridional overturning circulation continued to exhibit strong interannual variability, with some evidence of localized weakening in the subtropical North Atlantic and strengthening in the subtropical South Atlantic, but limited evidence of a long-term basin-wide decline.

The global ocean continues to play a major role in the global carbon cycle by absorbing approximately 29% of anthropogenic carbon dioxide emissions and helping slow its atmospheric accumulation, while contributing to ocean acidification. The oceanic uptake of carbon dioxide in 2025 increased compared to the prior decade. Despite regional variability and observational uncertainties, the ocean carbon sink remains strong and continues to increase. Satellite observations showed that global phytoplankton biomass and distribution in 2025 remained largely within historical ranges, with modest productivity increases in the tropical Pacific associated with weak La Niña conditions.

This year's report features a new section on dissolved oxygen, which is an essential climate variable, especially for marine ecosystems and biogeochemical cycling. In 2025, global ocean dissolved oxygen continued to decline, with inventories decreasing by about 0.45% per decade since 1965 due to warming, reduced ventilation, ocean circulation changes, and enhanced biological respiration. An ensemble of statistical and machine-learning analyses confirms widespread deoxygenation, especially in the North Pacific and Southern Oceans, with broadly negative oxygen anomalies in 2025 consistent with elevated ocean heat content and ENSO-driven variability.

Overall, the ocean in 2025 remained in a state of persistent change. Record-high global sea level, high SSTs and heat content, widespread marine heatwaves, and continued carbon uptake and deoxygenation highlight the ocean's central role in regulating Earth's climate.

b. Sea surface temperature

—X. Yin, R. W. Schlegel, B. Huang, D. Chan, G. Graham, and Z.-Z. Hu

1. INTRODUCTION

The state of sea surface temperatures (SSTs) in global oceans and seas in 2025 was analyzed using four gridded SST datasets: Daily Optimum Interpolation SST version 2.1 (DOISSTv2.1; Huang et al. 2021), Extended Reconstructed SST version 5 (ERSSTv5; Huang et al. 2017), Hadley Centre SST version 4 (HadSST.4.2.0.0; Kennedy et al. 2019), and Dynamically Consistent ENsemble of Temperature version 1.1.0.0 (DCENT-Iv1.1.0.0; Chan et al. 2026). DOISSTv2.1 is a blended product from in situ observations and satellite measurements, covering the period since late 1981, when satellite-retrieved SSTs became available. It provides daily mean SSTs and is analyzed on 0.25° latitude–longitude grids. The latter three datasets are in situ observation-based products, providing the longest available global SST records with monthly mean values extending back to preindustrial times, beginning in 1854 for ERSSTv5, 1850 for HadSST.4.2.0.0 and DCENT-Iv1.1.0.0, to present, when shipborne instrumental measurements of water temperature were deemed sufficiently extensive and reliable to support global SST analyses. The horizontal resolution is 2° for ERSSTv5 and 5° for HadSST.4.2.0.0 and DCENT-Iv1.1.0.0.

Marine heatwaves (MHWs) are defined as periods of five or more consecutive days with SSTs above the 90th percentile daily climatological values (Hobday et al. 2016). A MHW is categorized as Moderate (Category 1) when the greatest SST anomaly (SSTA) during the event is between one and two times the difference between the 90th percentile and the seasonal climatology. When this value is more than two, three, or four times of the difference, the MHW is categorized as Strong (Category 2), Severe (Category 3), or Extreme (Category 4), respectively (Hobday et al. 2018). The direct inverse of MHWs (i.e., days below the 10th percentile) is used to define and categorize marine cold spells (MCSs), with an additional 'ice' category for days when the daily climatology is below –1.7°C (Schlegel et al. 2021). An interactive visualization of global MHW and MCS coverage from 1982 to the present with DOISSTv2.1 is available at https://www.marineheatwaves.org/tracker.html.

In this report, the higher-resolution dataset DOISSTv2.1 is primarily used to examine daily SST variations and evaluate MHW/MCS occurrences, while the coarser-resolution but long-term datasets ERSSTv5, HadSST.4.0.1.0, and DCENT-Iv1.1.0.0 are used for large-scale SST pattern analysis and decadal-to-centennial SST trend assessment. The base period for computing SSTAs and analyzing MHWs/MCSs is 1991–2020, the current standard reference period for SST climate normals (Yin et al. 2024).

2. SEA SURFACE TEMPERATURES IN 2025

For the global ocean, recent strong warming manifested as historically high SSTs that began in March 2023 have persisted, making 2025 the third consecutive exceptionally warm year. Figure 3.1 shows the daily global-mean SST for each year since 1981 in DOISSTv2.1. The 1991–2020 normal SSTs and the corresponding ±1.96-standard deviation (std. dev.) envelope (Yin et al. 2024) are also shown for reference. The envelope represents the 95% confidence interval of the normal SSTs, corresponding to a 5% significance level when assessing departures of observed SSTs from normal conditions.

Although the daily global-mean SST in 2025 did not set new records as in the previous two years, it remained remarkable, ranking as the second or third highest during most

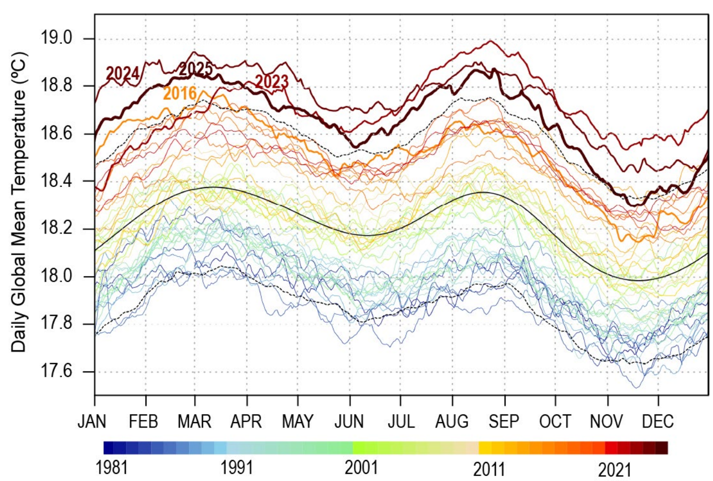

Fig. 3.1. Daily global-mean sea surface temperatures (SST) since 1981. Individual years are shown in different colors, as indicated by the color bar, plotted over a common 366-day Julian calendar year. The current year and the recent record-setting years (2016, 2023, and 2024) are highlighted with thicker lines and labeled. The solid and dashed black lines denote the 1991–2020 normal SST and the ±1.96-std. dev. envelope (95% confidence interval), respectively. (Source: Daily OISST [DOISSTv2.1].)

of the year. Consistent with the climatological seasonal cycle, daily global-mean SST reached maxima in early March and late August and minima in early June and mid-November. From January through late March, the 2025 global-mean SST was second only to the 2024 mean and remained substantially higher than in all other previous years, including the record-breaking years of 2016 and 2023. Between April and May, global-mean SSTs in 2025 and 2023 were comparable, alternating between the second- and third-highest positions for that time of year. Since early June, global-mean SSTs in 2025 were lower than in the previous two years for nearly the remainder of the year. During most of November and December, 2025 SSTs fell outside the top three highest for the time of year.

In 2025, the highest daily global-mean SST was 18.87°C, recorded on 26 August, ranking as the second highest for that time of year after 2024. The lowest daily global-mean SST, 18.30°C, was observed on 17 November, ranking as the fourth highest for that time of year, following 2023, 2024, and 2016. Figure 3.1 also shows that SSTs during the last three years were distinct from those in earlier years. With the exception of a few intermittent periods in November and December, the 2025 global-mean SST lay outside the ±1.96-std. dev. envelope of the 1991–2020 normal. Indeed, global-mean SST remained continuously more than 1.96 std. devs. above the 1991–2020 normal from mid-March 2023 through early November 2025, indicating an unusually warm global ocean for three consecutive years.

In the centennial record of ERSSTv5, the annual-average global-mean SST for 2025 was 18.68°C, which was 0.87°C higher than the 1854–1900 pre-industrial level and 0.38°C above the 1991–2020 reference level. Within the 172-year SST record beginning 1854, 2025 ranked as the third warmest year, 0.03°C cooler than 2023 and 0.09°C cooler than 2024, but 0.10°C warmer than 2016, the fourth warmest year. Moreover, the most recent decade (2016–25) was the warmest on record, with an average SST of 18.57°C, 0.77°C above the pre-industrial level and 0.27°C above the 1991–2020 reference level.

Changes of global SST in 2025 relative to the 1991–2020 reference period are shown in Fig. 3.2. On the annual mean (Fig. 3.2a), 2025 SSTs were characterized by ENSO-related patterns in the tropics, enhanced SST contrasts in the Northern Hemisphere, and comparatively lower variability in the Southern Hemisphere. In the equatorial Pacific, SSTs were lower than the reference period by less than 0.5°C between 170°E and 90°W and slightly higher than the reference period off the western coast of the Americas, consistent with the evolution from ENSO-neutral to La Niña-like conditions during 2025 (see section 4b; Tan et al. 2025). Across the remaining ocean basins, warm anomalies predominated, with scattered pockets of cold anomalies. Particularly large positive SSTAs (>+1.0°C) occurred in the midlatitude eastern and central North Pacific, the western Mediterranean Sea, the central Maritime Continent, the North Sea, and the Barents Sea. The seasonal evolution of global SST patterns is further illustrated using seasonal-mean SSTs (Figs. 3.2b–e). Here, the four seasons are defined as boreal winter (January–March), spring (April–June), summer (July–September), and autumn (October–December), corresponding to austral summer, autumn, winter, and spring, respectively.

As shown in Fig. 3.2, cooling in the central equatorial Pacific was most pronounced in boreal winter and autumn, with large areas exhibiting SSTs more than 0.5°C below the 1991–2020 average, suggesting that La Niña conditions briefly developed during these two seasons (see section 4b; Tan et al. 2025). Cooling in the Arabian Sea was observed in all seasons and was strongest in autumn, when negative SSTAs extended across nearly the entire basin. The Arctic Ocean exhibited relatively minor variability in winter and spring because of extensive ice coverage. However, SSTAs in the Barents Sea remained above normal throughout the year, while cooling occurred across much of the Beaufort Sea in summer and subsequently extended into the East Siberian Sea in autumn. Globally, ocean warming peaked in the Northern Hemisphere during summer (Fig. 3.2d). In contrast, the Southern Hemisphere exhibited comparatively weaker seasonal variability, with stronger warming during austral summer (Fig. 3.2b). Meanwhile, persistent positive SSTAs in the midlatitude North Pacific indicated that the Pacific Decadal Oscillation (PDO) maintained a five-year negative phase since 2020 (NOAA National Centers for Environmental Information 2026). In addition, the seasonal SSTA pattern in the Indian Ocean suggests that the

Indian Ocean dipole (IOD) was in a negative phase during boreal summer and autumn of 2025 (see section 4f for details; NOAA Climate Prediction Center 2026). For most of the year, the equatorial Atlantic was warm, with weak cooling associated with a short-lived Atlantic Niña event from June to August 2025.

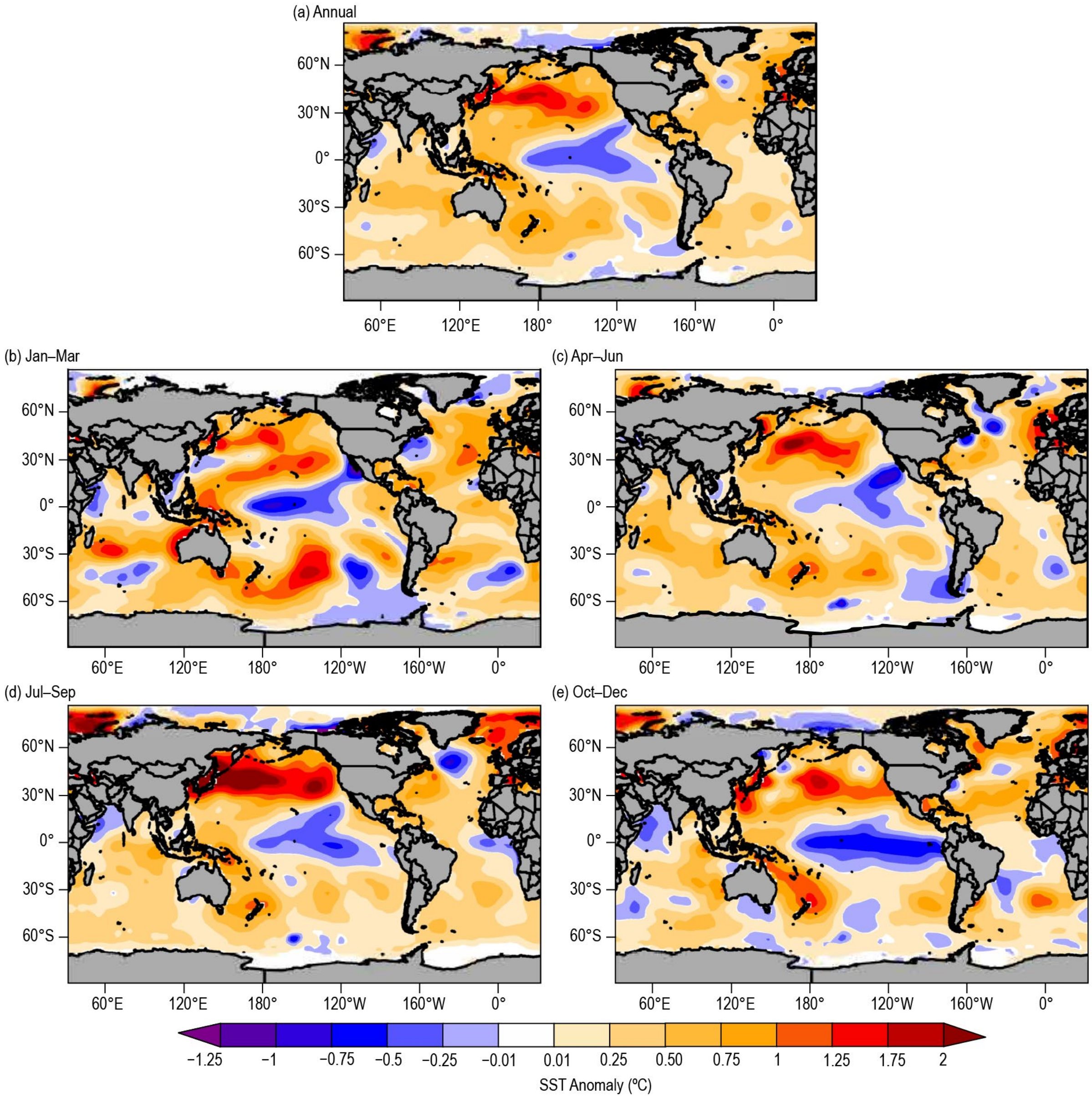

Fig. 3.2. Annual and seasonal mean sea surface temperature anomalies (SSTAs; °C) for 2025 relative to the 1991–2020 reference period. (a) Annual; (b) boreal winter (Jan–Mar); (c) spring (Apr–Jun); (d) summer (Jul–Sep); and (e) autumn (Oct–Dec). (Source: ERSSTv5.)

3. MARINE HEATWAVES AND COLD SPELLS

The 2025 analysis of DOISSTv2.1 indicates that 87% of the ocean surface experienced at least one marine heatwave (MHW; Hobday et al. 2016; Figs. 3.3a,b), while 26% experienced at least one marine cold spell (MCS; Figs. 3.3c,d). The most common MHW category in 2025 was Category 1 (Moderate), accounting for 40% of the total coverage, followed by Category 2 (Strong) events at 39%, with Category 3 (Severe) and Category 4 (Extreme) MHWs accounting for 6% and 2% of the total coverage, respectively. Category 1 (Moderate) MCSs remained the most prevalent cool events (17% in 2025), as has been the case since 2001. Globally, the ocean experienced an average of 73 MHW days and 5 MCS days in 2025. Although this is below the record high 100 MHW days observed in 2024 (and the MCS record high of 57 days in 1985; Figs. 3.3a,c), 2025 conditions correspond to a daily mean MHW coverage of 20% of the ocean surface, compared to about 1% for MCSs (Figs. 3.3a,c), making 2025 the new record-low year for MCSs.

With the transition from El Niño conditions in 2023/24 to La Niña conditions in 2024/25 (see section 4b; Tan et al. 2025), all MHW occurrences declined from 2024 to 2025. Nevertheless, 2025 still experienced more MHW activity than the previous record-setting year of 2016, ranking as the third highest year for daily MHW coverage after 2023 and 2024 (Fig. 3.3a).

While much of the Arctic experienced Category 4 MHW conditions during the first two months of the year, the absolute SST anomaly relative to the historical record was about +0.5°C. A recurring pattern of large MHWs with central cores reaching Category 4 affected the southwest coast of New Zealand from mid-February to mid-March. The northeastern region of the archipelago experienced another extensive MHW in November, again featuring a Category 4 core. As in 2024, waters surrounding Ireland and the United Kingdom were affected by Category 1 and 2 MHWs for much of the year.

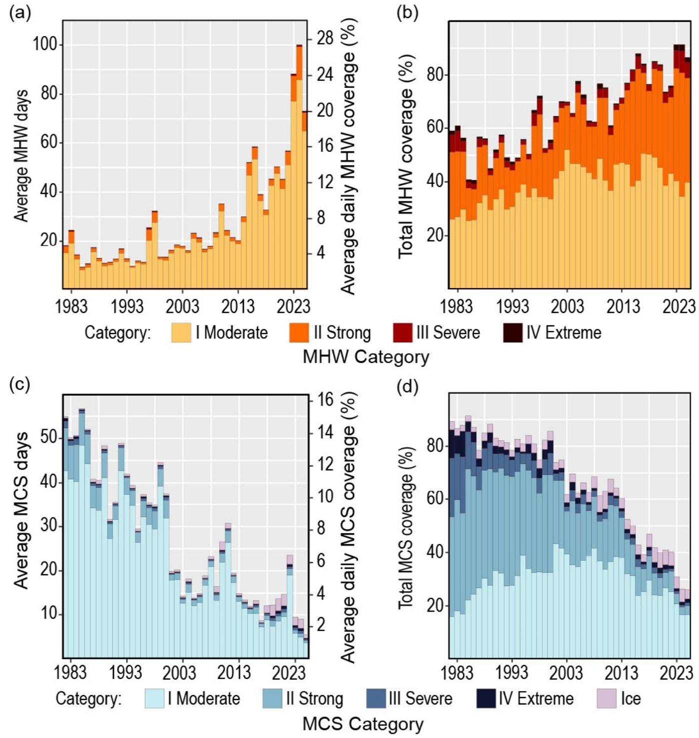

Fig. 3.3. Annual global occurrence (a),(b) of marine heatwaves (MHW) and (c),(d) marine cold spells (MCS) relative to the 1991–2020 base period. (a) Average count of MHW days experienced over the surface of the ocean each year (left y-axis), also expressed as the percent of the surface of the ocean experiencing a MHW on any given day (right y-axis) of that year; (b) total percent of the surface area of the ocean that experienced a MHW at some point during the year; (c) same as (a) but for MCS; and (d) same as (b) but for MCS. Values shown are for the highest category of MHW/MCS experienced at any point. (Source: Daily OISST [DOISSTv2.1].)

The spatial extent of this event affected much of the Atlantic coastline of Spain and France. Although short-lived, this otherwise mild MHW intensified in mid-May, with uninterrupted Category 3 conditions extending from the north of Iceland to the southern tip of Ireland. In 2025, the western Mediterranean experienced record-breaking warming during the first half of boreal summer (surpassing the previous record set in 2022). In contrast, the eastern Mediterranean was less warm in summer 2025 than in previous summers, although Category 3 MHW conditions occurred during the first two months of the year. Waters east and west of the Japanese archipelago reached Category 3 intensity beginning in July, persisting mainly as Category 2 and 3 events through October. This feature would occasionally connect across the Pacific to the 'blob-like' MHW that occurred along the west coast of North America (a now semi-permanent feature), whose most intense point was reached in mid-September with a near-basin scale core of Category 3 MHW coverage. In late July, the majority of the waters from Norway to the Arctic ice edge experienced a Category 2 MHW lasting one month. Meanwhile, the recurring summer Category 4 MHW across the Barents and Kara Seas reached its highest intensity since its annual reappearance began in 2015.

Although many other MHWs in 2025 would have been considered noteworthy a decade ago, none were as pronounced as those highlighted here. While the ocean experienced less extreme heat events in 2025 than in 2024, it did not experience correspondingly more extreme cold spells. All occurrences of MCSs declined relative to the previous year, indicating an upward shift in the overall SST envelope of the global ocean. No notable MCSs occurred in 2025; all Category 3 or 4 events were associated with cyclonic or anticyclonic eddy activity in western boundary currents or potential ice-edge-related artefacts.

4. SEA SURFACE TEMPERATURE TRENDS

Time series of global- and regional-mean annual SSTAs for the periods 1880–2025 and 1950–2025 are shown in Fig. 3.4. Uncertainty estimates derived from the ERSSTv5 ensemble analysis (Huang et al. 2015, 2020) are included for reference. Across all domains, the four SST datasets exhibit similar temporal variability and comparable trends; however, both variability and trends differ substantially among regions. Notably, North Atlantic SSTAs display pronounced interdecadal variability over the full record since 1880 (Fig. 3.4f), largely associated with the Atlantic Multidecadal Variability (Schlesinger and Ramankutty 1994).

Uncertainties are largest during the early part of the record, with substantial spreads among datasets, as illustrated for the global ocean (Fig. 3.4b) and the North Atlantic (Fig. 3.4f). This is because in situ observations were scarce in the early years, and different data reconstruction algorithms based on limited observations led to higher uncertainties in each SST reconstruction.

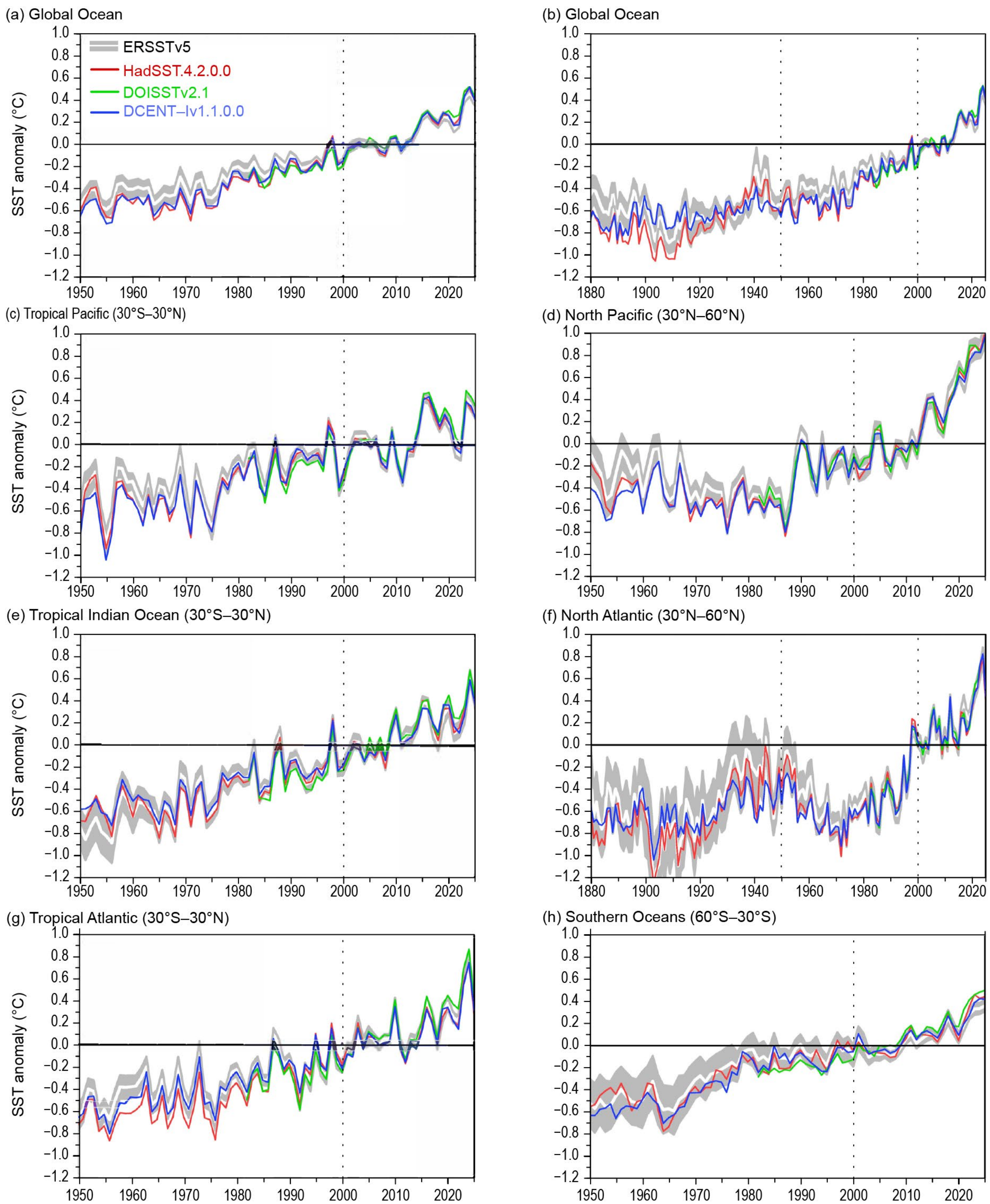

Fig. 3.4. Regional mean annual average sea surface temperature anomalies (SSTAs; °C) of ERSSTv5 (solid white), Hadley Centre Sea Surface Temperature dataset (HadSST.4.2.0.0; solid red), Daily OISST (DOISSTv2.1; solid green), and Dynamically Consistent ENsemble of Temperature (DCENT-Iv1.1.0.0; solid blue) for the period 1950–2025 except for (b) and (f). (a) Global Ocean; (b) Global Ocean for 1880–2025; (c) Tropical Pacific; (d) North Pacific; (e) Tropical Indian; (f) North Atlantic for 1880–2025; (g) Tropical Atlantic; and (h) Southern Oceans. Shadings provide the 2-std. dev. envelope derived from a 500-member ensemble analysis based on ERSSTv5 and centered on the SSTAs of ERSSTv5. The starting years of the two periods for trend assessment, 1950 and 2000, are indicated by vertical dotted black lines.

The gradual improvement of the observing network since World War II, and especially the widespread use of buoy data since the 1980s, greatly reduced SST uncertainties and narrowed the differences among datasets.

Trends in global-mean SST were evaluated for a longer period (1950–2025) and a shorter period (2000–25) using the four datasets (Table 3.1). For both periods, the estimated trends are consistent across datasets. During 1950–2025 (excluding DOISSTv2.1, which began in 1981), global trends range from 0.11°C to 0.13°C decade^{-1}, with small uncertainties between 0.01°C and 0.02°C decade^{-1}. During 2000–25, trends increased to 0.19°C–0.22°C decade^{-1} in all four products, with larger uncertainties of 0.05°C–0.06°C decade^{-1}. Accounting for uncertainties, all datasets show statistically the same trends for the two periods, with average trends of 0.12°C decade^{-1} in 1950–2025 and 0.21°C decade^{-1} for 2000–25.

Regional trends were also assessed for the six domains shown in Fig. 3.4 using ERSSTv5 (Table 3.1). For 1950–2025, trends are broadly similar across regions, ranging from 0.10°C to 0.14°C decade^{-1}, consistent with the global trends in the four datasets (0.11°C–0.13°C decade^{-1}) over the same period. In contrast, trends for 2000–25 show pronounced regional differences, spanning from 0.15°C decade^{-1} in the tropical Pacific and 0.16°C decade^{-1} in the Southern Ocean to 0.46°C decade^{-1} in the North Pacific, consistent with accelerated warming in that basin since 2013 (Hu et al. 2024). Trends in the tropical Indian Ocean (0.20°C decade^{-1}), North Atlantic (0.24°C decade^{-1}), and tropical Atlantic (0.21°C decade^{-1}) are close to the global trends (0.19°C–0.22°C decade^{-1}). Although all regional trends are statistically significant, their relative uncertainties are generally larger than those of global trends. Notably, the tropical Pacific exhibits both the weakest trend (0.15°C decade^{-1}) among all regions but the highest uncertainty (0.12°C decade^{-1}), reflecting comparatively weak warming and higher variability in the region, which is associated with the weak La Niña conditions that appeared at the beginning and end of the year (see section 4b).

Table 3.1. Linear trends (°C decade^{-1}) of global and regional mean annual sea surface temperature anomalies (SSTAs; °C) from ERSSTv5, the Hadley Centre Sea Surface Temperature Dataset version 4 (HadSST.4.2.0.0), the Dynamically Consistent ENsemble of Temperature (DCENT-Iv1.1.0.0), and the Daily OISST (DOISSTv2.1). The uncertainties at a 95% confidence level, expressed as ± values, are estimated by accounting for the effective sampling number quantified by lag–1 autocorrelation on the degrees of freedom of annual mean SSTAs.

Product	Region	1950–2025	2000–25
DCENT-Iv1.1.0.0	Global	0.13±0.01	0.20±0.06
HadSST.4.2.0.0	Global	0.13±0.02	0.21±0.06
DOISSTv2.1	Global	N/A	0.22±0.05
ERSSTv5	Global	0.11±0.01	0.19±0.06
ERSSTv5	Tropical Pacific (30°S–30°N)	0.10±0.02	0.15±0.12
ERSSTv5	North Pacific (30°N–60°N)	0.12±0.05	0.46±0.11
ERSSTv5	Tropical Indian (30°S–30°N)	0.14±0.02	0.20±0.07
ERSSTv5	North Atlantic (30°N–60°N)	0.13±0.05	0.24±0.10
ERSSTv5	Tropical Atlantic (30°S–30°N)	0.12±0.02	0.21±0.09
ERSSTv5	Southern oceans (30°S–60°S)	0.10±0.01	0.16±0.05

c. Ocean temperature and heat content

—G. C. Johnson, J. M. Lyman, C. P. Atkinson, L. Cheng, C. M. Domingues, R. E. Killick, R. Locarnini, A. Mishonov, D. P. Monselesan, M. Miyamoto, J. Reagan, A. Savita, and S. E. Wijffels

The oceans transport substantial amounts of heat within Earth's climate system (e.g., Donohoe et al. 2024) and act as the dominant heat sink, absorbing ~89% of the excess energy associated with Earth's top-of-atmosphere energy imbalance from 1971 to 2020 (e.g., von Schuckmann et al. 2023). This imbalance, driven by increasing greenhouse gas concentrations and the large thermal inertia of the oceans, substantially delays global warming (e.g., Forster et al. 2025). Surface-intensified ocean warming has increased the strength and duration of marine heatwaves (MHWs; e.g., Oliver et al. 2021) and enhanced upper ocean stratification (e.g., Li et al. 2020). This substantial upper ocean warming provides additional energy to fuel stronger tropical cyclones (e.g., Walsh et al. 2016), accelerates ice loss where the cryosphere interacts with the ocean (von Schuckmann et al. 2023), and exacerbates coral bleaching (e.g., Hughes et al. 2017). Subsurface ocean warming also contributes to sea level rise (section 3f).

Here, we discuss ocean temperature and heat content anomalies in 2025 relative to both 2024 and a 30-year climatology (1993–2022). We focus primarily on the upper 2 km of the ocean, but also update an estimate of decadal temperature trends for the deep (2 km–4 km) and abyssal (4 km–6 km) layers, where warming is also detected. To do this, we generated weekly maps of ocean heat content anomaly (OHCA) relative to a 1993–2022 baseline mean as well as temperature fields on 58 pressure layers from 0 dbar to 2000 dbar using Random Forest regression following Lyman and Johnson (2023), with V2.2 methodological improvements (https://www.pmel.noaa.gov/rfrom/). In situ ocean temperature profiles, including Argo data downloaded from an Argo Global Data Assembly Centre in January 2026 (http://doi.org/10.17882/42182#125185), were used for training data for these maps, and prediction variables included satellite sea surface height and SST, location, and time. Multidecadal time series of annual global estimates of OHCA using primarily in situ data for two depth layers (0 m–700 m and 700 m–2000 m) from multiple research groups are also discussed. Finally, a deep subset of these same Argo data is used along with shipboard conductivity, temperature, and depth (CTD) data downloaded from the World Ocean Database (Mishonov et al. 2024; https://www.ncei.noaa.gov/products/world-ocean-database) in January 2026 to update a 2000 dbar–6000 dbar multidecadal estimate of deep and abyssal ocean temperature trends following Johnson and Purkey (2024).

The boreal winter of 2023/24 marked an El Niño year, but the winters of 2024/25 and marginally 2025/26 both exhibited weak La Niña conditions (see section 4b). Consistent with this history, the 2025-minus-2024 difference of 0-m–2000-m OHCA (Fig. 3.5b) generally shows a decrease in the eastern tropical Pacific and an increase in the west, with ocean heat content anomalies for 2025 (Fig. 3.5a) being above the 30-year climatological conditions in the western tropical Pacific and below that climatology in much of the eastern tropical Pacific. As in 2020 through 2024, the centers of the North and South Pacific continued to be anomalously warm in 2025, with less warm conditions around the edges, consistent with a continued negative Interdecadal Pacific Oscillation index (Henley et al. 2015). As in 2022 through 2024, cold anomalies just south of the Kuroshio Extension and warm anomalies within that current in 2025 are associated with a long-lasting northward shift of that current (see section 3g). Pacific marginal seas remained warmer than climatological means in 2025, as they were in 2024.

In the Indian Ocean, the 2025-minus-2024 difference of OHCA (Fig. 3.5b) shows a strong decrease from about 15°S to about 5°S in the western two-thirds of the basin, with a smaller magnitude increase almost everywhere else. The 2025 OHCA anomalies (Fig. 3.5a) were mostly positive, except around some of the outer edges of the aforementioned strong decrease.

The 2025-minus-2024 difference of OHCA (Fig. 3.5b) in the Atlantic Ocean was heterogeneous, with broad regions of relatively weak cooling and warming in the interior, and smaller scale but stronger eddy signatures of warming and cooling in western boundary current extensions and the Antarctic Circumpolar Current (ACC). Much of the Atlantic Ocean exhibited OHCA well above the 1993–2022 average (Fig. 3.5a), with anomalies in the Gulf of America/Gulf of Mexico being especially high. The north side of the Gulf Stream extension remained cool as it was in 2024, suggesting a continued southward shift in the axis of that current. The cooler-than-average conditions southeast of Greenland that have persisted for several years were less apparent in 2025.

As expected, the large-scale statistically significant regional patterns in the 1993–2025 local linear trends of 0-m–2000-m OHCA (Fig. 3.5c) are similar to those from 1993–2024 (Johnson et al. 2025), and earlier reports for 0-m–700-m OHCA.

Near-global average seasonal temperature anomalies in the upper 2000 dbar of the ocean since 1993 (Fig. 3.6) show signatures of past strong El Niño events: Subsurface cold anomalies with maximum amplitude around 140 dbar–150 dbar and warm near-surface anomalies with maximum amplitude around 40 dbar–50 dbar peak in boreal winters of El Niño years. The opposite pattern is observed during La Niña years (Fig. 3.6a). Boreal winter 2023/24 shows a typical El Niño signature, with a near-surface warm anomaly and a relatively cool (compared to surrounding years) subsurface anomaly centered at about 160 dbar. The record-warm near-surface anomalies reached during winter 2023/24 have slowly diminished over the past two years, with two subsequent winters that have exhibited weak La Niña conditions. However, the ocean below 100 dbar has exhibited an overall warming trend over this period. The 33-year record length warming trend (Fig. 3.6b) is strongest near the surface (0.19°C decade^{-1} at 30 dbar), diminishing steadily with increasing pressure to reach 0.04°C decade^{-1} by 420 dbar, and then diminishing more gradually with increasing pressure to about 0.01°C decade^{-1} around 2000 dbar.

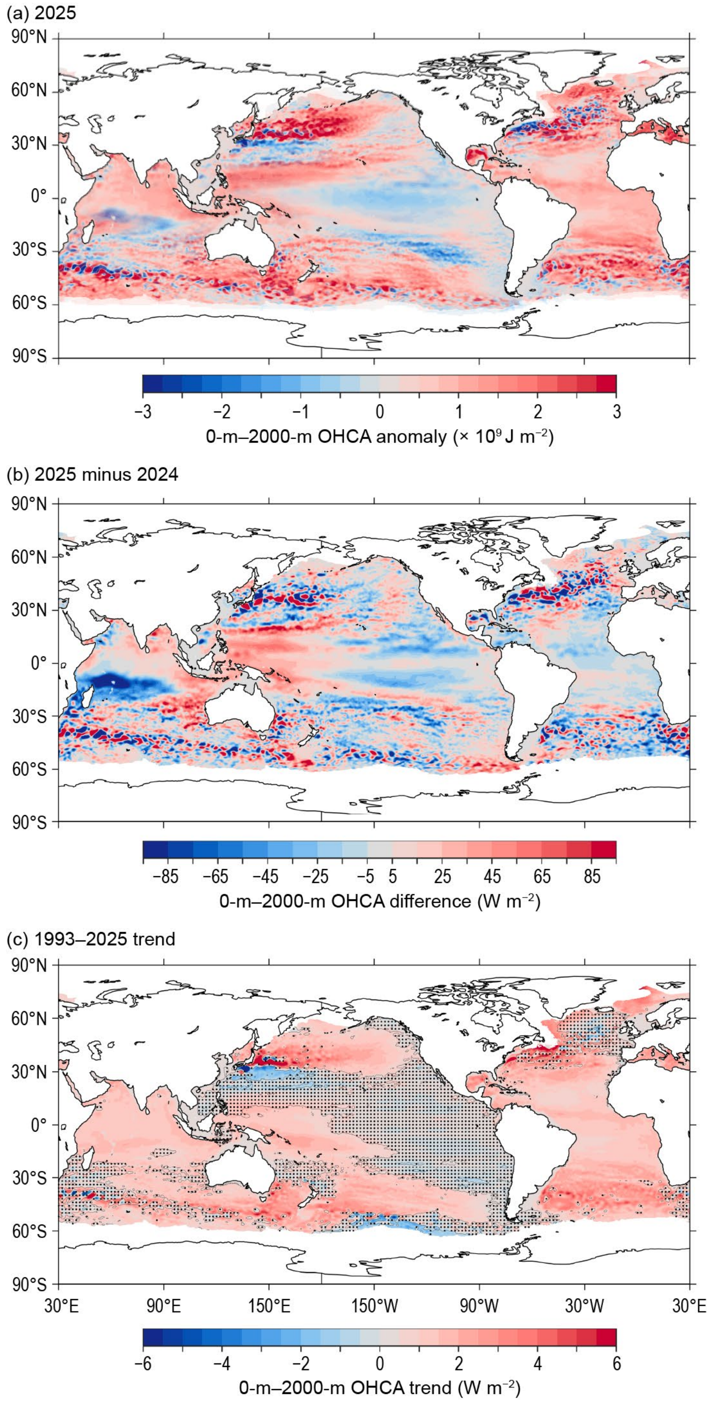

Fig. 3.5. (a) Random Forest Regression Ocean Maps (RFROM) v2 estimate of 0-m–2000-m ocean heat content anomaly (OHCA; × 10^9 J m^{-2}) for 2025 analyzed following Lyman and Johnson (2023) with v2.2 improvements as in https://www.pmel.noaa.gov/rfrom/. Values are displayed relative to a 1993–2022 baseline. (b) 2025-minus-2024 of 0-m–2000-m OHCA expressed as a local surface heat flux equivalent (W m^{-2}). For (a) and (b) comparisons, note that 95 W m^{-2} applied over one-year results in a 3 × 10^9 J m^{-2} change of OHCA. (c) Linear trend for 1993–2025 0-m–2000-m annual OHCA (W m^{-2}). Areas with statistically insignificant trends at 5%–95% confidence (taking into account the decorrelation time scale of the residuals when estimating effective degrees of freedom) are stippled.

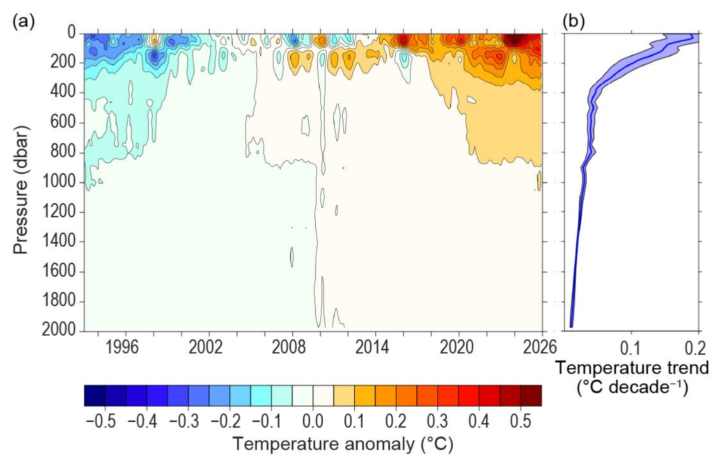

Fig. 3.6. (a) Near-global (66.5°S–81.5°N, but excluding seasonally ice-covered regions within that latitude range) average monthly ocean temperature anomalies (°C; from Random Forest Regression Ocean Maps [RFROM] v2.2, Lyman and Johnson [2023]) relative to a 1993–2022 seasonal cycle and mean, smoothed with a five-month Hanning filter and contoured at 0.05°C intervals (see color bar) vs. pressure and time. (b) Linear trend of temperature anomalies over the period 1993–2025 in (a) plotted vs. pressure in °C decade^{-1} (blue line) with 5%–95% confidence intervals (blue shading).

Nearly global integrated annually averaged OHCA estimates from 0 m–700 m and 700 m–2000 m from six and five research groups, respectively, are presented (Fig. 3.7). As noted in previous reports, year-round, near-global sampling in both of those layers commenced around 2005 from Argo, making estimates relatively certain after that date. Deep expendable bathythermographs sampling to 700 m were deployed extensively over much of the globe (with the exception of the high southern latitudes) starting in the early 1990s (Lyman and Johnson 2014), hence the upper layer results may be fairly robust back to 1993. Results for the 700-m–2000-m layer, which is quite sparsely sampled prior to about 2005, should be interpreted with caution in earlier years.

The various estimates of annual globally integrated 0-m–700-m OHCA (Fig. 3.7a) consistently show large increases since 1993, with all six analyses reporting 2025 as a record high. The 700-m–2000-m OHCA annual analyses (Fig. 3.7b) show a smaller, but still distinct, long-term warming trend, and again all five analyses report 2025 as a record high in that deeper layer. The water column from 0 m to 700 m gained 13±5 ZJ and from 700 m to 2000 m gained 8.0±1.1 ZJ (means and standard deviations given) from 2024 to 2025. Causes of differences among estimates are discussed in Johnson et al. (2014, 2015).

The estimated linear rates of heat gain for each of the six global integral estimates of 0-m–700-m OHCA that extended from 1993 through 2025 (Fig. 3.7a) range from 0.39 (±0.05) W m^{-2} to 0.48 (±0.07) W m^{-2}. These estimates are applied over the surface area of Earth (Table 3.2) rather than the surface area of the ocean, to relate directly to the top-of-atmosphere energy imbalance (e.g., Loeb et al. 2021; see section 2f for details). Linear trends for the 700-m–2000-m layer from five groups over the same time period range from 0.18 (±0.03) W m^{-2} to 0.24 (±0.03) W m^{-2}. Trends from all groups agree within 5%–95% uncertainties in both layers. Using shipboard and Deep Argo CTD data collected from 1968 through 2025 to update the OHCA estimates of Johnson and Purkey (2024) for the 2000-dbar–6000-dbar layer, the linear trend is 0.07 (±0.02) W m^{-2} from February 1988 to June 2015. These dates are the global volume-average times of the first and last sampling used in the local trend calculations.

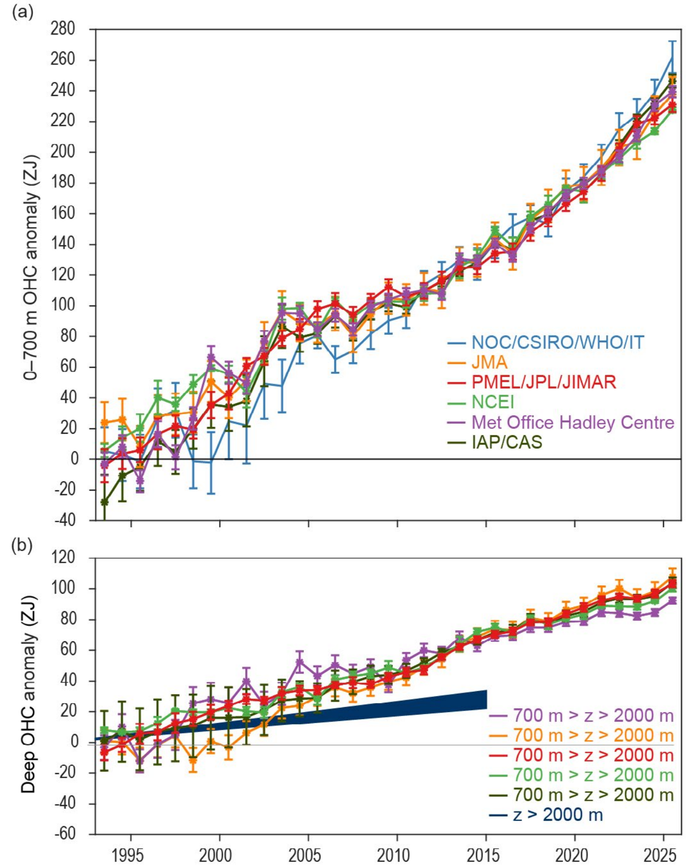

Fig. 3.7. (a) Annually averaged global integrals of in situ estimates of upper (0 m–700 m) ocean heat content anomaly (OHCA; ZJ; 1 ZJ = 10^{21} J) for the period 1993–2025 with standard errors of the mean. The Meteorological Research Institute (MRI)/Japan Meteorological Agency (JMA estimate is an update of Ishii et al. (2017). The Pacific Marine Environmental Laboratory (PMEL)/Jet Propulsion Laboratory (JPL)/Cooperative Institute for Marine and Atmospheric Research (CIMAR) estimate is from Random Forest Regression Ocean Maps (RFROM) v2.2 after Lyman and Johnson (2023). The Met Office Hadley Centre estimate is computed from gridded monthly temperature anomalies following Palmer et al. (2007) and Good et al. (2013). Both the PMEL and Met Office estimates use Cheng et al. (2014) eXpendable BathyThermograph (XBT) corrections and Gouretski and Cheng (2020) mechanical bathythermograph corrections (MBT) corrections. The NCEI estimate follows Levitus et al. (2012). The Institute of Atmospheric Physics (IAP)/Chinese Academy of Sciences (CAS) estimate was reported in Pan et al. (2026). The National Oceanography Centre (NOC)/Commonwealth Scientific and Industrial Research Organisation (CSIRO)/Woods Hole Oceanographic Institution (WHOI)/Indian Institutes of Technology (IIT) estimate is an update of Domingues et al. (2008). See Johnson et al. (2015, 2024) for details on uncertainties, methods, and datasets. For comparison, all estimates have been individually offset (vertically on the plot), first to their individual 2005–25 means (the best sampled time period) and then to their collective 1993 mean. (b) Annual average global integrals of in situ estimates of intermediate (700 m–2000 m) OHCA for 1993–2025 (ZJ) with standard errors of the mean and a long-term trend with one standard error uncertainty shown from February 1988 to June 2015 for deep and abyssal (2000 dbar–6000 dbar) OHCA following Johnson and Purkey (2024) but updated as detailed in the text.

This result is consistent with previously reported decadal deep and abyssal warming trends (e.g., Purkey and Johnson 2010), though it features smaller uncertainties than earlier estimates due to inclusion of more recent and historical data. Summing the three layers (despite their different time periods as given above), the full-depth ocean heat gain rate applied to Earth's entire surface ranges from 0.65 W m^{-2} to 0.74 W m^{-2}. While in situ observations of long-term rates of heat uptake by the ocean and other components of Earth's climate system are used to calibrate top-of-atmosphere satellite measurements of Earth's energy imbalance (e.g., Loeb et al. 2024), the precision and stability of those satellite measurements allows closer tracking of year-to-year variations in that quantity (see section 2f).

Table 3.2. Trends of ocean heat content increase (in W m^{-2} applied over the 5.1×10^{14} m^2 surface area of Earth) from seven different research groups over three depth ranges (see Fig. 3.7 for details). For the upper (0-m–700-m) and intermediate (700-m–2000-m) depth ranges, estimates cover 1993–2025, with 5%–95% uncertainties based on the residuals taking their temporal correlation into account when estimating degrees of freedom (Von Storch and Zwiers 1999). The 2000-dbar–6000-dbar depth range estimate, an update of Johnson and Purkey (2024), uses data from 1970 to 2025, having a global average start and end date of February 1988 to June 2015, again with 5%–95% uncertainty.

Research group	0 m–700 m Global ocean heat content trends (W m^{-2})	700 m–2000 m Global ocean heat content trends (W m^{-2})	2000 dbar–6000 dbar Global ocean heat content trends (W m^{-2})
MRI/JMA	0.40±0.06	0.24±0.03	—
PMEL/JPL/CIMAR	0.42±0.08	0.20±0.03	—
NCEI	0.39±0.05	0.19±0.02	—
Met Office Hadley Centre	0.43±0.08	0.18±0.03	—
IAP/CAS	0.47±0.07	0.21±0.02	—
NOC/CSIRO/WHOI/IIT	0.48±0.07	—	—
Johnson and Purkey	—	—	0.07±0.02

d. Salinity

—J. Reagan, J. M. Lyman, and R. Locarnini

1. INTRODUCTION

Ocean salinity is the concentration of dissolved salts in seawater. Surface freshwater fluxes such as precipitation and evaporation, river run-off, ice melt, and ice freezing can alter local salinity, with advection and mixing redistributing these anomalies at both the surface and subsurface (Ren et al. 2011; Yu 2011). Salinity is a conservative tracer and as it is subducted into the subsurface, it retains its surface footprint (in the absence of mixing), allowing water masses to be tracked over large distances. Ocean salinity also plays a major role in ocean stratification and ultimately deep-ocean circulation by stabilizing (destabilizing) the water column leading to reduced (enhanced) mixing. Additionally, changes in ocean salinity can act as a proxy for estimating the strength of the global hydrological cycle (Schmitt 1995; Durack et al. 2012; Skliris et al. 2014), while the integration of salinity anomalies provides estimates of freshwater content. Finally, ocean salinity anomalies have been shown to improve subseasonal to seasonal precipitation forecasts (Li et al. 2016; Arcodia et al. 2025).

The sea surface salinity (SSS) analysis relies on Argo data downloaded in January 2026, with annual anomaly maps relative to a seasonal climatology generated following Johnson and Lyman (2012) updated using World Ocean Atlas 2023 (Reagan et al. 2024) as well as monthly maps of bulk (as opposed to skin) SSS data from the Blended Analysis of Surface Salinity (BASS; Xie et al. 2014). BASS blends in situ SSS data with data from the Aquarius (Le Vine et al. 2014; mission ended in June 2015), Soil Moisture and Ocean Salinity (SMOS; Font et al. 2013), and the Soil Moisture Active Passive (SMAP; Fore et al. 2016) satellite missions. Despite the larger uncertainties of satellite data relative to Argo data, their higher spatial and temporal sampling allows higher spatial and temporal resolution maps than are possible using in situ data alone at present. To investigate interannual changes of subsurface salinity, all available salinity profile data within the World Ocean Database (Mishonov et al. 2024; WOD Team 2025) are quality controlled following Garcia et al. (2024b) and then used to derive 1° monthly mean gridded salinity anomalies relative to a long-term monthly mean for the years 1955–2022 from World Ocean Atlas 2023 at standard depths from the surface to 2000 m. Note that all salinity values used in this section are reported on the dimensionless Practical Salinity Scale-78 (PSS-78; Fofonoff and Lewis 1979).

Since ~2005, profiling floats of the Argo program (Riser et al. 2016) have dominated the ocean salinity observing system and have provided unprecedented spatial and temporal coverage of salinity. These data are a mix of real-time (preliminary) and delayed-mode (scientific quality controlled) observations. Hence, the estimates presented here may be subject to instrument biases such as the positive salinity drift identified in a subset of Argo floats (Wong et al. 2023), and will be refined after all data are subjected to scientific quality control.

2. SEA SURFACE SALINITY

Sea surface salinity anomalies, unlike SST anomalies, are generally quite persistent since salinity has no direct feedback to the atmosphere. Regions dominated by evaporation, such as the subtropics, tend to exhibit higher salinity values, while areas where precipitation prevails, like the Intertropical Convergence Zone (ITCZ) and high latitudes, usually have fresher water (e.g., Wüst 1936; Schmitt 1995).

The equatorial Pacific generally became saltier from 2024 to 2025 (Fig. 3.8b). This includes both the western equatorial Pacific fresh pool and the ITCZ. However, the South Pacific Convergence Zone (SPCZ) freshened and shifted south after moving north in 2024 (see section 3e). Also, a strong patch of anomalously fresh water just east of the Galápagos Islands became even fresher. The Philippine Sea, which had become saltier in 2024, became anomalously fresh (Fig. 3.8a).

The North Atlantic experienced regions of SSS freshening in the Davis Strait, the Greenland Sea, and the Labrador Sea (Fig. 3.8b). This sea surface freshening at high latitudes is potentially important in that it could affect thermohaline circulation by making surface waters less dense (Gordon 1986; Broecker 1991). A fresh region off Venezuela also developed in 2025, presumably from an increase in river runoff from the Orinoco and possibly the Amazon Rivers (see section 2d). The ITCZ in the Atlantic remained anomalously fresh in 2025 (Fig. 3.8a).

The equatorial Indian Ocean, which had become relatively fresh in 2024, became saltier in 2025, shifting from anomalously fresh to slightly salty (Figs. 3.8a,b). While the region west of Australia became anomalously fresh, reversing the pattern of SSS change that was observed last year. As would be expected in the weak La Niña conditions, a freshening occurred over the maritime continent as precipitation increased over this region (see section 3e).

Sea surface salinity trends from 2005 to 2025 are essentially unchanged compared to those previously reported in Johnson and Lyman (2025). While most regions have statistically insignificant trends, there has been, and continues to be, statistically significant freshening in some climatologically fresh areas such as parts of the Pacific ITCZ, the Gulf of Alaska, the northeastern portions of the North Atlantic Ocean, the Greenland-Iceland-Norwegian Seas, the western Bay of Bengal, and the Gulf of Guinea (Fig. 3.8c). Likewise, climatologically salty regions have become increasingly salty, as evidenced by portions of the subtropics across all ocean basins. This overall "salty gets saltier and fresh gets fresher" trend, which has been evident to varying degrees and discussed in *State of the Climate* reports since 2006, is expected on a warming Earth. As the atmosphere warms, it can hold more moisture, enabling an increased hydrological cycle over the ocean (Held and Soden 2006; Durack and Wijffels 2010; Durack et al. 2012, Skliris et al. 2014).

The seasonal progression in the surface salinity features shown in Argo data can be traced in BASS SSS anomalies, which have higher spatial and temporal resolution but less accuracy (Fig. 3.9). In the equatorial Pacific, the freshening east of the Galápagos Islands is relatively episodic, occurring primarily during the March–May season, when precipitation is generally high. The Amazon/Orinoco River plume region is salty during December–February when river runoff is low, and becomes fresher in the subsequent seasons as flow increases. In the Indian Ocean, the region of anomalous freshwater west of Australia starts off fresh in December–February, and becomes progressively fresher each season, reaching its freshest in September–November.

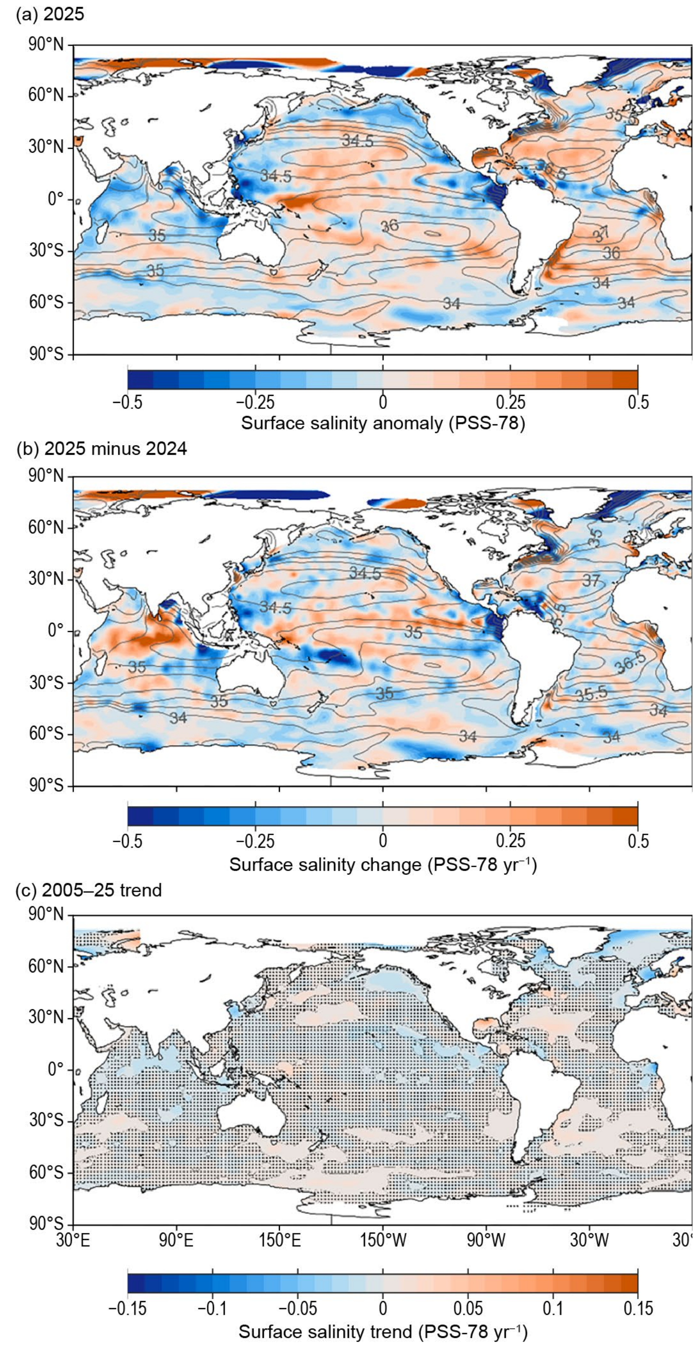

Fig. 3.8. (a) Map of the 2025 annual surface salinity anomaly (colors, Practical Salinity Scale-78 [PSS-78]) with respect to monthly climatological 1955–2022 salinity fields from World Ocean Atlas 2023 (yearly average; gray contours at 0.5 intervals, PSS-78). (b) Difference of 2025 and 2024 surface salinity maps (colors, PSS-78 yr^{-1}). White ocean areas are too data-poor (retaining <80% of a large-scale signal) to map. (c) Map of local linear trends estimated from annual surface salinity anomalies for 2005–25 (colors, PSS-78 yr^{-1}). Areas with statistically insignificant trends at 5%–95% confidence (taking into account the decorrelation time scale of the residuals when estimating effective degrees of freedom) are stippled. All maps are made using Argo data.

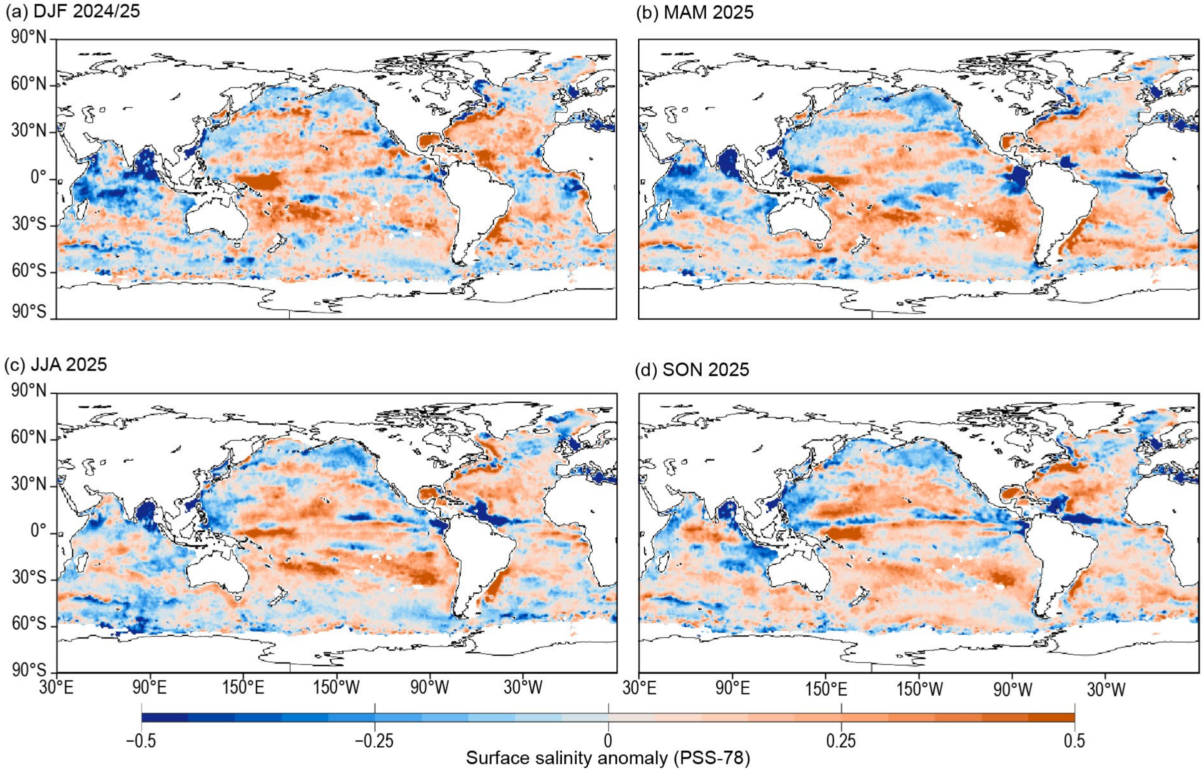

Fig. 3.9. Seasonal maps of surface salinity anomalies (colors) from monthly blended maps of satellite and in situ salinity data (Blended Analysis of Surface Salinity [BASS]; Xie et al. 2014) relative to monthly climatological 1955–2022 salinity fields from World Ocean Atlas 2023 for (a) Dec 2024–Feb 2025, (b) Mar–May 2025, (c) Jun–Aug 2025, and (d) Sep–Nov 2025.

3. SUBSURFACE SALINITY

Subduction (downward movement along isopycnals) and convection (vertical mixing) are the two primary pathways for surface water to reach the ocean interior. The propagation of surface salinity anomalies into the ocean's interior enables water masses to be tracked, changes in freshwater content to be estimated, and potential impacts on ocean dynamics to be assessed.

The 2025 Atlantic basin-averaged salinity anomalies continued the multiyear pattern that has been evident since ~2020, with nearly the entire 0-m–1000-m layer saltier than the long-term mean, and the greatest anomalies (>0.06) observed in the upper 100 m, decreasing with depth (Fig. 3.10a). Unlike the strong (>0.02) near-surface increase in the Atlantic basin-averaged salinity from 2023 to 2024 (Reagan et al. 2025), the 2024 to 2025 changes are within ±0.01 in the upper 1000 m (Fig. 3.10b). The weak salinity changes in the Atlantic between 2024 and 2025 are reflected in the interannual change in zonally averaged salinity, where significant changes are mostly localized and shallow (Fig. 3.10c).

The basin-averaged Pacific salinity anomalies, unlike the Atlantic, have exhibited vertical decoupling over the past decade with recent near-surface salinification deepening in 2025 (Fig. 3.10d). The deepening of the near-surface salinification is more evident in the basin-averaged salinity difference between 2024 and 2025 where there is slight (~−0.008) freshening in the upper 30 m and salinification extending from ~30 m to 600 m with a peak (~0.012) at 100 m (Fig. 3.10e). The slight freshening at the surface is influenced by shallow freshening between 10°S and 20°S (Figs. 3.10e,f.), which may be due to enhanced precipitation in the SPCZ (Section 3e). The maximum salinification at 100 m is a reflection of the positive changes in both the northern and southern Pacific subduction zones (20°S–30°S and 20°N–30°N) and large changes (>0.03) near 50°N.

Similar to the Pacific, the Indian Ocean basin-averaged salinity anomalies have exhibited vertical decoupling since mid-2019 with fresh anomalies (<−0.01) in the upper 100 m and weak (≤0.01) salty anomalies in a 100-m–200-m thick layer beneath (Fig. 3.10g). From 2024 to 2025, the fresh anomalies near the surface deepened with the −0.02 contour moving from 50 m to 100 m.

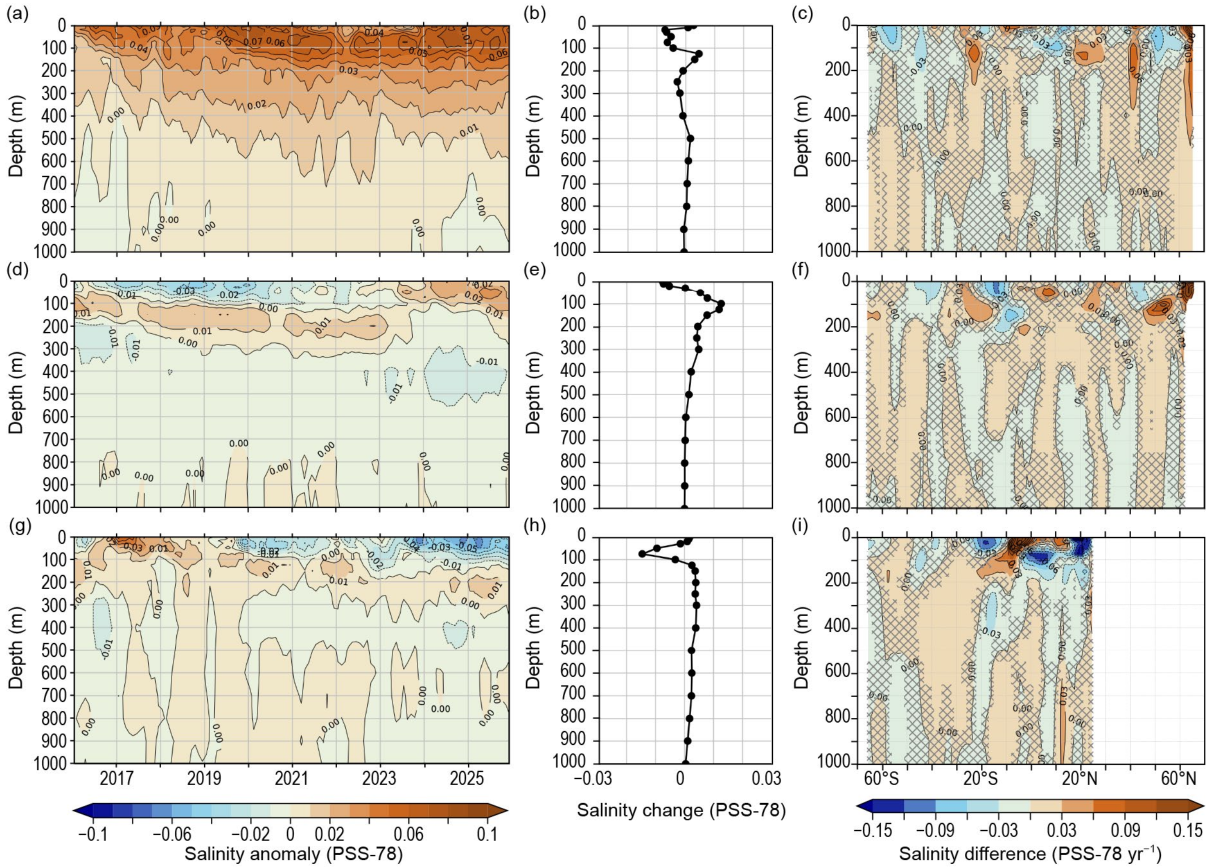

Fig. 3.10. Average monthly salinity anomalies (Practical Salinity Scale-78 [PSS-78]) vs. depth for the (a) Atlantic, (d) Pacific, and (g) Indian basins from 2016 through 2025. Change in salinity from 2024 to 2025 vs. depth for the (b) Atlantic, (e) Pacific, and (h) Indian basins. Change in the 0-m–1000-m zonal-average salinity from 2024 to 2025 vs. latitude and depth in the (c) Atlantic, (f) Pacific, and (i) Indian Ocean. Areas of statistically insignificant change, defined as <±1 std. dev. and calculated from all year-to-year changes between 2005 and 2024, are stippled in gray. Data are smoothed using a three-month running mean. Anomalies are relative to the long-term (1955–2022) World Ocean Atlas 2023 monthly salinity climatology (Reagan et al. 2024).

This freshening is even more evident in the basin-averaged change where there was peak freshening at 75 m (~−0.015), with very weak salinification below (<0.005) (Fig. 3.10h). The most significant changes between 2024 and 2025 occurred within the tropics and in the upper 200 m, which is consistent with freshwater fluxes playing a large role in this interannual change (Fig. 3.10i).

Surface salinity anomalies reflect changes in freshwater fluxes and are redistributed both horizontally and vertically through ocean circulation. The 2005–25 zonally averaged salinity trends highlight common large-scale changes, but also reveal basin-specific contrasts (Fig. 3.11). As documented in prior *State of the Climate* reports (e.g., Reagan et al. 2025), the large-scale trends, particularly near the surface (Fig. 3.8c), reflect the "wet gets wetter, dry gets drier" paradigm (Held and Soden 2006) that has been recognized in multiple studies (e.g., Durack and Wijffels 2010; Durack et al. 2012; Skliris et al. 2014).

The 2005–25 Atlantic zonally averaged salinity trends (Fig. 3.11a) remain largely unchanged from prior *State of the Climate* reports, as there were few significant changes between 2024 and 2025 (Fig. 3.10c). Unlike the Atlantic, the 2005–25 Pacific salinity trends do not exhibit coherent significant trends from the upper ocean to deeper depths outside of the 55°S–65°S salinification band that extends from the surface to >900 m (Fig. 3.11b). While there were some significant changes in the upper 200 m in the Pacific between 2024 and 2025 (Figs. 3.10e,f), these changes do not substantially alter the significant 2005–25 trends. The 2005–25 zonally averaged Indian Ocean basin trends are dominated by significant subsurface changes, with much of the surface characterized by insignificant trends outside of freshening in the upper 50 m between the equator and 15°N. The salinification changes in 2025 (Fig. 3.10i) may have modestly strengthened the subsurface salinification region in the South Indian Ocean basin between 125 m and 550 m and 35°S–50°S (Fig. 3.11c) when compared to the 2005–24 trends (see Fig. 3.11c in Reagan et al. 2025). Overall, the 2025 basin-scale changes in subsurface salinity did not significantly impact the long-term trends.

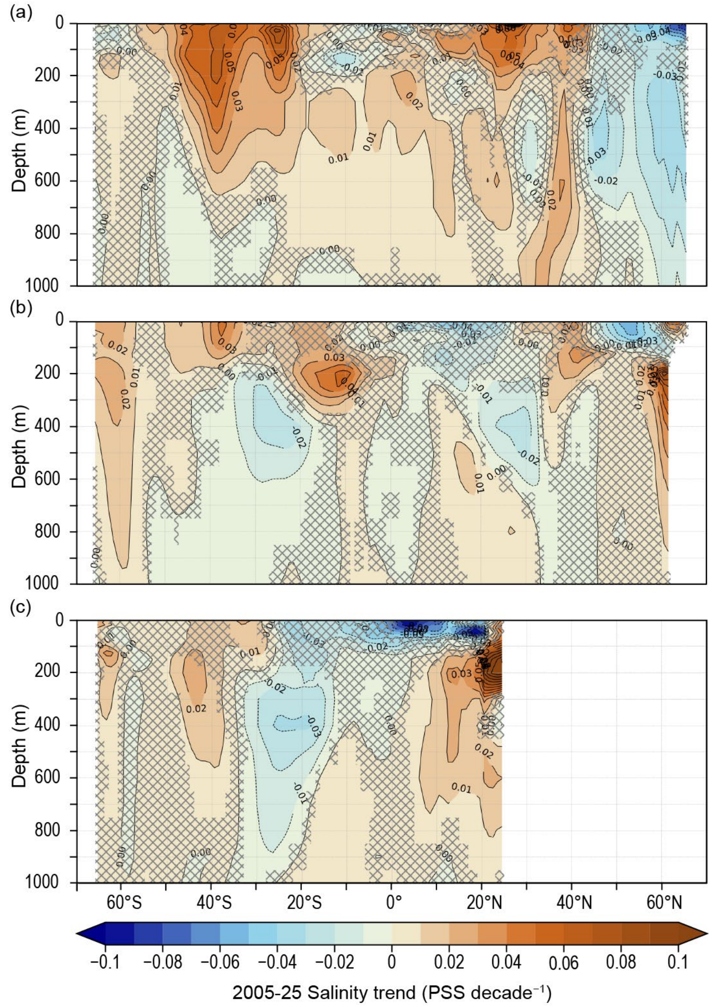

Fig. 3.11. Linear trends of zonally averaged salinity (Practical Salinity Scale-78 [PSS-78], psu decade^{-1}) for the period 2005–25 vs. latitude and depth for the (a) Atlantic, (b) Pacific, and (c) Indian Ocean computed using least squares regression. Areas stippled in gray are not significant at the 95% confidence interval.

e. Global ocean heat, freshwater, and momentum fluxes

—L. Yu, P. W. Stackhouse, and R. A. Weller

The ocean and the atmosphere interact through the exchange of heat, freshwater, and momentum across their interface. These air–sea fluxes are key to maintaining the global climate system's equilibrium in response to incoming solar radiation. The ocean absorbs the majority of shortwave radiation reaching the Earth's surface and returns energy to the atmosphere through longwave radiation, evaporation (latent heat flux), and conduction (sensible heat flux). Any remaining heat is stored in the ocean and redistributed by currents, driven largely by wind stress. Evaporation not only mediates heat but also moisture transfer, the latter of which, together with precipitation, determines the surface freshwater flux across the open ocean. Variations in these air–sea fluxes are key drivers of changes in ocean circulation, influencing the global distribution of heat and salt from the tropics to the poles.

Here, we present surface heat flux, freshwater flux, and wind stress for 2025, along with their changes relative to 2024. The net surface heat flux (Q_{net}) comprises four components: shortwave (SW), longwave (LW), latent heat (LH), and sensible heat (SH). We calculate the net surface freshwater flux into the ocean, excluding inputs from rivers and glaciers, as the difference between precipitation (*P*) and evaporation (*E*), referred to as the *P*–*E* flux. Data from multiple research groups are synthesized to produce global maps of Q_{net}, *P*–*E*, and wind stress (Figs. 3.12–3.14) and provide a long-term view over time (Fig. 3.15). SW and LW in 2024 were sourced from the Fast Longwave And Shortwave Radiative Fluxes (FLASHFlux) version 4A product (Stackhouse et al. 2006), which have been radiometrically scaled to the SW and LW products from the Clouds and the Earth's Radiant Energy Systems (CERES) Surface Energy Balanced and Filled (EBAF) Edition 4.2 (Loeb et al. 2018; Kato et al. 2018). SW and LW in 2024 and 2025 were also sourced from the ERA5 reanalysis (Hersbach et al. 2020), which provides comparable surface radiation fields. *P* was derived from the Global Precipitation Climatology Project (GPCP) version 2.3 products (Adler et al. 2018). Estimates for LH, SH, *E*, and wind stress were produced by the second generation of the Objectively Analyzed Air–Sea Heat Fluxes (OAFlux2; Yu and Weller 2007; Yu 2019), computed from satellite retrievals and the bulk parameterization COARE version 3.6 (Fairall et al. 2003). The Q_{net} time series begins in 2001, aligning with the availability of CERES EBAF 4.2.1 products, while the *P*–*E* and wind stress time series extend back 38 years, starting in 1988.

1. SURFACE HEAT FLUXES

The 2025 Q_{net} anomalies relative to 2001–15 (Fig. 3.12a) are predominantly positive, indicating enhanced ocean heat gain over much of the global ocean. The largest positive anomalies (~10 W m^{-2}–20 W m^{-2}) occur in the tropical Indian Ocean, tropical Atlantic, and across much of the tropical and subtropical Pacific. Negative anomalies, indicating enhanced ocean heat loss, are concentrated in the central North Pacific (30°N–50°N), parts of the subtropical North Atlantic, the South Indian Ocean, and portions of the Southern Ocean. The central North Pacific heat-loss feature is consistent with the Pacific Decadal Oscillation (PDO)-like pattern evident in recent years, although it is weaker than in 2024. The 2025 Q_{net} anomalies are consistent with corresponding sea surface temperature anomalies (see Fig. 3.2a).

The 2025–2024 Q_{net} differences (Fig. 3.12b) are positive across broad regions, implying greater ocean heat gain in 2025 than in 2024. The largest increases (~10 W m^{-2}–20 W m^{-2}) occur in the North Atlantic (20°N–40°N and the subpolar gyre poleward of 55°N), the midlatitude North Pacific, and the subtropical South Pacific and South Atlantic. Notably, the Kuroshio Extension region exhibits positive differences of ~10 W m^{-2}–15 W m^{-2}, reversing the pronounced negative Q_{net} anomalies (~20 W m^{-2}) observed in 2024. The North Atlantic (20°N–40°N) also shows widespread positive differences of ~15 W m^{-2}–20 W m^{-2}. In contrast, the South Indian Ocean displays a more heterogeneous pattern, with alternating bands of positive and negative Q_{net} differences.

These year-to-year Q_{net} changes are driven primarily by differences in turbulent heat fluxes (LH+SH; Fig. 3.12d), with a smaller contribution from net surface radiation (SW–LW; Fig. 3.12c). Radiative differences are generally weak over most basins, with modest positive anomalies (~5 W m^{-2}) in many midlatitude regions. The clearest radiative feature is a dipole over the far western Pacific/Maritime Continent, with negative anomalies to the west and positive anomalies to the east, consistent with a shift in convection under weak La Niña conditions.

For Fig. 3.12d, red (negative) LH+SH differences indicate reduced turbulent heat loss from the ocean (therefore greater ocean heat gain in 2025), whereas blue (positive) differences indicate enhanced turbulent heat loss. The LH+SH differences show widespread negative (red) anomalies (~10 W m^{-2}–20 W m^{-2}) over the North Atlantic (20°N–40°N and the subpolar gyre), the midlatitude North Pacific, and the subtropical South Pacific and South Atlantic, consistent with reduced turbulent cooling in 2025. Positive (blue) differences (locally ~15 W m^{-2}–25 W m^{-2}) indicate enhanced turbulent heat loss over parts of the tropical Indian Ocean (15°S–30°S), with weaker positive anomalies in portions of the subtropical North Atlantic and North Pacific (10°S–25°N).

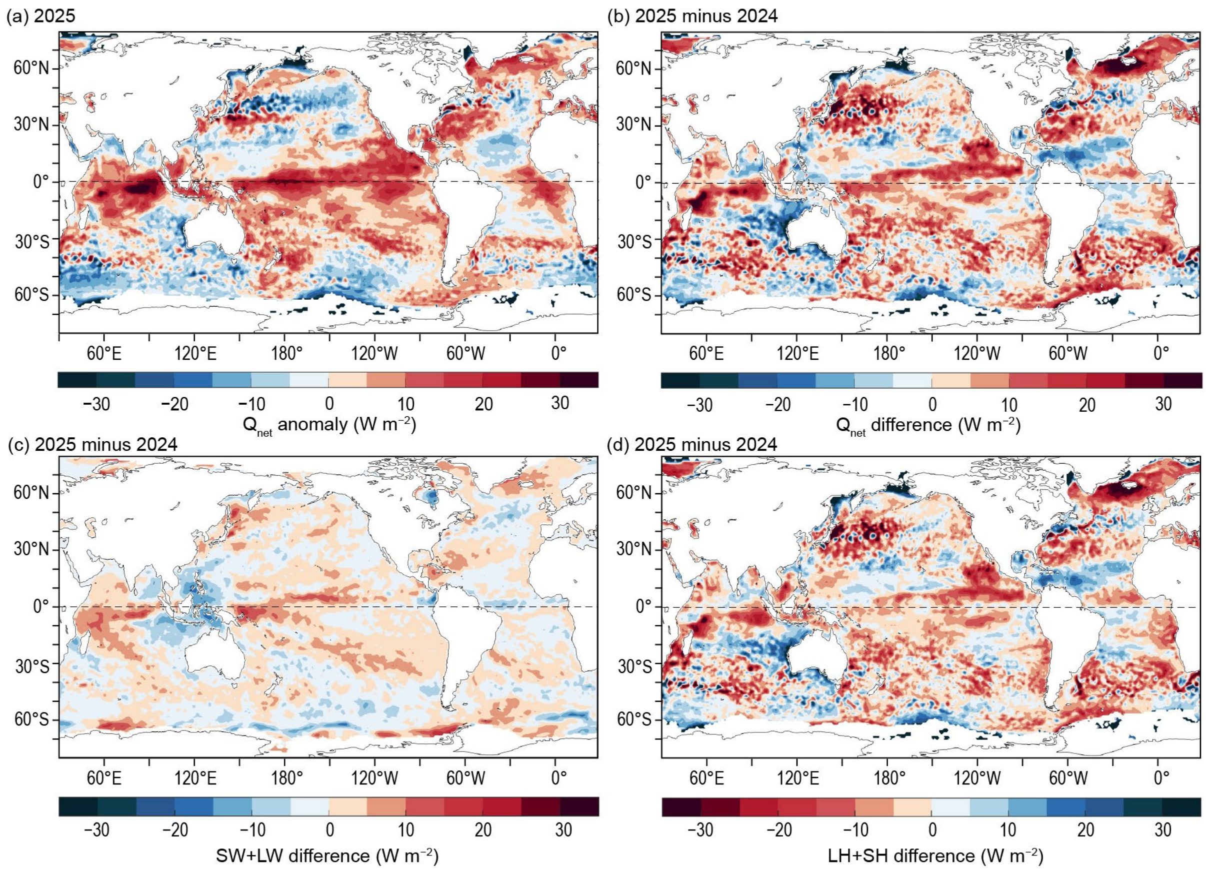

Fig. 3.12. (a) Surface heat flux (Q_{net}) anomalies (W m^{-2}) for 2025 relative to the 2001–15 climatology. Positive (negative) values denote ocean heat gain (loss). (b) 2025-minus-2024 difference for (b) Q_{net}, (c) net surface radiation (shortwave [SW] – longwave [LW]), and (d) turbulent heat fluxes (latent heat [LH] + sensible heat [SH]), respectively. Positive tendencies denote more ocean heat gain in 2025 than in 2024. LH+SH are from Woods Hole Oceanographic Institution (WHOI) OAFlux2, and SW–LW from ERA5. Net radiative fluxes defined as the difference between the incoming and outgoing radiation (positive indicates radiative flux into the ocean).

2. SURFACE FRESHWATER FLUXES

The 2025 *P–E* anomalies relative to the 2001–15 climatological mean (Fig. 3.13a) show widespread positive *P–E* (green colors), indicating anomalous net freshwater gain and a freshening tendency over much of the tropical ocean. The strongest freshening anomalies occur over the western tropical Pacific/Maritime Continent, with weaker positive anomalies (~10 cm yr^{-1}) in parts of the tropical Indian and tropical Atlantic Oceans. In contrast, negative *P–E* anomalies (brown colors) across the central equatorial Pacific indicate anomalous net freshwater loss and a salinification tendency (see Fig. 3.8a), locally exceeding ~60 cm yr^{-1}. Additional salinification anomalies appear in patches of the midlatitude North Pacific and in parts of the Southern Ocean (south of 40°S). Freshwater loss anomalies remained notable in the central North Pacific (~20 cm yr^{-1}), consistent with the continued negative PDO-like background state.

The 2025–2024 *P–E* differences (Fig. 3.13b) are dominated by tropical Pacific changes consistent with the shift from ENSO-neutral conditions in 2024 to weak La Niña in 2025. Relative to

2024, P–E decreased sharply across the central/eastern equatorial Pacific, indicating enhanced freshwater loss and a stronger salinification tendency (locally >60 cm yr^{-1}), while P–E increased over the far western Pacific/Maritime Continent and parts of the southwest Pacific/South Pacific Convergence Zone (SPCZ), indicating enhanced freshwater gain and a stronger freshening tendency in 2025. In contrast, the western tropical Indian Ocean and portions of the subtropical North and South Atlantic Ocean show reduced P–E in 2025, implying a shift toward greater freshwater loss (salinification) relative to 2024. These year-to-year P–E changes are driven primarily by precipitation (Fig. 3.13d), with rainfall decreasing over the central/eastern equatorial Pacific and increasing over the far western Pacific/Maritime Continent and parts of the SPCZ. Evaporation differences (Fig. 3.13c) are comparatively weak, including a modest decrease over the eastern equatorial Pacific cold tongue consistent with cooler SSTs during weak La Niña conditions, confirming that precipitation dominates the 2025–2024 P–E changes.

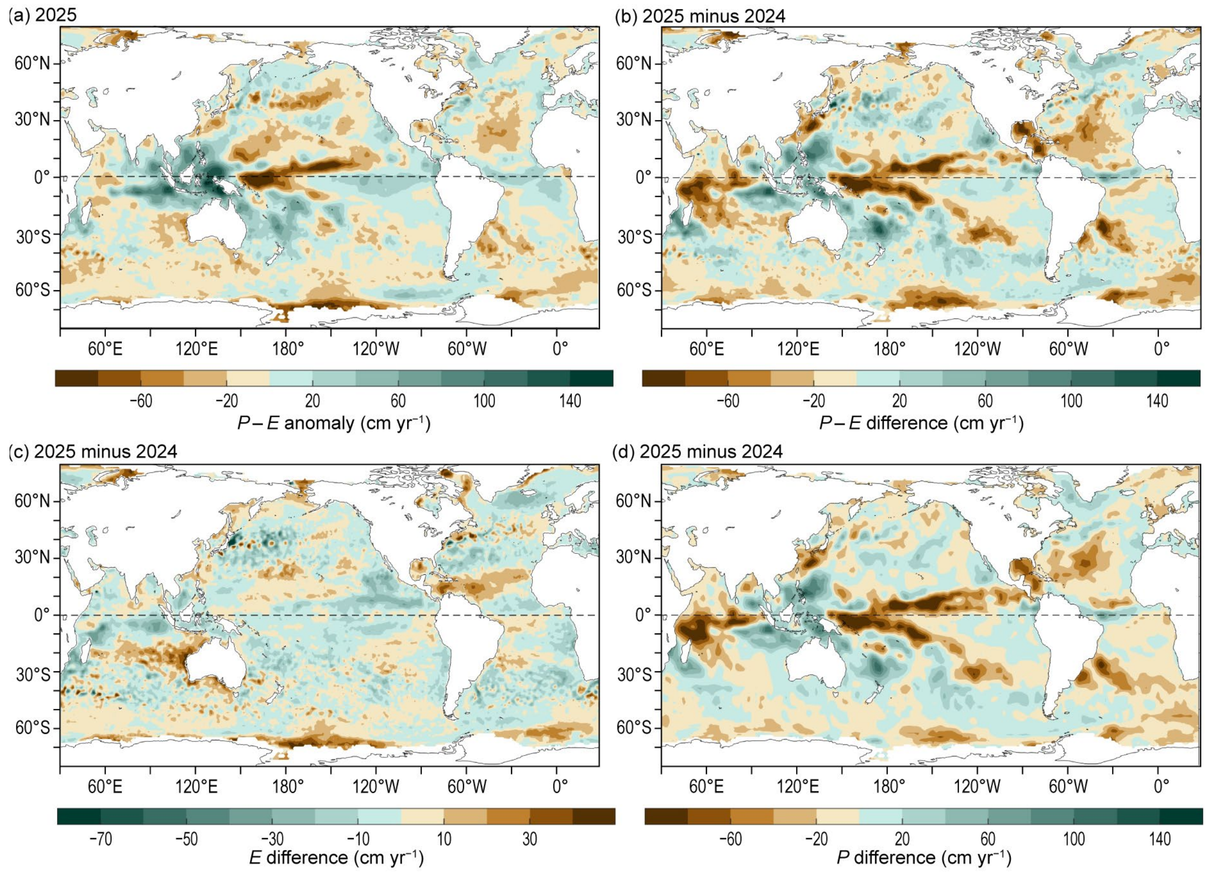

Fig. 3.13. (a) Surface freshwater precipitation (*P*)–evaporation (*E*) flux anomalies (cm yr^{-1}) for 2025 relative to the 2001–15 climatology. Positive values denote ocean freshwater gain. 2025-minus-2024 differences for (b) *P–E*, (c) evaporation (*E*), and (d) precipitation (*P*). Positive (negative) values denote ocean freshwater gain (loss). *P* is the GPCP version 2.3 product, and *E* is from Woods Hole Oceanographic Institution (WHOI) OAFlux2.

3. WIND STRESS

In 2025, wind stress magnitude anomalies were generally weak and negative across much of the tropics (Fig. 3.14a), indicating slightly weaker near-surface winds overall, with the clearest negative anomalies over the tropical Pacific and eastern tropical Indian Ocean. Vector anomalies nevertheless indicate a modest enhancement of the easterly (trade-wind) component in the western/central equatorial Pacific, consistent with weak La Niña conditions, while winds weaken in parts of the eastern tropical Indian Ocean. The tropical Atlantic exhibits a mixed pattern, with localized strengthening in the tropical North Atlantic. In the extratropics, anomalies are larger and more coherent. Over the Antarctic Circumpolar Current (ACC) belt (~40°S–60°S), wind stress exhibits mixed signs, with locally positive anomalies exceeding ~0.02 N m^{-2} (Fig. 3.14a). The North Atlantic also shows strengthened mid- to high-latitude wind stress, whereas the central North Pacific is characterized by negative anomalies (~0.02 N m^{-2}), indicating weaker westerlies there.

The 2025–2024 differences (Fig. 3.14b) underscore these changes, with marked strengthening of westerlies across the Southern Ocean and the North Atlantic, contrasted by weaker wind stress over the central North Pacific midlatitudes. The strengthening of westerlies in the North Atlantic likely contributed to the reduction of meridional overturning circulation at 41°N (see section 3h). In the tropics, the most prominent features are enhanced easterly wind anomalies in the western equatorial Pacific and the tropical North Atlantic.

Wind stress curl drives divergence/convergence of Ekman transport and the associated Ekman pumping velocity, W_{EK}, at the base of the Ekman layer. Here W_{EK} is computed as $W_{EK} = 1/\rho\nabla\times(\tau/f)$, where ρ is seawater density, τ is wind stress, and f the Coriolis parameter. The ±2° band is not calculated to avoid the Coriolis singularity (f=0). The 2025 W_{EK} anomalies (Fig. 3.14c) are predominantly negative (downwelling) over much of the tropical/subtropical ocean, with the strongest signal expressed as a narrow, intense negative band along the equatorial Pacific. Positive (upwelling) anomalies are more spatially confined, occurring in localized equatorial and coastal bands. The 2025–2024 W_{EK} differences (Fig. 3.14d) show enhanced downwelling over the equatorial Pacific and broad subtropical regions, while upwelling differences appear in patches of the Southern Ocean and the subpolar North Atlantic, consistent with the regional wind-stress changes in Fig. 3.14b.

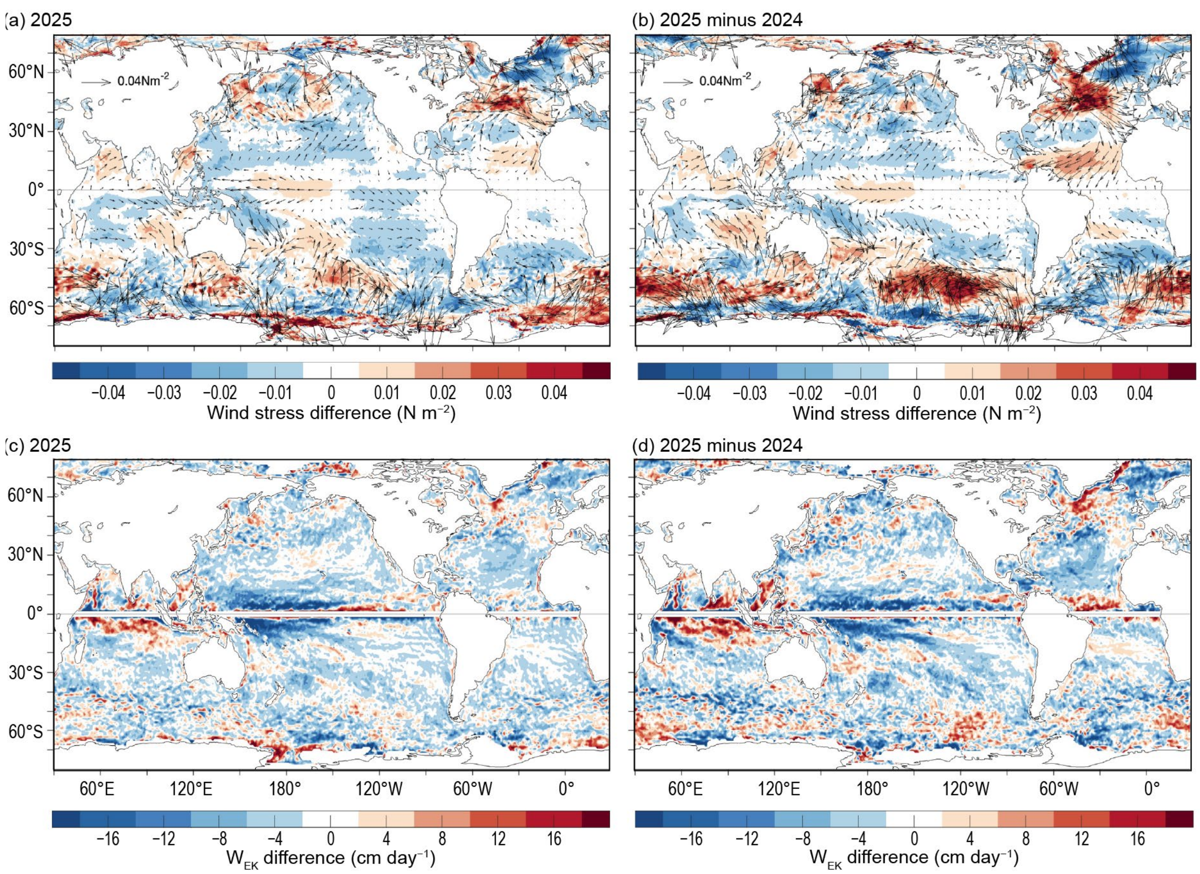

Fig. 3.14. (a) Wind stress magnitude (shaded) and vector anomalies (N m^{-2}) for 2025 relative to a 2001–15 climatology. (b) 2025-minus-2024 differences in wind stress. (c) Ekman vertical velocity (W_{EK}; cm day^{-1}) anomalies for 2025 relative to a 2001–15 climatology. Positive (negative) values denote upwelling (downwelling). (d) 2025-minus-2024 differences of W_{EK}. Wind stress and W_{EK} fields are from Woods Hole Oceanographic Institution (WHOI) OAFlux2.

4. LONG-TERM PERSPECTIVE

A long-term perspective on ocean surface forcing in 2025 is shown using annual-mean time series of Q_{net}, P–E, and wind stress anomalies averaged over the global ice-free ocean (Figs. 3.15a–c). All variables are referenced to the 2001–15 climatological mean. Positive (negative) Q_{net} anomalies indicate increased (reduced) net downward heat flux into the ocean, positive (negative) P–E anomalies indicate increased (reduced) freshwater input, and positive (negative) wind stress anomalies indicate stronger (weaker) surface momentum forcing. Error bars denote one standard deviation of interannual variability.

Annual-mean Q_{net} was relatively stable in the early 2000s, and then rose by ~3±1 W m^{-2} from the 2011 La Niña to a peak greater than 2 W m^{-2} during the strong 2016 El Niño (Fig. 3.15a). Q_{net} declined thereafter during the 2017/18 La Niña and remained reduced through the 2020/23 triple-dip La Niña. By 2025, Q_{net} had recovered and remained slightly negative (~ −0.1 W m^{-2}) relative to the 2001–15 mean state. The *P*–*E* record exhibits pronounced decadal and interannual variability (Fig. 3.15b). After peaking in 2015/16, *P*–*E* reached a minimum around 2021 of approximately −4±2 cm yr^{-1}. In 2025, *P*–*E* remained slightly negative (≈ –1 cm yr^{-1} to –2 cm yr^{-1}), indicating a weak residual salinification tendency relative to the climatological mean. The wind stress time series shows a regime shift in the late 1990s followed by relatively stable behavior since 2000 (Fig. 3.15c). After modest strengthening around 2020/21, wind stress weakened again. In 2025, wind stress anomalies were negative, remaining below the climatological mean and consistent with relatively weak global-mean surface momentum forcing. Together, changes in Q_{net}, *P*–*E*, and wind stress represent variability in air–sea exchanges that both force the ocean and influence the atmosphere through two-way ocean–atmosphere coupling.

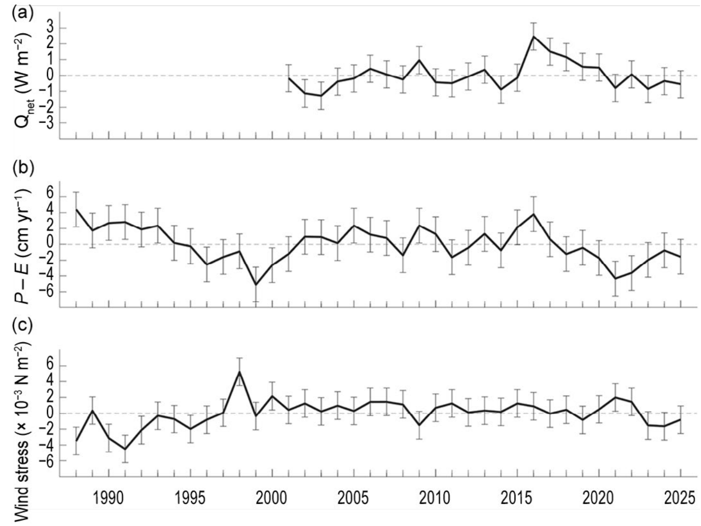

Fig. 3.15. Annual mean time series of global ocean surface (a) net surface heat flux anomalies (Q_{net}; W m^{-2}) from a combination of Clouds and the Earth's Radiant Energy System (CERES) EBAF4.2 short wave (SW) + long wave (LW) and the Woods Hole Oceanographic Institution (WHOI) OAFlux2 latent heat (LH) + sensitive heat (SH). (b) Net freshwater flux anomaly (precipitation [*P*]–evaporation [*E*] cm yr^{-1}) from a combination of GPCP *P* and OAFlux2 *E*. (c) Wind stress magnitude anomalies (N m^{-2}) from OAFlux2. Error bars denote one std. dev. of annual-mean variability.

f. Sea level variability and change

—P. R. Thompson, M. J. Widlansky, B. Beckley, B. D. Hamlington, S. Jevrejeva, F. W. Landerer, E. Leuliette, G. T. Mitchum, R. S. Nerem, J. M. Steinberg, and W. Sweet

Annual average global mean sea level (GMSL) from satellite altimetry (1993–present; Willis et al. 2025) reached a new high in 2025, rising to 111.2 mm above the 1993 mean (Fig. 3.16a). This marks the 14th consecutive year (and 30th out of the last 32) that GMSL increased relative to the previous year, reflecting the combined effects of the ongoing trend and acceleration in GMSL. The average linear trend over the entire altimetry era is 3.5±0.4 mm yr^{-1} (Fig. 3.16a) when corrected for glacial isostatic adjustment (GIA; –0.25±0.1 mm yr^{-1}; Tamisea and Mitrovica 2011; Caron and Ivins 2020), with positive local trends from altimetry over 99% of the ice-free ocean (Fig. 3.16b). However, the global mean rate has increased during this time, and acceleration in GMSL, 0.071±0.06 mm yr^{-2}, has doubled the decadal rate of GMSL rise since 1993 (Hamlington et al. 2024). A quadratic fit with corrections for the eruption of Mt. Pinatubo (Fasullo et al. 2016) yields a climate-driven linear trend of 3.1±0.4 mm yr^{-1} and an acceleration of 0.092±0.025 mm yr^{-2} (updated from Nerem et al. 2018).

The thermosteric (i.e., ocean-warming) contribution to GMSL change over ±65° latitude was 1.6±0.3 mm yr^{-1} during 2005–25 (Fig. 3.16a), which primarily reflects warming of the upper 2000 m of the ocean based on Argo observations (Roemmich and Gilson 2009). The ocean below 2000 m contributes less than 10% of the thermosteric trend based on measurements made by deep Argo floats and ship-based observations (Johnson and Purkey 2024; section 3c). Mass concentration anomalies spanning ±65° latitude from the Gravity Recovery and Climate Experiment (GRACE) and GRACE Follow-On (GRACE-FO) missions (Wiese et al. 2022) show the average mass contribution to GMSL rise during the 2005–25 period was 2.0±0.4 mm yr^{-1} when corrected for GIA (–1.0±0.3 mm yr^{-1}; Caron and Ivins 2020; Fig. 3.16a). The trend in the sum of thermosteric and mass contributions, 3.6±0.5 mm yr^{-1}, agrees within uncertainty with the GMSL trend of 3.9±0.2 mm yr^{-1} measured by altimetry since 2005 (Leuliette and Willis 2011; Chambers et al. 2017), with the thermosteric component contributing to positive

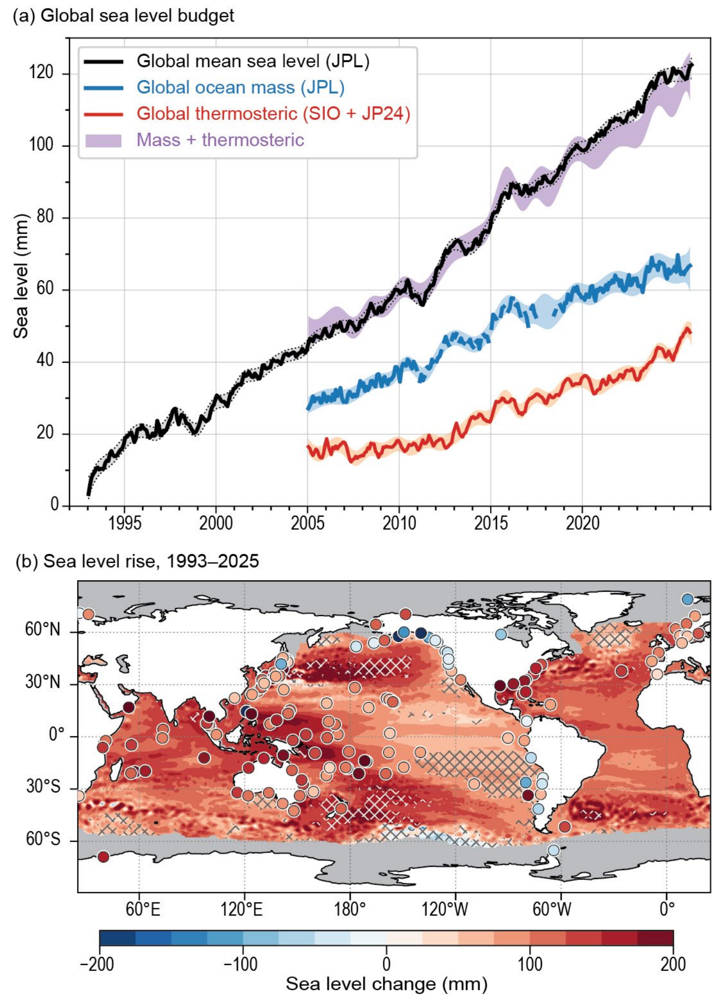

Fig. 3.16. (a) Monthly global mean sea level (GMSL) estimates from satellite altimetry (1993–2025) produced by NASA Jet Propulsion Laboratory (JPL) with support from the NASA Sea Level Change and Ocean Surface Topography Science Teams (black). Monthly global ocean mass (2005–25) from GRACE and GRACE Follow-On (GRACE-FO) calculated from mass concentrations produced by NASA JPL (blue). GRACE and GRACE-FO data within 300 km of land were excluded. Monthly global mean thermosteric sea level (2005–25) from Scripps Institute of Oceanography (SIO) for depths above 2000 m and from Johnson and Purkey (2024; JP24) for depths below 2000 m (red). Shading around the GMSL, mass, and thermosteric series represents a 95% confidence range for annual and longer variations, including glacial isostatic adjustment (GIA) uncertainty for the GMSL and mass time series. The confidence ranges for mass and thermosteric are used to produce a 95% confidence range for the sum of the contributions to GMSL (purple). (b) Total local sea level change during 1993–2025 as measured by satellite altimetry (contours) and tide gauges (circles). Hatching indicates local changes that differ from the change in GMSL by more than one standard deviation. The sea level change map was generated using gridded delayed-mode and near-real-time altimetry data produced by the Copernicus Climate Change Service and obtained from the Copernicus Marine Service. Tide-gauge observations were obtained from the University of Hawaii Sea Level Center Fast Delivery database.

acceleration during this time. Halosteric (salinity-related) contributions are small and typically excluded (Roemmich et al. 2019).

Annually averaged GMSL from altimetry, adjusted for GIA, rose just 1.0±0.5 mm from 2024 to 2025, which is well below the long-term rate of sea level rise (Figs. 3.17a,b). La Niña conditions during early 2025 likely suppressed global sea levels by redistributing fresh water from ocean to land (Figs. 3.13a,b; see Fig. 2.43; e.g., Fasullo et al. 2013), consistent with the modest 0.1±0.6 mm annual increase in global ocean mass from GRACE-FO, which also fell short of the long-term trend. By contrast, global mean thermosteric sea level from Argo rose 3.9±0.8 mm, well above the long-term trend and consistent with the unprecedented increase in ocean temperatures observed during 2025 (Pan et al. 2026).

Reconciling these annual increases in the context of the global sea level budget proves difficult, as the thermosteric increase, third largest in the Argo record, far outpaces the lower-than-expected increases in ocean mass and GMSL. One factor that may reduce the discrepancy is the halosteric contribution, as mentioned earlier. Nevertheless, Argo salinity data show a 1 mm–2 mm decrease in global mean halosteric sea level from 2024 to 2025, which would substantially narrow the gap. The decrease in halosteric sea level aligns with the salinification of the Pacific from 2024 to 2025 (see Fig. 3.10e), assuming it dominates the global average. Differences in spatial sampling may also contribute. For example, Argo undersamples continental shelves and shallow seas, including the southeast Asian seas around the Maritime Continent.

Local sea level anomalies averaged during 2025 were positive over most of the global ocean relative to the 1993–2022 baseline (Fig. 3.17a), consistent with the continuing rise in mean sea level onto which regional variability is superimposed. The anomaly pattern in altimetry observations exhibits pronounced spatial structure across the tropics and midlatitudes, with broad areas of above-normal sea level spanning much of the Indo-western Pacific and additional positive anomalies in almost all parts of the North Pacific and North Atlantic midlatitudes (Fig. 3.17a). In contrast, slightly below-normal sea level is evident across portions of the southern Indian Ocean and equatorial central-to-eastern Pacific, yielding a strong zonal contrast across the tropical Pacific that is more apparent in the seasonal averages when the long-term trend is removed (Figs. 3.17c,d). Tide gauges provide coastal examples of the elevated background sea levels relative to 1993–2022, while generally agreeing with the regional patterns evident in

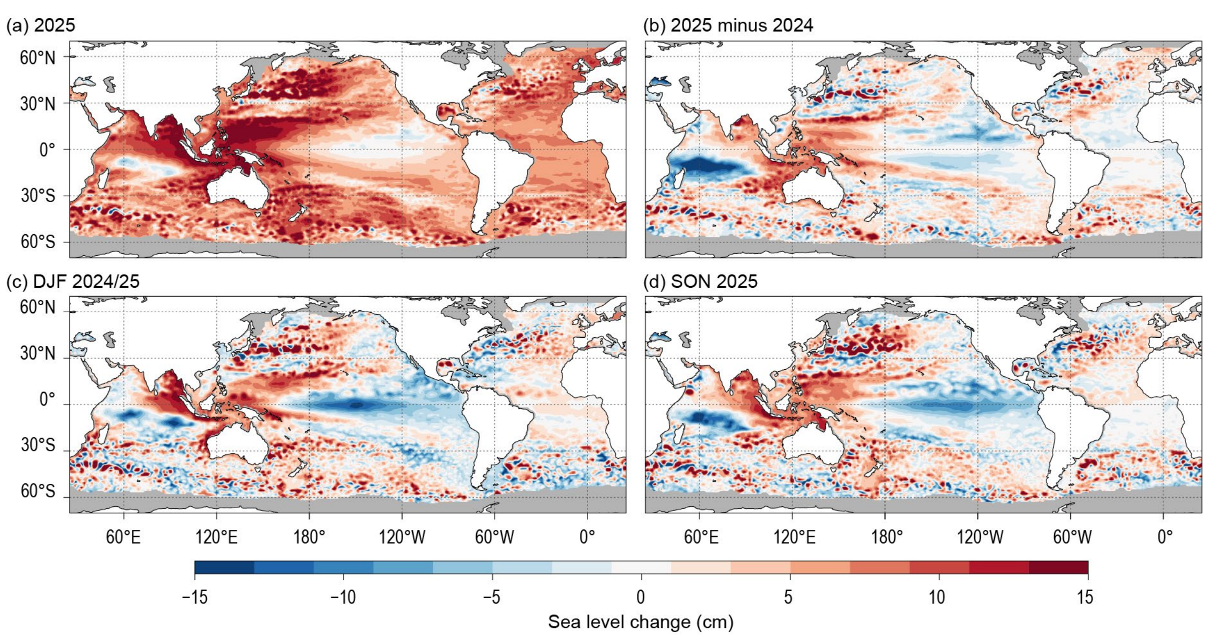

Fig. 3.17. (a) Annual average sea level anomaly during 2025 relative to average sea level at each location during 1993–2022. (b) Average 2025-minus-2024 sea level anomaly. (c) Average sea level anomaly during Dec–Feb (DJF) 2024/25 relative to the 1993–2022 DJF average. (d) Same as (c), but for Sep–Nov (SON). Units are given in cm. Global mean sea level was subtracted from panels (c),(d) to emphasize regional, non-secular change. These maps were generated using gridded delayed-mode and near-real-time altimetry data produced by the Copernicus Climate Change Service and obtained from the Copernicus Marine Service.

the altimetry data (e.g., Woodworth et al. 2019). Tide gauge data (Caldwell et al. 2015) confirm elevated sea levels globally, with especially large positive anomalies in parts of the western Pacific (Fig. 3.17a).

Year-over-year differences (2025 minus 2024) indicate that 2025 featured a substantial reorganization of sea level across the tropical Pacific, with lower sea level in 2025 in much of the tropical central/eastern Pacific and compensating increases elsewhere in the Indo–western Pacific (Fig. 3.17b). The December–February (DJF) and September–November (SON) seasonal maps emphasize a coherent band of negative sea level anomalies along the equator in the central-to-eastern Pacific, together with relatively higher sea level in the off-equatorial western tropical Pacific (Figs. 3.17c,d), consistent with wind-driven changes (Fig. 3.14) that redistribute upper-ocean heat and mass, deepen the thermocline, and alter the zonal sea level slope across the basin (e.g., Widlansky et al. 2014). The El Niño–Southern Oscillation (ENSO) conditions during 2025, as characterized by NOAA's Climate Prediction Center Relative Oceanic Niño Index (RONI), were consistent with two short-lived periods of La Niña conditions (e.g., DJF values near −1.1°C, near-neutral May–July means, and SON values near −0.9°C), supporting the observed tropical Pacific sea level zonal seesaw pattern (Fig. 3.17; Widlansky et al. 2015). Consistent with these basin-scale changes, tide gauges show regionally differing interannual tendencies: 2025 mean sea level (updated through November at the time of writing) increased since 2024 by about 6 cm and 10 cm at Guam and Yap, respectively, while Honolulu and neighboring stations in Hawaii decreased by about −2 cm over the same period. These changes illustrate how ENSO-related dynamic adjustment can produce opposing changes across the basin depending on location and time (e.g., Long et al. 2020).

Outside the Pacific, the 2025 sea level variability also reflects the influence of other climate modes and regional wind stress forcing, particularly in the Indian Ocean and the extratropical basins. The annual anomaly field shows above-normal sea levels in the northern and eastern Indian Ocean, whereas most of the southern Indian Ocean was well below normal (Figs. 3.17a,b). Consistent with this, the Indian Ocean dipole (IOD) index was negative on average in 2025 (see section 4f), a state often associated with wind and thermocline adjustments that can favor relatively higher sea level in the eastern Indian Ocean/Maritime Continent region relative to the western basin. More locally, interannual variability in the tropical Indian Ocean sea level includes contributions from wind forcing (e.g., Ekman suction in the southwestern tropics associated with wind stress curl that shoals the thermocline and reduces sea levels; Fig. 3.14) and covarying climate modes (e.g., IOD and ENSO interactions; Kumar et al. 2020). Along the U.S. West and East Coasts, tide gauges illustrate regionally differing year-over-year changes superimposed on a positive background relative to 1993–2022: year-to-date 2025 mean sea level at San Diego (West Coast) was approximately unchanged relative to 2024 (0 cm) while Charleston (East Coast) was lower by about 5 cm, even though both sites were elevated by about +3 cm to +6 cm relative to the 1993–2022 climatology (through 30 November 2025; Caldwell et al. 2015).

Ongoing trends, interannual variability, and seasonal changes in sea level increase the magnitude and frequency of extreme sea level events, contributing to coastal flooding and erosion (e.g., Wahl et al. 2014; Kendon et al. 2024; Li et al. 2022). Minor impacts occur when water levels exceed the 99th percentile of daily maxima (Sweet et al. 2014). Using 1993–2022 as the baseline, such extreme events have become more frequent in recent years (Sweet et al. 2024). Tide-gauge records with at least 80% completeness during 1993–2025 and in both 2024 and 2025 show that the median number of extreme events per year increased from one during 1993–97 to five during 2021–25, while the 90th percentile rose from six to 18 events per year.

Thirty-six of the 116 locations experienced more than 10 extreme sea level events during 2025 (Fig. 3.18a). These locations were distributed around the global ocean and were concentrated in areas where sea level trends and/or annual sea level anomalies were largest (Figs. 3.16a, 3.17b). The greatest number of extreme events occurred in the western Pacific, especially Guam and Yap, where annual 2025 sea level anomalies were especially high due to La Niña conditions. Relative to 2024, more locations experienced large decreases in the number of extremes during 2025 compared to large increases (Figs. 3.16b, 3.17d). The lone exception was the western Pacific, where the large number of extremes during 2025 in Guam and Yap represented substantial increases over the previous year (Fig. 3.18c).

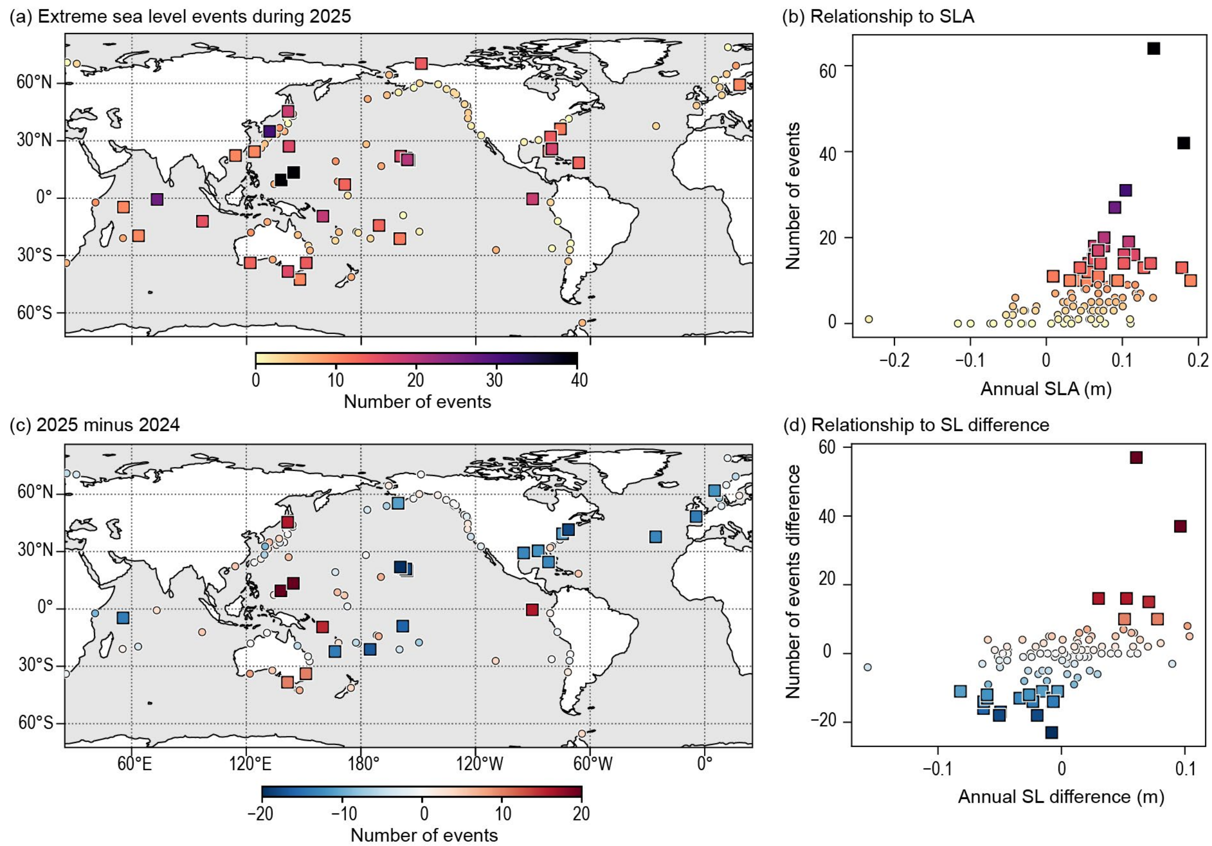

Fig. 3.18. (a) Number of extreme sea level (SL) events from tide gauges during 2025. (b) Counts in (a) as a function of annual sea level anomaly (SLA) during 2025. Square markers in (a) and (b) highlight locations with more than 10 extreme events. (c) Change in number of extreme sea level events from 2024 to 2025. (d) Counts in (c) as a function of the change in annual sea level from 2024 to 2025. Square markers in (c) and (d) highlight locations where the magnitudes of changes in counts of extreme events were greater than 10. Counts of extreme sea level events were calculated from hourly tide gauge observations obtained from the University of Hawai'i Sea Level Center Fast Delivery database.

g. Surface currents

—M. Le Hénaff, R. C. Perez, and F. P. Tuchen

This section describes variations of ocean surface currents, transports, and associated features, such as rings. Here, geostrophic surface current estimates are obtained from in situ and satellite observations. See Lumpkin et al. (2012) for details of these calculations. Zonal geostrophic current anomalies are calculated with respect to a 1993–2020 climatology and are discussed below for individual ocean basins.

Near-surface in situ measurements (12-m depth or shallower) are available from seven mooring sites in the tropical Atlantic, three sites along the equator in the tropical Pacific, and six sites along 65°E Indian Ocean, as part of the Global Tropical Moored Buoy Array (GTMBA; e.g., McPhaden et al. 2023). In August–September 2025, as part of the National Data Buoy Center (NBDC) recapitalization of the Tropical Atmosphere Ocean (TAO) array and a NBDC, Pacific Marine Environmental Laboratory (PMEL), and Atlantic Oceanographic and Meteorological Laboratory (AOML) collaboration, 17 acoustic current meters and six acoustic doppler current profilers (ADCPs) were deployed at TAO mooring locations between 165°E and 155°W and 2°S to 2°N as part of a Tropical Pacific Observing System (TPOS) field experiment to resolve the upper ocean jets in the western equatorial Pacific.

1. PACIFIC OCEAN

In 2025, zonal geostrophic currents in the equatorial Pacific (Fig. 3.19a) exhibited annual mean westward (negative) current anomalies exceeding –10 cm s^{-1} in the western portion of the equatorial band, between 2°S and 2°N and between 155°E and 170°E, with the strongest anomalies of –20 cm s^{-1} at 158°E and 0.5°S. The rest of the equatorial band in the Pacific does not show marked anomalies. Since 2024 presented intense negative anomalies across the whole basin (Lumpkin et al. 2025), the 2025-minus-2024 difference map (Fig. 3.19b) shows a weakening relative to the previous year with eastward anomalies of 10 cm s^{-1} covering most of the equatorial waveguide in the Pacific basin.

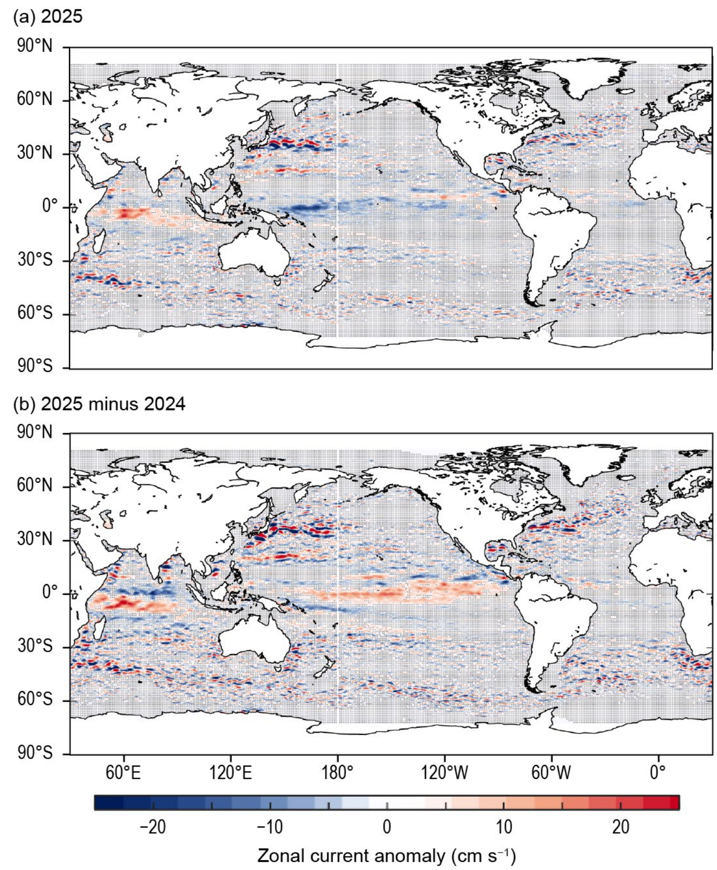

Fig. 3.19. Annually averaged geostrophic zonal current anomalies (cm s^{-1}) with respect to the 1993–2020 climatology for (a) 2025 and (b) 2025 minus 2024. Values are only shown where they are significantly different from zero.

Westward anomalies exceeding –20 cm s^{-1} were present in the western equatorial Pacific in December 2024–February 2025 (Fig. 3.20a) between 2°S and 1°N, and between 150°E and 160°W. Significant westward anomalies extended to 6°S between 160°E and 160°W, and to 6°N between 160°W and 140°W. These anomalies are consistent with the weak La Niña conditions observed at the end of 2024 (see section 4b). In March–May, eastward anomalies of 10 cm s^{-1}–20 cm s^{-1} developed in the central and eastern parts of the basin, between 160°W and 90°W, and between 1°S and 3°N, associated with more neutral ENSO conditions. The equatorial anomalies reversed again to westward anomalies in June–August in the central to eastern part of the basin, between 150°W and 105°W, and between the equator and 3°N, exceeding –10 cm s^{-1}, as weak La Niña conditions began to develop again. North of this pattern, eastward anomalies exceeding 20 cm s^{-1} between 140°W and 120°W were associated with an accelerated North Equatorial Countercurrent. The westward anomalies intensified in September–November, covering most of the equatorial band between 2°S and 4°N and exceeding –20 cm s^{-1} between 160°E and 180°E near the equator, and are associated with the development of more marked La Niña conditions.

In 2020–25, the annual-average latitude of the Kuroshio Extension in the region 141°E–153°E, 32°N–38°N was shifted north of its long-term (1993–2025) location of 35.5°N, to a maximum of 36.8°N in 2021 and to 36.5°N in 2025 (Fig. 3.21c). This can be seen as alternating eastward/westward current anomalies in Fig. 3.19a that persisted through the year (Fig. 3.20). This 2020–25 northward shift of the Kuroshio Extension corresponded with a multiyear increase in averaged eddy kinetic energy (EKE; Fig. 3.21d), associated with a large meander of the Kuroshio Current off the southern coast of Japan (Qiu et al. 2020). Initiated since 2017 (Qiu and Chen 2021), this large meander ended in 2025, as seen in the altimetry data (Fig. 3.21b).

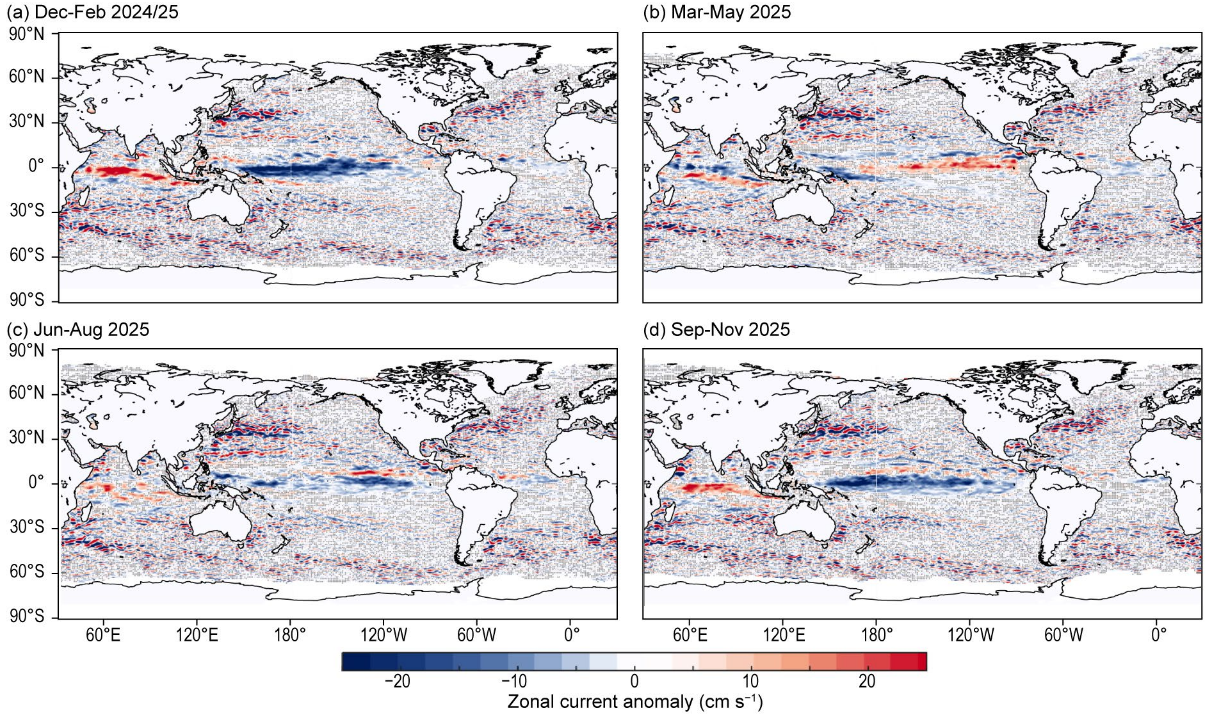

Fig. 3.20. Seasonally-averaged zonal geostrophic anomalies (cm s^{-1}) with respect to 1993–2020 seasonal climatology for (a) Dec–Feb 2024/25, (b) Mar–May 2025, (c) Jun–Aug 2025, and (d) Sep–Nov 2025. Values are only shown where they are significantly different from zero.

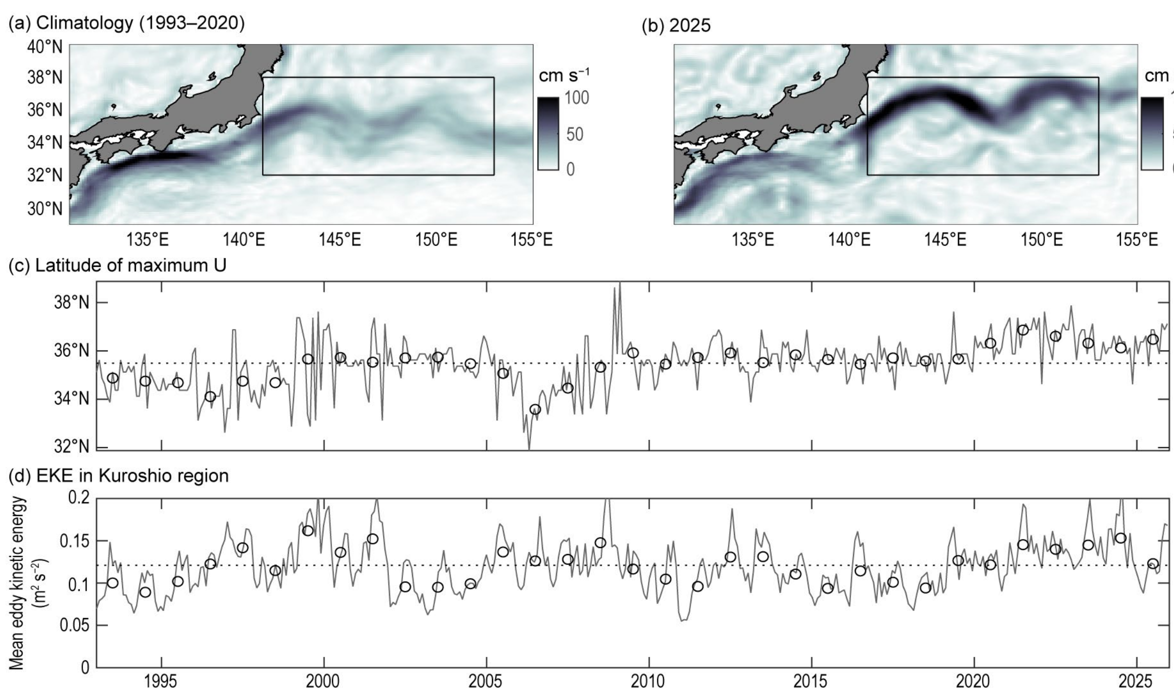

Fig. 3.21. (a) Climatological geostrophic surface current speed (cm s^{-1}) from Mulet et al. (2021) and (b) 2025 mean geostrophic currents from MDT13 Mean Dynamic Topography (Rio et al. 2014) and Copernicus near-real-time altimetry in the Kuroshio Current region (box) and surrounding regions. (c) Latitude of maximum zonal currents averaged in the Kuroshio Current region. (d) Mean eddy kinetic energy (EKE; m^2 s^{-2}) in the Kuroshio region.

2. INDIAN OCEAN

Annually averaged geostrophic zonal current anomalies in the Indian Ocean (Fig. 3.19a) exhibited eastward anomalies exceeding 10 cm s^{-1} between 6°S and the equator and between 55°E and 75°E, reaching 20 cm s^{-1}–25 cm s^{-1} locally. Because the equatorial currents presented eastward anomalies centered on the equator with westward anomalies south of that pattern, the 2025-minus-2024 difference map (Fig. 3.19b) shows a dipole pattern of negative anomalies between 1°S and 2°N, and positive anomalies south of it. During December 2024–February 2025 (Fig. 3.20a), eastward anomalies exceeding 25 cm s^{-1}–30 cm s^{-1} were present across the equatorial band. These were replaced by westward anomalies of up to 25 cm s^{-1} in March–May 2025 (Fig. 3.20b) near the equator, which disappeared in June–August (Fig. 3.20c). Eastward anomalies of 20 cm s^{-1}–30 cm s^{-1} developed in the central basin at 55°E–85°E, 3.5°S–0.5°N in September–November (Fig. 3.20d), with peak values of 35 cm s^{-1} at 80°E, 1°S reflecting an acceleration of the seasonal Southwest Monsoon Current.

3. ATLANTIC OCEAN

Annual mean geostrophic zonal current anomalies in the tropical Atlantic Ocean in 2025 did not exceed ±5 cm s^{-1} (Fig. 3.19a). Because a similar situation was observed in 2024, the 2025-minus-2024 difference map (Fig. 3.19b) is not remarkable. Westward –(5–10) cm s^{-1} anomalies were present between 1°S and 3°N in the central part of the basin in December 2024–February 2025 (Fig. 3.20a) and in March–May 2025 (Fig. 3.20b), before disappearing in June–November (Figs. 3.20c,d). During June–August 2025, the tropical Atlantic (20°W–0°, 3°S–3°N) exhibited an Atlantic Niña event with sea surface temperature anomalies below −0.5°C persisting for three consecutive months (Tuchen 2025). Such cold events are commonly associated with a seasonal intensification of easterly trade winds and westward surface currents. Accordingly, anomalous westward surface currents emerged during the onset phase of the cold sea surface temperature anomalies, resembling the evolution of the weaker but more rapidly developing cold event observed in 2024 (Tuchen et al. 2025).

In the subtropical North Atlantic, comparable to 2024, a band of strong positive and negative anomalies of magnitude 15 cm s^{-1}–20 cm s^{-1} east of Cape Hatteras (Fig. 3.19a) indicated that the Gulf Stream extension east of Cape Hatteras was shifted anomalously northward in 2025 compared to the long-term mean. This anomalous banding persisted throughout the year (Fig. 3.20b).

4. METHODOLOGICAL ADVANCES

In terms of ocean surface current retrieval methodologies, several approaches, all based on machine learning (ML), were developed in 2025. Sun et al. (2025), Shao et al. (2025), and Bai et al. (2025) applied various ML techniques to retrieve ocean current information from Sentinel-1 synthetic aperture radar (SAR) data, which has been a significant challenge since the inception of SAR imagery. Blending standard satellite altimetry, satellite wind estimates, and surface drifter data, Ge et al. (2025) implemented a deep learning approach to reconstruct near-surface currents. Also using deep learning, Garcia et al. (2025) used standard and Surface Water and Ocean Topography (SWOT) altimetry, together with surface drifters, to estimate geostrophic surface currents and forecast them over seven days. Finally, Ciani et al. (2025) developed a deep learning method to estimate surface currents from standard altimetry and high-resolution sea surface temperature images. These efforts illustrate how machine learning allows the retrieval of surface currents estimates from a wide range of platforms.

h. Atlantic meridional overturning circulation and heat transport

—D. L. Volkov, S. Dong, T. Petit, J. K. Willis, W. Hobbs, Y. Fu, R. C. Perez, B. Moat, D. Smeed, S. Elipot, and M. S. Lozier.

The upper limb of the meridional overturning circulation (MOC) transports large quantities of heat and seawater properties across the South and North Atlantic toward the North Pole and plays a key role in shaping regional and global climate, weather, and ocean variability patterns. The MOC volume transport and associated meridional heat transport (MHT) have been observed using moored arrays and synthetic estimates combining satellite altimetry and in situ data at selected latitudes (Fig. 3.22). Here, we present, from north to south, updated time series of the MOC and MHT from the Overturning in the Subpolar North Atlantic Program (OSNAP), RAPID-Meridional Overturning Circulation and Heat-flux Array-Western Boundary Time Series (RAPID-MOCHA-WBTS; hereafter, RAPID), and synthetic estimates at 41°N, 20°S, 25°S, 30°S, and 34.5°S. Updates from the Meridional Overturning Variability Experiment (MOVE), Tropical Atlantic Circulation and Overturning at 11°S (TRACOS), and South Atlantic Meridional overturning Basin-wide Array (SAMBA) moored arrays (black lines in Fig. 3.22) are pending. Due to logistical constraints, only the synthetic MOC and MHT estimates extend through 2025.

The recently extended OSNAP MOC and MHT time series spans August 2014 to July 2022 (Fig. 3.23a). Over this period, the time–mean MOC across the full OSNAP array, comprising OSNAP West between Labrador and West Greenland and OSNAP East between East Greenland and Scotland (Lozier et al. 2017), is 16.5±3.3 Sverdrup (Sv; mean±standard deviation). Mean overturning is 16.4±2.9 across OSNAP East and 2.7±1.3 Sv across OSNAP West, with OSNAP East dominating both the mean and variability, consistent with previous studies (e.g., Lozier et al. 2019). The full-array OSNAP MOC is defined as the maximum of the combined streamfunction, so it does not equal the sum of the individual East and West maxima, which occur at different density levels. The annual mean MOC in 2021 was near the record mean, while the January–July 2022 average was ~1 Sv lower but remained within uncertainty bounds. Using the extended record, Fu et al. (2025) showed that surface buoyancy-driven water-mass transformation explains up to 30% of interannual MOC variability in both subpolar basins. No statistically significant MOC and MHT trends are evident over the eight-year period.

Overturning at OSNAP East and OSNAP West is anti-correlated on interannual timescales, with a maximum correlation of −0.64 when OSNAP East leads by a few months (Fu et al. 2025), indicating partial compensation between the eastern and western segments. The time–mean MHT across the full OSNAP array is 0.51±0.06 PW, dominated by OSNAP East (0.42±0.06 PW) with a smaller fraction from OSNAP West (0.08±0.02 PW). The MOC–MHT correlation is 0.7, indicating that overturning variability largely controls heat transport, with important contributions from gyre circulation and temperature structure. Petit et al. (2025a) showed that variability in MOC strength measured at OSNAP does not directly reflect changes at midlatitudes; instead, the density at which maximum overturning occurs in the subpolar North Atlantic acts as a key precursor to midlatitude MOC variability. This underscores that OSNAP and

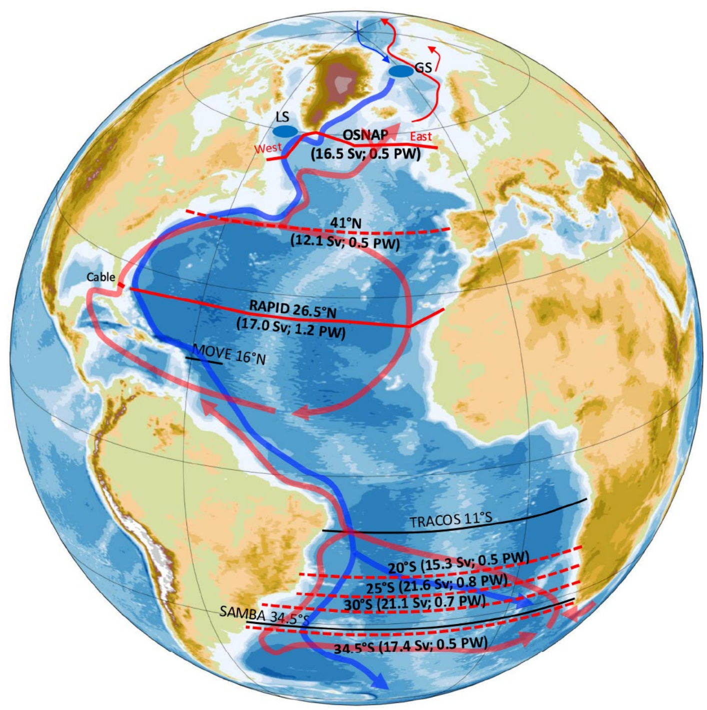

Fig. 3.22. The Atlantic meridional overturning circulation (MOC)/meridional heat transport (MHT) observing network: moored arrays (solid red and black lines) and sections across which the MOC/MHT is estimated by synthesizing in situ measurements (Argo, eXpendable BathyThermograph [XBT]) with satellite altimetry data (dashed red lines). The red lines show the sections that have updates covered in this report, while the black lines show the sections for which updates are pending. The updated record mean MOC/MHT values are shown in parentheses. Red arrows show flows associated with the upper limb of the MOC and blue arrows show deeper limb of the MOC.

subtropical and tropical observing systems farther south capture different aspects of MOC variability, and that OSNAP density structure may help interpret meridional MOC coherence in the North Atlantic.

The MOC estimates at 41°N (Fig. 3.23b), derived from satellite altimetry sea surface height (SSH) and Argo observations, are reproduced from Willis (2010) and Hobbs and Willis (2012) and extended from January 2002 through December 2025 (Willis and Hobbs 2026). Each estimate represents a three-month moving average, with uncertainties of 2.3 Sv for the MOC and 0.23 PW for the MHT. The time–mean MOC and MHT are 12.1 Sv and 0.47 PW, respectively. The smaller MOC at 41°N compared to OSNAP can reflect both methodological differences and a real northward increase in overturning due to subpolar water-mass transformation. The annual-mean MOC was 14.7 Sv in 2023, increased to 16.0 Sv in 2024, and declined to 13.0 Sv in 2025. Both MOC and MHT weakened in 2025, returning within the uncertainty range of the long-term mean; only the 2023 and 2024 values remain statistically distinct. The 2025 weakening was likely contributed to by the observed strengthening of the anticyclonic wind circulation in the subtropical North Atlantic (see Figs. 3.14a,b) through enhanced southward Ekman transport at 41°N and the corresponding geostrophic adjustment. A strong MOC-MHT correlation (0.9) indicates that large-scale overturning variability is the primary driver of meridional heat transport at this latitude. On interannual to decadal time scales, the 24-year record shows extended periods of positive (2004–08 and 2022–25) and negative (2009–21) anomalies. As quality control of Argo and altimeter data is continuously updated, refinements to the estimates are expected. Updates since the *State of the Climate* report in 2024 (Volkov et al. 2025a), including improved Argo quality control and higher-resolution altimetry grids, reduced the 2023 and 2024 annual-mean MOC estimates by 0.4 Sv and 0.2 Sv, respectively. These adjustments are smaller than the year-to-year uncertainty, and the elevated MOC values in 2023/24 remain unusually high relative to the previous two decades.

The RAPID array at 26.5°N has provided continuous, basin-wide observations of the Atlantic MOC since 2004, forming the longest observational record of the MOC, now extended through March 2024 (Fig. 3.23c; Moat et al. 2026). Florida Current transport—the primary contributor to northward flow in the upper limb of the MOC at this latitude—has historically been estimated from submarine cable measurements. Following a cable failure in November 2023, transport is now derived from cross-stream pressure gauges and altimetry (Volkov et al. 2025b). While the impact of this change on the MOC estimates is still under investigation, preliminary assessments indicate that low-frequency variability and trends remain unchanged. Petit et al. (2025b) evaluated the sensitivity of RAPID MOC estimates to the array design and showed that while moorings in the upper 3000 m and at the western boundary are essential, deep eastern boundary and Mid-Atlantic Ridge moorings can be replaced by repeat hydrographic sections with only a small additional error (~0.3 Sv).

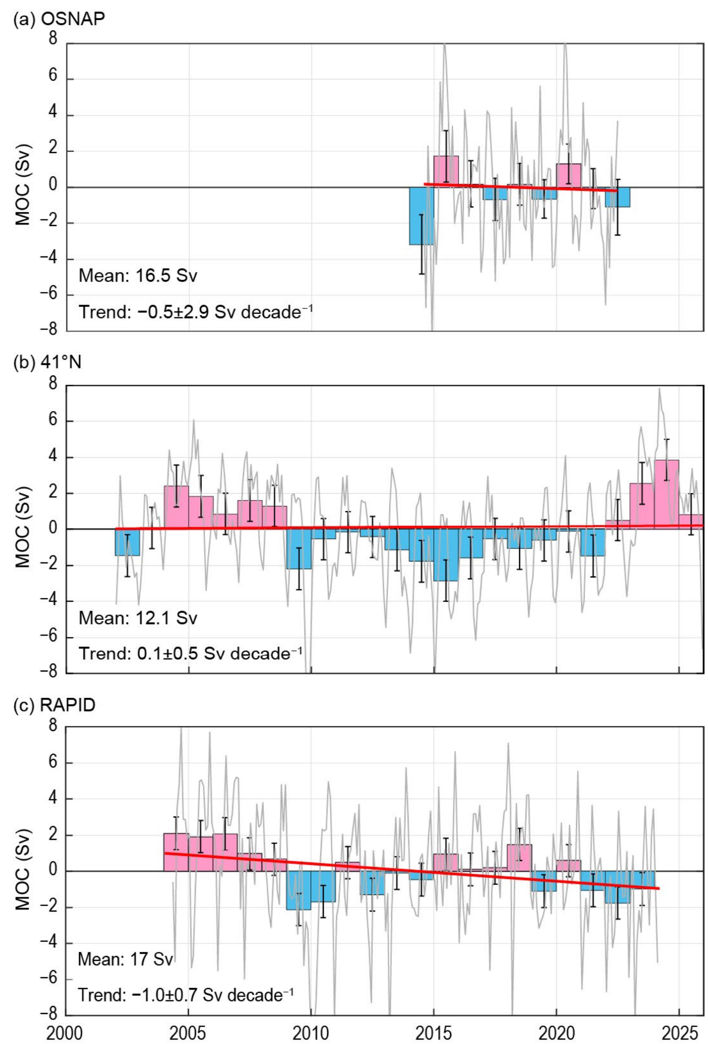

Fig. 3.23. Monthly (gray lines) and annual (bars) estimates of meridional overturning circulation (MOC) anomalies (Sverdrup [Sv]) in the North Atlantic: (a) Overturning in the Subpolar North Atlantic Program (OSNAP) array, (b) 41°N section, and (c) RAPID array. Error bars indicate uncertainties of annual mean values. Trends are shown by red lines.

The mean MOC at the RAPID array in 2023—the most recent full year in the currently available record—was ~1 Sv below the long-term mean of 16.9 Sv, but remained within uncertainty bounds (Fig. 3.23c), following statistically significant reductions in 2021 and 2022. In contrast to the positive anomalies observed at 41°N during 2022/23, this pattern indicates divergence within the subtropical gyre. Following a reassessment of Florida Current transport that reduced the previously inferred long-term MOC decline by ~40% (Volkov et al. 2024), a modest weakening trend of –1.0±0.7 Sv decade^{-1} remains. This rate is broadly consistent with climate model projections (Weijer et al. 2020) but inconsistent with collapse scenarios suggested by some statistical models (McCarthy et al. 2025). At 26.5°N, MOC and MHT are strongly correlated (r = 0.97), indicating that most poleward heat transport is carried by the overturning circulation (Johns et al. 2023). While the 2004–23 MOC trend is marginally significant, the corresponding MHT trend (–0.03±0.07 PW decade^{-1}) is not statistically significant. A recent study combining RAPID observations with repeated Florida Straits sections and Argo data estimated the overturning streamfunction at 26.5°N in density coordinates (Smeed et al. 2026). The density-based MOC in Smeed et al. (2026) was slightly stronger than the depth-based estimate and more clearly captured subtropical gyre overturning, although variability remained closely aligned with the depth-based MOC.

In the South Atlantic, synthetic estimates of the MOC and MHT at 20°S, 25°S, 30°S, and 34.5°S —reproduced from Dong et al. (2015, 2021)—have been extended through December 2025 (only MOC is shown in Fig. 3.24). The updated estimates incorporate a reprocessed relationship between satellite altimeter SSH anomalies and vertical temperature structure, based on more than a decade of additional hydrographic observations, and a higher-resolution (0.125°) SSH product for deriving temperature profiles. As in the North Atlantic, the MOC and MHT time series at these latitudes are strongly correlated (r = 0.84–0.97). In 2025, statistically significant positive MOC and MHT anomalies occurred only at 25°S and 30°S. On interannual time scales, variability is coherent between 25°S and 35°S, with significant increasing trends. Detrended annual MOC and MHT estimates at 20°S, 25°S, and 30°S are significantly correlated with one another at near-zero lag (r = 0.6–0.8), whereas correlations with 34.5°S are weaker, with statistically significant relationships only between 30°S and 34.5°S. The reduced coherence of MOC and MHT at 34.5°S relative to latitudes farther north likely reflects regional dynamics associated with Agulhas leakage and the Brazil–Malvinas Confluence. Regarding the robustness of the estimates, it should be noted that the standard deviation of the monthly synthetic MOC at 34.5°S (2.7 Sv) is substantially smaller than that derived from the SAMBA moored array (7.6 Sv; Volkov et al. 2025a), although their monthly anomalies are moderately correlated (r = 0.65). Ongoing community efforts are investigating discrepancies between synthetic and mooring-based estimates, potentially arising from differences in instrumentation, sampling, and methodology.

Together, these observations highlight the importance of sustained, basin-wide monitoring for characterizing Atlantic MOC variability and change. Variability across latitudes is dominated by short- to interannual

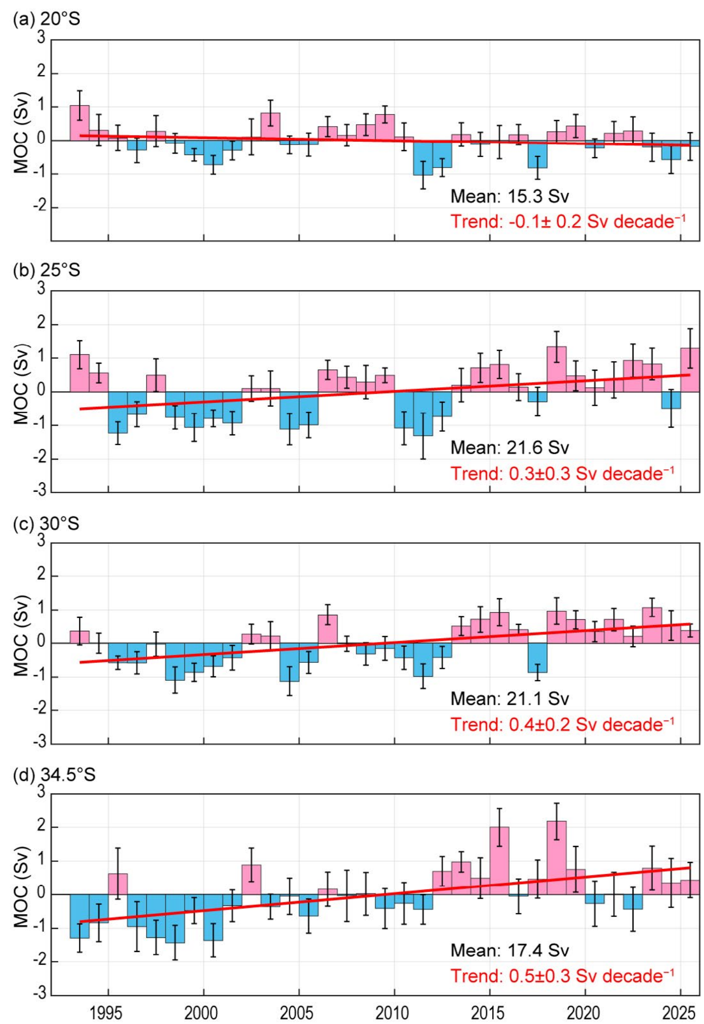

Fig. 3.24. Annual estimates of meridional overturning circulation (MOC) anomalies (Sverdrup [Sv]) and their associated standard errors (error bars) in the South Atlantic, at (a) 20°S, (b) 25°S, (c) 30°S, and (d) 34.5°S. Trends are shown by red lines.

time scales, with no statistically robust evidence of a persistent basin-wide weakening, despite a modest trend at 26.5°N, while positive trends persist in the subtropical South Atlantic. It is acknowledged that the observational time series may still be too short to detect a centennial MOC decline that is projected by climate models and proxy-based reconstructions (e.g., Weijer et al. 2020; Rahmstorf et al. 2015). There is, however, new observational evidence of a coherent multidecadal decline in the Deep Western Boundary Current transport across the tropical/subtropical North Atlantic, indicating a weakening of the lower limb of the Atlantic MOC (Xing et al. 2026). Meridional coherence of the MOC varies, with stronger coherence evident among subtropical latitudes in the South Atlantic and weaker or no coherence in regions influenced by distinct regional dynamics. The complementary use of moored arrays and the synthetic estimates based on satellite and in situ data provides a resilient observing system for detecting change and refining MOC assessments, which remains essential for advancing understanding of the Atlantic's role in the climate system.

i. Global ocean phytoplankton

—B. A. Franz, I. Cetinić, M. Gao, and T. K. Westberry

Marine phytoplankton are microscopic algae that perform a vital function in global ecosystems, generating approximately 50% of Earth's oxygen and newly synthesized organic matter through photosynthesis. In addition to supporting the oceanic food web as primary producers, phytoplankton are a crucial component of the biological pump, capturing carbon dioxide from the atmosphere and transporting it to the deep ocean for long-term storage (Field et al. 1998; Siegel et al. 2023). Phytoplankton distribution and abundance are shaped by multiple interacting factors. Biological factors such as predation by zooplankton and infection by viruses control population size, while environmental factors including nutrient concentrations, light availability, water temperature, ocean stratification, and circulation patterns determine rate of growth (Behrenfeld et al. 2006). Satellite-based ocean color sensors provide a global perspective on phytoplankton dynamics by measuring two key indicators in surface waters: chlorophyll-*a* (Chl *a*; mg m^{-3}) and phytoplankton carbon (C_{phy}; mg m^{-3}). Chlorophyll-*a* is the primary photosynthetic pigment and reflects both the abundance of phytoplankton present and their physiological condition. In contrast, phytoplankton carbon provides a direct measurement of biomass, independent of physiological changes. While Chl *a* and C_{phy} often covary, discrepancies between these two measurements provide valuable insights into phytoplankton community dynamics, such as shifting physiological or compositional makeup of phytoplankton communities (Geider et al. 1997; Cetinić et al. 2012; Siegel et al. 2013; Westberry et al. 2016, Stoer and Fennel 2024).

This report evaluates the global distribution of phytoplankton from October 2024 through September 2025. The assessment uses remotely-sensed Chl *a* and C_{phy} measurements from a continuous 28-year record (October 1997–September 2025) that combines observations from three satellite sensors: SeaWiFS (October 1997–September 2003), MODIS on *Aqua* (MODIS-A, October 2002–September 2018), and VIIRS on NOAA20 (VIIRS-N20, October 2018–September 2025). To provide context on the physical state of the oceans, daytime sea surface temperature (SST) from MODIS-A is also assessed over a common time period. The Chl *a* product was derived using the Ocean Color Index algorithm originally developed by Hu et al. (2012), but with updated algorithm coefficients (Hu et al. 2019; O'Reilly and Werdell 2019). The C_{phy} product was derived in two steps: first, calculating the particle backscattering coefficient (b_{bp}) at 443 nm using the Generalized Inherent Optical Properties algorithm (Werdell et al. 2013; McKinna et al. 2016), then applying a linear relationship between b_{bp} and C_{phy} (Graff et al. 2015).

Creating a seamless multisensor time series requires careful bias correction between the different instruments. To merge SeaWiFS and MODIS-A observations, differences between the sensors were assessed during their overlapping period from 2003 through 2008. A mean bias correction of −0.0021 mg m^{-3} for Chl *a* and -6.7×10^{-5} m^{-1} for b_{bp} (equivalent to −0.78 mg m^{-3} of C_{phy}) was derived and applied to the SeaWiFS time series. Similarly, the overlap period from 2018 to 2020 was used to assess differences between MODIS-A and VIIRS-N20, resulting in a bias correction of −0.0021 mg m^{-3} for Chl *a* and -3.1×10^{-4} m^{-1} for b_{bp} (equivalent to −3.6 mg m^{-3} of C_{phy}) that was applied to the VIIRS-N20 time series. It is important to note that the bias corrections between VIIRS-N20 and MODIS-A b_{bp} retrievals are relatively large, primarily due to residual sensor radiometric calibration errors and the sensitivity of b_{bp} retrievals to spectral sampling differences between the sensors (Werdell and McKinna 2019). While NASA efforts are underway to reduce this retrieval bias, some additional caution is warranted when interpreting C_{phy} anomalies from VIIRS-N20 relative to the climatological record, which is dominated by MODIS-A observations. Nevertheless, the VIIRS-N20 instrument demonstrates very good temporal stability (Twedt et al. 2022) and, therefore, provides the primary reference for assessing changes during the current analysis year.

Changes in the global distribution of phytoplankton were assessed by comparing current observations to historical baselines. For each month during the 2025 analysis year, VIIRS-N20 measurements of Chl *a* and C_{phy} were compared against VIIRS-N20 monthly means spanning October 2019 through September 2024. These monthly anomalies were then averaged to produce global annual mean anomaly maps for both Chl *a* and C_{phy} (Figs. 3.25a,b). The same approach and reference period was applied to MODIS-A SST data to generate an equivalent SST annual mean anomaly map (Fig. 3.25c). The analyses presented in Figs. 3.25 and 3.26 utilize the full 28-year bias-corrected multisensor record, but focus specifically on the permanently stratified ocean (PSO), a region that encompasses the tropical and subtropical oceans. The PSO is defined by two key characteristics: annual average SST exceeding 15°C and surface mixed layers that are typically shallow and nutrient-depleted, remaining above the nutricline (the depth below which nutrient concentrations increase). This region extends roughly between 40°S and 40°N latitude, as indicated by the black lines in Figure 3.25 (Behrenfeld et al. 2006).

For the 2025 analysis year, the distribution of SST anomalies (Fig. 3.25c) is consistent with La Niña conditions over much of the analysis year, including a pronounced tongue of anomalously cool waters extending across the equatorial Pacific. Negative SST anomalies within the PSO are typically associated with a deeper surface mixed layer (Deser et al. 2010), which reduces phytoplankton light exposure rates leading to higher cellular Chl *a* and a decoupling between Chl *a* and C_{phy} variability (Behrenfeld et al. 2016; Graff et al. 2016; Stoer and Fennel 2024). Consistent with that expectation, Chl *a* anomalies were elevated for this analysis year (>30%) within the cooler water of the equatorial Pacific and depressed (<20%) in the anomalously warm waters of the subtropical and subpolar Pacific and the Indian Ocean (Fig. 3.25a). While C_{phy} and Chl *a* anomalies largely covary within the PSO, C_{phy} is elevated where Chl *a* is depressed in the subtropical western North Pacific, with the opposite relationship to the east. Patches of elevated and depressed Chl *a* are visible throughout the subpolar and polar regions above and below the PSO (Fig. 3.25a), and the C_{phy} anomalies show higher spatial variability and dynamic range (Fig. 3.25b). Observed heterogeneity in biomass indicators outside of the PSO are a result of the ephemeral nature of phytoplankton blooms in these waters, as well as poor spatial and temporal sampling due to clouds and low-light conditions and the confounding influence of wind-driven whitecaps (Randolf et al. 2014) that limit our ability to interpret interannual variability in higher latitude regions.

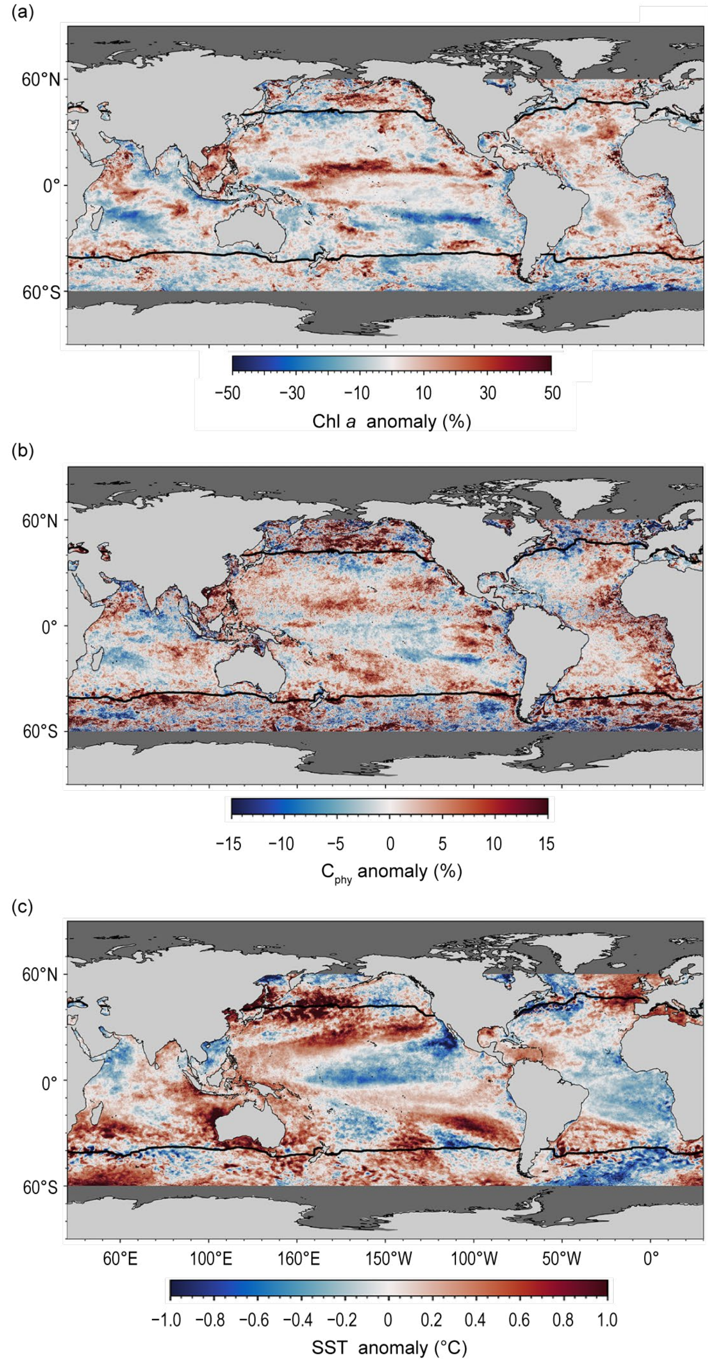

Fig. 3.25. Spatial distribution of average monthly (a) VIIRS-N20 Chl *a* anomalies (%), (b) VIIRS-N20 C_{phy} anomalies (%), and (c) Moderate Resolution Imaging Spectroradiometer on *Aqua* (MODIS-A) sea surface temperature (SST) anomalies (°C) for Oct 2024–Sep 2025, where monthly differences were derived relative to the VIIRS-N20 mission period (Oct 2019–Sep 2024). Chl *a* and C_{phy} are stated as % difference from climatology, while SST is shown as an absolute difference. Also shown in each panel is the location of the mean 15°C SST isotherm (black lines) delineating the permanently stratified ocean (PSO). Differences in the SST anomalies here vs. in Fig. 3.2a are owing to differences in climatological periods, smoothing, and data sources.

Annual variability of Chl *a* and C_{phy} within the permanently stratified ocean typically exhibits two distinct peaks (Figs. 3.26a,b), corresponding to springtime increases in phytoplankton biomass in the Northern Hemisphere (Figs. 3.26c,d) and Southern Hemisphere (Figs. 3.26g,h).

Notably, the timing of C_{phy} peaks lags two to three months behind those of Chl *a*. This lag reflects two important biological processes: the tight coupling between phytoplankton and its losses (mostly through zooplankton grazing) keep biomass in check long after nutrient-driven increases in growth give rise to corresponding increases in cellular Chl *a*, and subsequently the phytoplankton chlorophyll-to-carbon ratios decline as the seasonal bloom progresses (Westberry et al. 2016). The timing of seasonal peaks and troughs observed during the 2025 analysis year is consistent with the climatological record (averaged over the period of October 1997 to September 2024). In the equatorial region, Chl *a* was slightly elevated in February and again in July–August of 2025, consistent with weak La Niña conditions, but otherwise remained close to climatological monthly means (Figs. 3.26e,f). In the Northern Hemisphere, for both Chl *a* and C_{phy} (Figs. 3.26c,d), the magnitude of the spring peak was slightly depressed, while in the Southern Hemisphere the peak was elevated for C_{phy} but remained close to the historical mean for Chl *a* (Figs. 3.26g,h).

Over the 28-year time series of spatially averaged monthly mean Chl *a* within the PSO, concentrations vary by 5.7% (0.008 mg m^{-3}, standard deviation) around an average of 0.136 mg m^{-3} (Fig. 3.27a). C_{phy} over the same 28-year period varies by 3.1% (0.68 mg m^{-3}) around an average of 21.8 mg m^{-3} (Fig. 3.27c). Chl *a* monthly anomalies within the PSO (Fig. 3.27b) vary by 4.5%

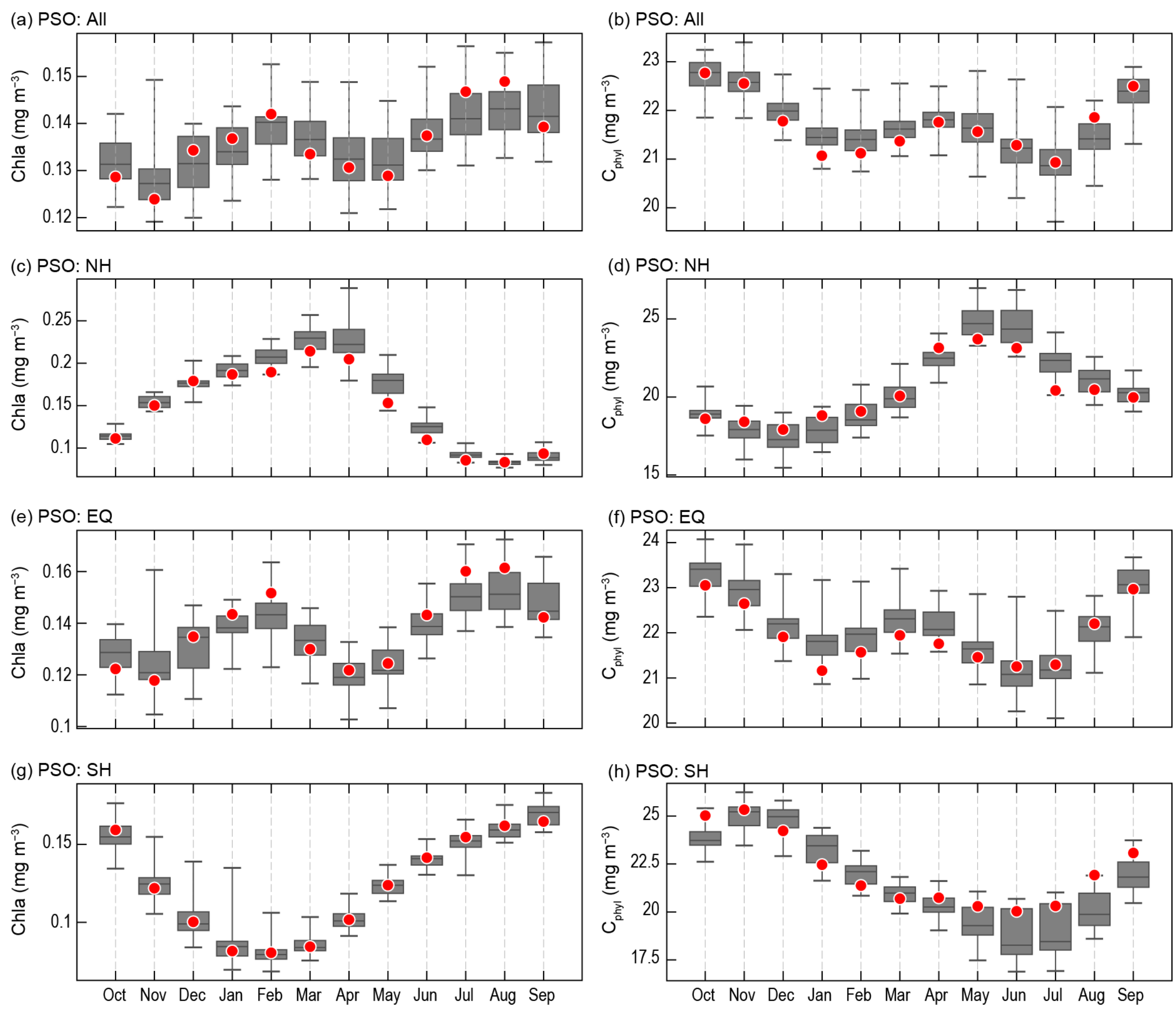

Fig. 3.26. Distribution of Oct 2024–Sep 2025 monthly means (red circles) for (a) VIIRS on NOAA-20 (VIIRS-N20) chlorophyll-*a* (Chl *a*) and (b) VIIRS-N20 phytoplankton carbon (C_{phy}) for the permanently stratified ocean (PSO) region (see Fig. 3.27), superimposed on the climatological values as derived from the combined time series of Sea-Viewing Wide Field-of-View Sensor (SeaWiFS), Moderate Resolution Imaging Spectroradiometer on Aqua (MODIS-A), and Visible Infrared Imaging Radiometer Suite on NOAA-20 (VIIRS-N20) over the period of Oct 1997–Sep 2024. Gray boxes show the interquartile range of the climatology, with a black line for the median value and whiskers extending to minimum and maximum values. Subsequent panels show latitudinally segregated subsets of the PSO for (c),(d) the Northern Hemisphere (above tropics)NH, (e),(f) tropical ±23.5° latitude subregion EQ, and (g),(h) Southern Hemipshere (below tropics). SH Units for (a), (c), (e), and (g) are Chl *a* (mg m^{-3}) and (b), (d), (f), and (h) are C_{phy} (mg m^{-3}).

(0.006 mg m^{-3}) over the multimission time series, with the largest interannual deviations generally associated with ENSO events (r = −0.38), as demonstrated by the correspondence of Chl *a* anomaly variations with the Multivariate ENSO Index (MEI; Wolter and Timlin 1998; presented in the inverse to illustrate the covariation). C_{phy} anomalies (Fig. 3.27d), which vary by 1.9% (0.42 mg m^{-3}), are less correlated with the MEI (r = −0.27) due to the inherent lag between environmental change, phytoplankton growth, and biomass accumulation. The monthly mean anomalies in 2025 for Chl *a* and C_{phy} within the PSO indicate modestly elevated concentrations in the early part of the analysis year and again in boreal summer, consistent with La Niña conditions that enhanced phytoplankton production.

Continuous ocean color monitoring enables us to track changes in the global distribution of marine phytoplankton, which play a critical role in driving biogeochemical processes, regulating the ocean's contribution to the global carbon cycle, and controlling marine ecosystems, food webs, and fisheries. By analyzing subtle variations in Chl *a* and C_{phy} distributions and seasonal cycles, we can distinguish between climate-driven changes in both phytoplankton biomass and shifts in their physiological state or community composition. The timing and distribution of phytoplankton biomass indicators for 2025 is consistent with the climatological record and the weak La Niña conditions that prevailed over much of the analysis year.

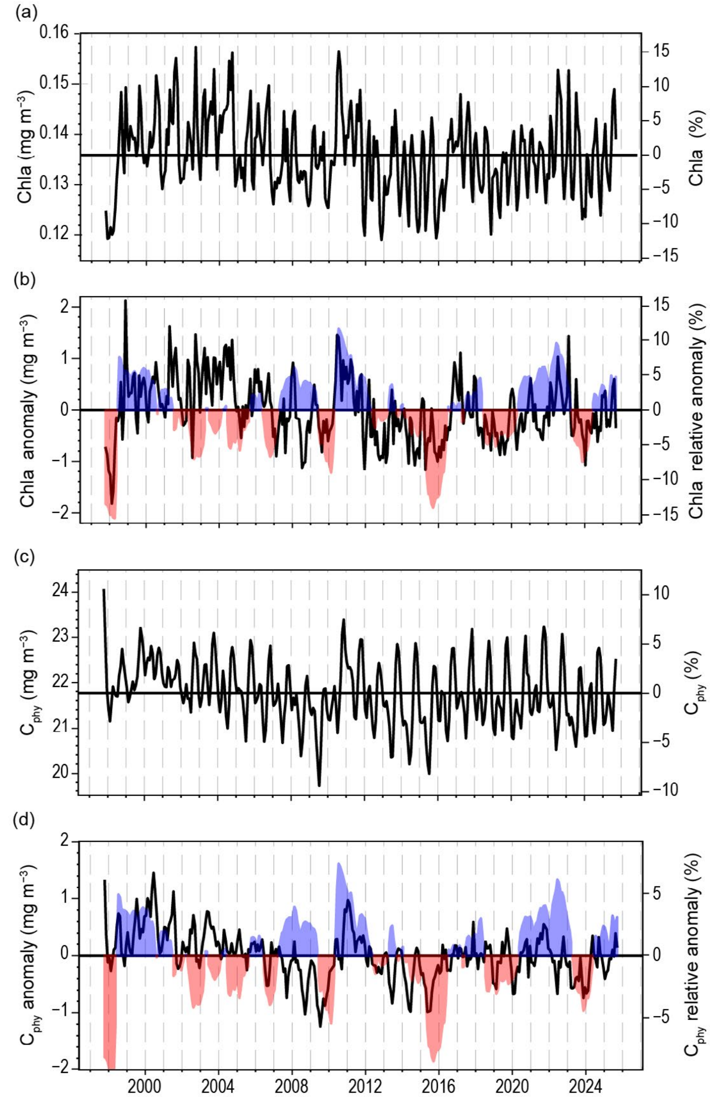

Fig. 3.27. Twenty-eight-year, multimission record of chlorophyll-*a* (Chl *a*; mg m^{-3}) and phytoplankton carbon (C_{phy}; mg m^{-3}) averaged over the permanently stratified ocean (PSO; Oct 1997 to Sep 2025). (a) Monthly Chl *a*, with the horizontal line indicating the multimission mean Chl *a* concentration for the entire PSO region. (b) Monthly Chl *a* anomalies after subtraction of the multimission climatological mean (Fig. 3.26a). (c) Monthly C_{phy}, with the horizontal line indicating the multimission mean C_{phy} concentration for the entire PSO region. (d) Monthly C_{phy} anomalies after subtraction of the multimission climatological mean (Fig. 3.26b). Shaded blue and red colors show the Multivariate El Niño–Southern Oscillation (ENSO) Index, inverted and scaled to match the range of the Chl *a* and C_{phy} anomalies, where blue indicates La Niña and red indicate El Niño conditions.

j. Global ocean carbon cycle

—A. Jersild, R. Wanninkhof, J. A. Triñanes, P. Landschützer, R. A. Feely, and B. R. Carter

1. INTRODUCTION

The oceans play a major role in the global carbon cycle by taking up a substantial fraction of the excess carbon dioxide (CO_2) that humans release into the atmosphere. As a consequence of these anthropogenic CO_2 (C_{ant}) emissions, the atmospheric CO_2 concentration has risen from pre-industrial levels of about 278 ppm (parts per million) to 425.7 ppm. Over the last decade the global ocean has continued to take up C_{ant} and is a major mediator of atmospheric CO_2 levels. Of the 11.2±0.9 Pg C yr^{-1} C_{ant} released during the period 2015–24, 3.2±0.4 Pg C yr^{-1} (29%) accumulated in the ocean, 2.4±0.8 Pg C yr^{-1} (21%) accumulated on land, and 5.6±0.02 Pg C yr^{-1} (50%) remained in the atmosphere (see Table 7 in Friedlingstein et al. 2026). This decadal C_{ant} uptake estimate by the ocean is a consensus view from a combination of measured ocean decadal CO_2 inventory changes, global ocean biogeochemical models, and global air–sea CO_2 flux estimates using data-based and machine learning systems, based on surface ocean fugacity of CO_2 (fCO_{2w})[1] measurements.

The ocean interior is more challenging to observe than the surface, leading to reduced temporal and spatial coverage than for surface ocean fCO_2. Machine-learning gap filling techniques are now being employed to provide increased resolution of interior C_{ant} estimates, with a 2025 mean inventory uptake of 3.7 Pg C yr^{-1} (Carter et al. 2025).

2. AIR–SEA CARBON DIOXIDE FLUXES

Ocean uptake of CO_2 is estimated from the net air–sea CO_2 flux derived from a bulk flux formula determined from the product of the difference of air and surface-seawater fCO_2 (ΔfCO_2) and gas transfer coefficients. Gas transfer is parameterized with wind, described in Wanninkhof (2014). This provides a net flux estimate. A river adjustment of 0.65 Pg C yr^{-1} is applied to uptake (Regnier et al. 2022), as recommended in the Global Carbon Budget (GCB) 2025. The data sources for fCO_{2w} are annual updates of observations from the Surface Ocean CO_2 Atlas (SOCAT) composed of moorings, autonomous surface vehicles, and ship-based observations (Bakker et al. 2016). The increased observations and improved mapping techniques, including machine learning methods summarized in Rödenbeck et al. (2015), provide global fCO_{2w} fields on a 1° × 1° grid at monthly time scales. For this report, we use a self-organizing maps feed-forward neural network (SOM-FNN) approach of Landschützer et al. (2013, 2014) and an extremely randomized trees (ET) machine learning technique (AOML-ET) described in Wanninkhof et al. (2025), both using SOCATv2025 for training. Predictor variables include: sea surface temperature (SST; Rayner et al. 2003); chlorophyll-*a* (Globcolour; Maritorena et al. 2010); mixed-layer depth (de Boyer Montégut et al. 2004 merged with Schmidtko et al. 2013), and salinity (Good et al. 2013). For atmospheric CO_2, the zonally resolved NOAA marine boundary layer atmospheric CO_2 product is used (Lan et al. 2023). Gas transfer coefficients are determined using European Centre for Medium-Range Weather Forecasts Reanalysis version 5 (ERA5) winds (Hersbach et al. 2018). The air–sea CO_2 flux for 2025 extrapolates the predictor variables for that year rather than having a year's latency.

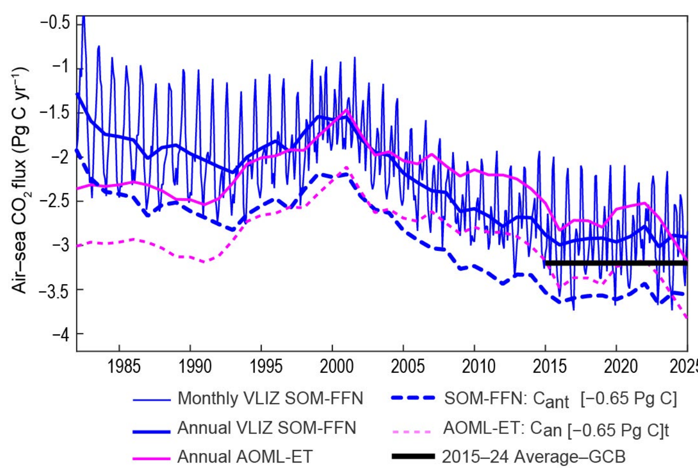

Fig. 3.28. Global annual (thick lines) and monthly (thin blue line) net air–sea carbon dioxide (CO_2) fluxes (Pg C yr^{-1}) for the period 1982–2025 using the Flanders Marine Institute (VLIZ) self-organizing maps feed-forward neural network (SOM-FFN) and the extremely randomized trees (ET) machine learning technique (AOML-ET) output. The annual anthropogenic CO_2 (C_{ant}) air–sea flux (dashed lines) includes the riverine adjustment of −0.65 Pg C. Negative values indicate CO_2 uptake by the ocean. The black line is the 2015–24 average from global carbon budget products (Friedlingstein et al. 2025).

The SOM-FNN and AOML-ET results (solid lines in Fig. 3.28) show a steady ocean CO_2 sink (S_{ocean}) from 1982 to the early 1990s, followed

[1] The fugacity is the partial pressure of CO_2 (pCO_2) corrected for non-ideality. They are numerically similar for surface waters with $fCO_2 \approx 0.994\ pCO_2$.

by a period of decreasing uptake to 2002. There is a strong increase in the ocean sink from 2002 onward that continues through 2016, after which the global uptake decreases until 2022. The 2025 S_{ocean} of 3.4 Pg C yr^{-1} (SOM-FFN) and 3.6 Pg C yr^{-1} (AOML-ET; dashed lines in Fig. 3.28) shows a ≈0.2 Pg C–0.4 Pg C increase in uptake above the 2015–24 GCB average of 3.2±0.4 Pg C yr^{-1} when the riverine adjustment is included. The amplitude of seasonal variability is ≈1.6 Pg C with a minimum uptake in June–September.

The annual average flux map for 2025 (Fig. 3.29a) shows the characteristic pattern of high effluxes (ocean-to-air CO_2 fluxes) in equatorial-tropical, coastal upwelling, and open-ocean upwelling regions. Coastal upwelling regions include those in the Arabian Sea and off the west coasts of North America, South America, and West Africa. The western Bering Sea continues to be a strong CO_2 source, a juxtaposition to the strong sink in surrounding regions. This regional source is hypothesized to result from a local outcropping of shallow isopycnals with high CO_2 values, but this has not been independently verified. Cumulatively, the regions of effluxes are substantial CO_2 sources to the atmosphere (≈1 Pg C). The primary CO_2 uptake regions are in the subtropical and subpolar regions. The largest sinks are poleward of the sub-tropical fronts. Generally, SST influences solubility (positive SST anomalies decrease solubility, increasing fCO_{2w}). However, in regions with high fCO_{2w} due to upwelling, warmer SST stemming from decreased upwelling of the cold CO_2-rich water leads to lower fCO_{2w}.

In the Northern Hemisphere, the North Atlantic is a large sink, while the North Pacific is punctuated by a substantial source of CO_2 in the western subpolar Pacific and the central Bering Sea (Fig. 3.29a). The Northern Hemisphere sinks are, in part, due to the position of the western boundary currents whose cooling waters, transported poleward, increase solubility and contribute to CO_2 uptake at high latitudes. The Gulf Stream/North Atlantic Drift in the Atlantic extends farther north than the Kuroshio in the Pacific, extending the region of a strong sink in the North Atlantic.

The ocean carbon uptake anomalies (Fig. 3.29c) in 2025 relative to the 1990–2020 average, adjusted for the 30-year trend, demonstrate the return to neutral El Niño–Southern Oscillation (ENSO) conditions over much of the summer, with some evidence of the weak La Niña returning in autumn 2025. The Southern Ocean (≈45°S–60°S) continues to show reduced uptake when compared to the 30-year trend, although it should be noted the regional average is still overall an ocean sink. This reduction of uptake of nearly 50% smaller

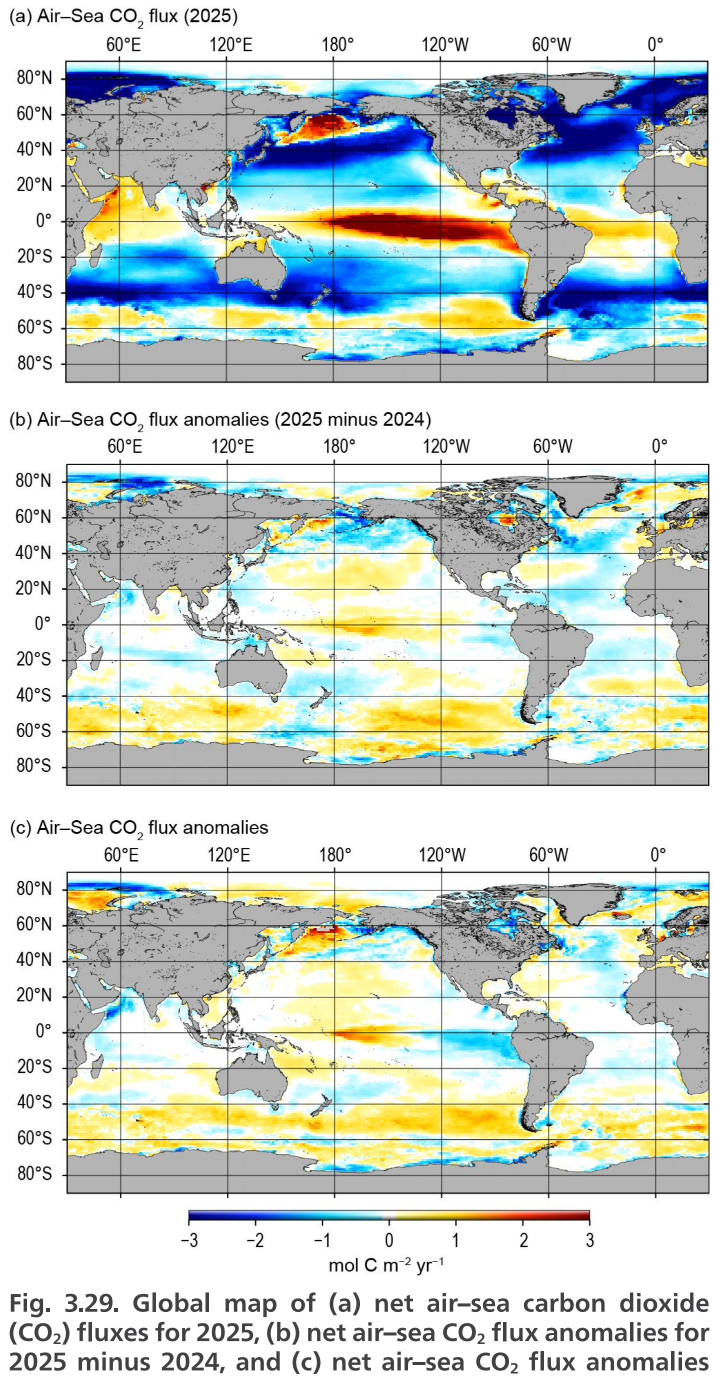

Fig. 3.29. Global map of (a) net air–sea carbon dioxide (CO_2) fluxes for 2025, (b) net air–sea CO_2 flux anomalies for 2025 minus 2024, and (c) net air–sea CO_2 flux anomalies for 2025 relative to 1990–2020 average values, adjusted for the 30-year trend using the Flanders Marine Institute (VLIZ) self-organizing maps feed-forward neural network (SOM-FNN) approach. Units are all mol C m^2 yr^{-1}. Ocean CO_2 uptake regions are shown in blue. For reference, a global ocean CO_2 uptake of 2.8 Pg C yr^{-1} equals a flux density of −0.65 mol C m^2 yr^{-1}.

than previous estimates is likely due to a combination of temporal variation, methodological improvements, and estimate uncertainty stemming from data sparsity in the region (Hauck et al. 2023).

The spatial differences in CO_2 fluxes between 2025 and 2024 (Fig. 3.29b) shows an increased influx (blue shading) in the Atlantic and polar regions, potentially a recovery of the anomalous reduced uptake observed in 2023/24 (Müller et al. 2025). In the Southern Ocean, we observe an increased efflux. This difference can mainly be attributed to shifting levels of observations in the Southern Ocean in the SOCAT dataset (Fay et al. 2025). The machine-learning methods and use of predictor values to complete the time series can be sensitive to data availability, and low-sampled regions can be highly responsive to individual observations (Jersild and Landschützer 2024; Hauck et al. 2023).

3. OCEAN INTERIOR INVENTORY ESTIMATES

The ocean inventory of dissolved inorganic carbon (DIC) varies over time due to surface CO_2 fluxes, interior ocean cycling of organic matter, riverine inputs, and sedimentary exchanges. Interior ocean observations are more expensive and challenging to obtain than surface observations, so their coverage tends to be more limited across time and space. For this reason, interior ocean DIC observations are primarily used in decadal retrospective analyses that quantify the accumulation of C_{ant} throughout the ocean.

As with $f\mathrm{CO}_{2w}$, machine learning gap-filling techniques are now being used to map the available measurements onto data products that have better spatial and temporal resolution (e.g., Keppler et al. 2023). For example, Fig. 3.30 reflects machine learning estimates of DIC (Carter et al. 2021, centered on the year 2002) and C_{ant} (Carter et al. 2025) derived from the temperature and salinity climatology of Roemmich and Gilson (2009). These estimates collectively allow the total ocean inventory ($C_{inventory}$) estimates and their increases (Fig. 3.30, attributable primarily to S_{ocean}) to be separated into natural variations (ΔC_{nat}) and anthropogenic accumulation (ΔC_{ant}).

Meaningful interannual variability can be seen in the annually averaged rate of $C_{inventory}$ accumulation (Fig. 3.30). This variability is also attributable primarily to C_{nat} variability. The C_{ant} changes are mostly steady from year to year, and the variations generally oppose the much larger variations in the C_{nat}. This anticorrelation can result when increases in ocean overturning generate anomalous loss of deep carbon accumulated from organic matter respiration and anomalous uptake of C_{ant} with ventilation of older waters (DeVries et al. 2017). Surface ocean heat content variations also play a role; anomalously warm waters hold less DIC and more C_{ant} than anomalously cool waters when in air–sea gas exchange equilibrium with the atmosphere.

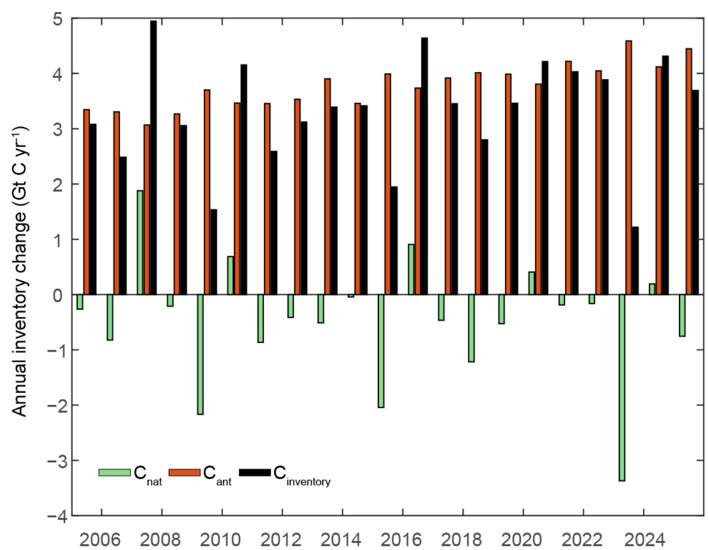

Fig. 3.30. Annual average accumulation rates (Gt C yr^{-1}) for the ocean inventories of total dissolved inorganic carbon ($C_{inventory}$; black), the portion attributable to anthropogenic carbon emissions (C_{ant}; red), and the portion attributable to natural processes (C_{nat}; green), which is estimated by residual.

The mean inventory increase rate over the 2015–24 period of 3.4 Pg C yr^{-1} is comparable to the 3.2±0.4 Pg C yr^{-1} estimate from air–sea fluxes. Both ways of estimating S_{ocean} imply larger increases in 2025: 3.7 Pg C yr^{-1} for the inventory estimate and 3.4 Pg C–3.6 Pg C yr^{-1} for the air–sea CO_2 flux estimate. Two differences in the estimates, that are well within their uncertainties, can be attributed to the fact that the interannual variations in the inventory estimates are greater and the inventory estimates do not show the recent (post 2016) relaxation of ocean CO_2 uptake.

Ocean interior inventory mapping can take advantage of regular updates to the underlying climatologies to provide timely and detailed information about ocean carbon inventory variations. However, as of yet, these estimates solely provide projections of expected patterns based on DIC measurements that predate 2024, and rely on the Argo-array-dominated temperature and salinity patterns from ~2004 onward to generate the estimates for the most recent years. Furthermore, the methodological uncertainties for this approach have yet to be quantified.

k. Global ocean dissolved oxygen

—J. D. Sharp, Z. Wang, T. Ito, S. Minobe, L. Cheng, J. Du, H. Garcia, C. J. Roach, B. Lu, Y. Xin, M. Han, Y. Zhou, and G. G. Navarra

Dissolved oxygen (O_2) is vital for aerobic marine organisms and plays a major role in shaping species distributions (Deutsch et al. 2024; Stramma et al. 2012), modulating elemental cycles (Gruber 2008), and regulating the production of natural greenhouse gases such as nitrous oxide and methane (Bianchi et al. 2012). A major consequence of climate warming is the widespread loss of dissolved O_2 from seawater (Gruber 2011; Keeling et al. 2010; Levin 2018; Long et al. 2016; Oschlies et al. 2017). Unlike the well-mixed atmosphere, oxygen is unevenly distributed in the ocean, and some regions contain levels too low to support most marine organisms (Breitburg et al. 2018). This variability arises because 1) oxygen supply from photosynthesis and air–sea exchange is limited to surface waters, 2) biological respiration, whereby heterotrophic organisms use oxygen to extract energy from organic carbon (OC), depletes oxygen in a spatiotemporally uneven way depending on the rate of OC supply, heterotrophic community composition, and additional environmental factors, and 3) ocean circulation and mixing redistribute oxygen throughout the ocean interior. Dissolved oxygen in seawater is declining; estimates have suggested the global ocean lost 0.5%–3.3% of its O_2 inventory (surface to 1000-m depth) from 1970 to 2010 (Bindoff et al. 2019; Helm et al. 2011; Ito et al. 2017; Schmidtko et al. 2017).

The ocean's oxygen inventory, the total amount of oxygen in the ocean, is difficult to track, as observations are scattered and the quality of O_2 observations is generally lower than that of temperature and salinity. Further, there has been an evolution over time in the data sources that contribute to the observational record for dissolved oxygen in the open ocean, with Winkler titrations from bottle samples being most prevalent from the 1960s through the 1980s, electrochemical sensors on shipboard CTDs contributing heavily to the record from the 1990s through the 2010s, and optical sensors on profiling floats becoming the dominant data source in the 2010s through the present (Fig. 3.31). This diversity of data sources means that discrepancies among measurement types and their spatial distribution must be carefully considered, especially when trying to extract a trend from the observational record using aggregated data from several sources. We analyze time-varying, three-dimensional, mapped fields of ocean oxygen from nine different approaches to evaluate the changing ocean oxygen inventory over the last 60 years and anomalies in 2025 relative to a 1990–2020 baseline.

The O_2 fields considered in this analysis include results from five statistical interpolation (SI) methods—objective analysis using weighted-averaging interpolation (NCEI; Garcia et al. 2024a), ensemble optimal interpolation (IAP; Cheng et al. 2020; Cheng ad Zhu 2016; Gouretski et al. 2024), Gaussian optimal interpolation (GT-OI; Ito 2022), data-interpolating variational analysis (UTAS; Roach and Bindof 2023), and geostatistical regression (SJTU-GR; Zhou et al. 2022)—and four machine-learning (ML) methods—Gaussian mixture models and shallow neural networks (GOBAI; Sharp et al. 2023), neural networks and random forest regressions (GT-ML; Ito et al. 2024), hybrid graph learning (Jingwei; Lu et al. 2024), and Bayesian ensemble machine learning (SJTU-HZ; Han et al. 2025).

The maps considered here may not correspond directly with the data products described in the references listed but are built using the methods described in those references. Eight are constructed using data extracted from the World Ocean Database 2023 (WOD23) updated through 2025 (Garcia et al. 2024a; Mishonov et al. 2024), and one (IAP) uses data from the IAP database (Gouretski et al. 2024). Because eight out of nine results use WOD23 with the same quality control, comparisons among the ensemble differ primarily in mapping methodology, not in their primary data sources and quality-control methods. However, previous work has demonstrated that mapping methods have a greater effect on variability among mapped climatological (annual mean) products than the small variations in the primary data sources and the quality-control methods (Ito et al. 2025), so we believe our results represent a robust ensemble. The SI maps use data binned into $1° \times 1°$ annual bins and the ML maps use individual profile data to train models that are applied to temperature and salinity data mapped onto $1° \times 1°$ monthly bins. Three of the ML maps (GOBAI, GT-ML, and Jingwei) use temperature and salinity data from the EN4.2.2 dataset (Good et al. 2013) and SJTU-HZ uses the ORAS5 dataset (Copernicus Climate Change Service 2021).

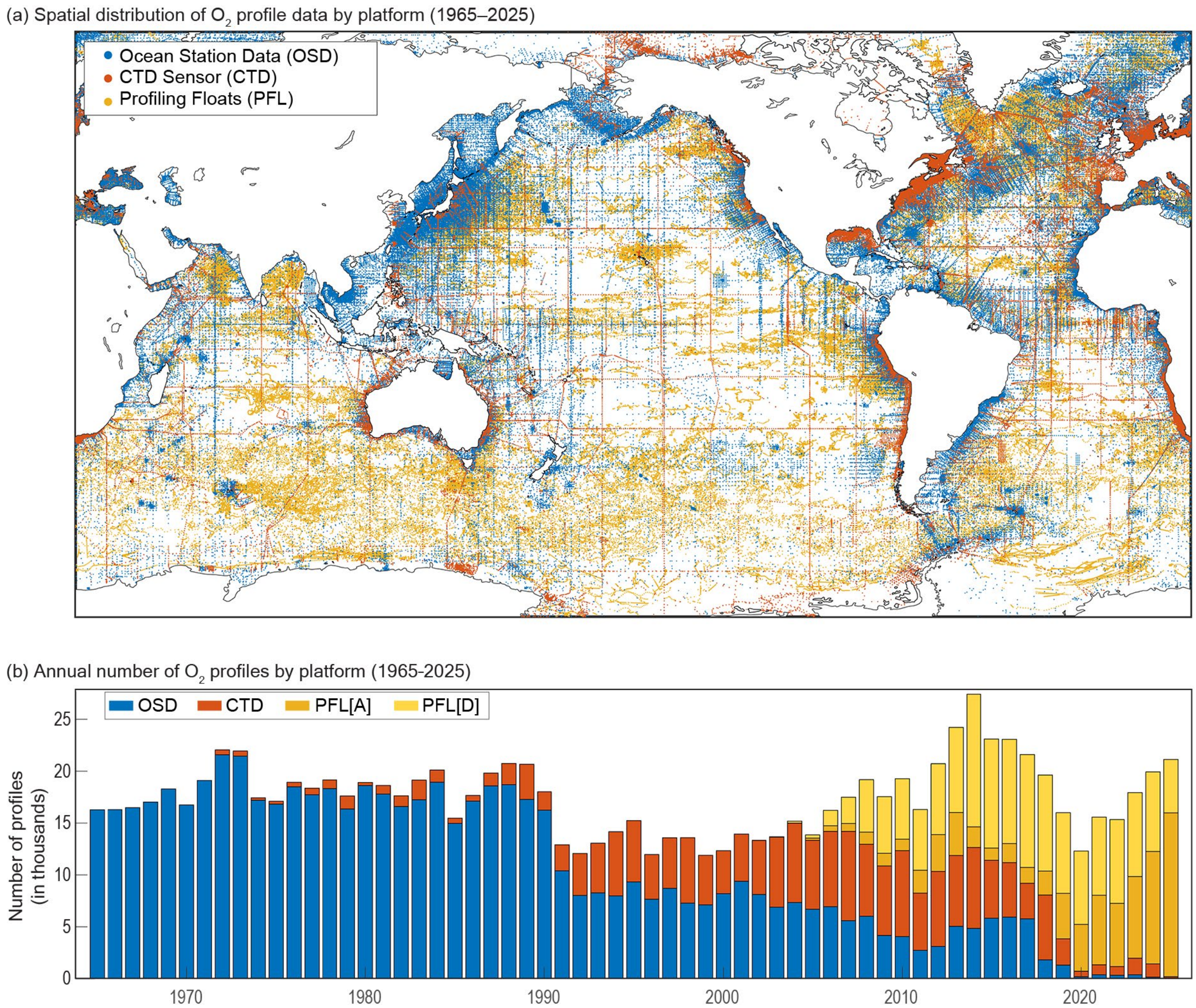

Fig. 3.31. (a) Spatial distribution and (b) annual number of profiles containing dissolved oxygen (O_2) observations contributed by different platforms to the dataset used to create the dissolved oxygen maps. Measurements were extracted from the World Ocean Database 2023, updated through 2025. Data from bottle measurements at ocean stations (OSD), conductivity-temperature-depth profiles (CTD), and profiling floats (PFL) are included, as they are the three most prevalent oxygen data sources. In (b), profiling float data are separated into data with real-time adjustments (PFL[A]) and data with delayed-mode quality-control (PFL[D]).

The ensemble long-term mean oxygen inventories show the effects of high O_2 solubility in cold, high-latitude waters compared to low O_2 solubility in warm, tropical waters in the 0-m–50-m depth layer (Fig. 3.32a). From 50 m to 1000 m, accumulated respiration and weak ventilation result in extremely low oxygen inventories in the subarctic North Pacific, eastern tropical Pacific, North Indian, and eastern tropical Atlantic (Fig. 3.32b). Conversely, strong ventilation forms highly oxygenated mode and intermediate waters in the North Atlantic and Southern Oceans, which extend equatorward.

Dissolved oxygen content in the ocean has generally decreased over at least the last 60 years (Fig. 3.32e). Negative trends in the 0-m–50-m depth layer (Fig. 3.32c) reveal the widespread influence of rising sea surface temperature (section 3b), which decreases O_2 solubility and increases upper ocean stratification (Oschlies et al. 2018). Negative trends from 50 m to 1000 m (Fig. 3.32d) reflect deoxygenation driven by additional factors, including reduced ventilation, changes in interior ocean circulation, and enhanced biological respiration. Bindoff et al. (2019) indicated that the North Pacific and Southern Oceans have seen the largest changes in oxygen inventory over the past few decades, which is supported by our results (Fig. 3.32d). Long et al. (2016) highlight the impact of reduced ventilation driving strong deoxygenation trends in the North Pacific, agreeing with our results as well as an analysis of oxygen trends at Ocean Station Papa (Cummins and Ross 2020) and recent global-scale work by Ito et al. (2026). The small area exhibiting an O_2 increase in the North Atlantic (Fig. 3.32d) is likely related to variability in the ventilation of Labrador Sea Water (Rhein et al. 2017) and in the Atlantic meridional overturning circulation (section 3h). A weak O_2 increase in the western subtropical South Pacific (Fig. 3.32d) aligns with a feature pointed out by Ito et al. (2026) and corresponds with a cooling signal pointed out by Garcia-Soto et al. (2021).

Volume-integrated O_2 inventories from 0 m–1800 m (Fig. 3.32e) show an average trend from 1965 to 2025 of −0.45±0.10% decade^{-1} (mean±sample standard deviation across nine maps) relative to a climatological mean inventory (1965–2025) of 91.2±0.2 Pmol O_2 (in a volume equal to 565.96×10^6 km^3). All the maps show relatively weak trends until about the mid-1980s, after which stronger O_2 loss continues through 2025. This behavior was first reported by Garcia et al. (2005), who noted an O_2 increase from the 1950s to mid-1980s, followed by O_2 loss in the upper 100 m. This pattern has since been confirmed by more recent studies that include deeper levels (e.g., Ito et al. 2017). The ML maps tend to display greater interannual variability (IAV = 0.28±0.12%) and stronger trends (−0.52±0.08% decade^{-1}) compared to the SI maps (IAV = 0.24±0.07%; trend = −0.39±0.08 % decade^{-1}). IAV is calculated as the standard deviation of de-trended annual mean inventory values for each product, with the trend removed using a linear least-squares fit. For both IAV and trends, the mean (μ) and sample standard deviation (±σ) are reported across the SI maps (n = 5) and the ML maps (n = 4).

The differences in multidecadal trends and interannual variability between the two subsets of O_2 maps (SI and ML) could be partially explained by fundamental differences between the

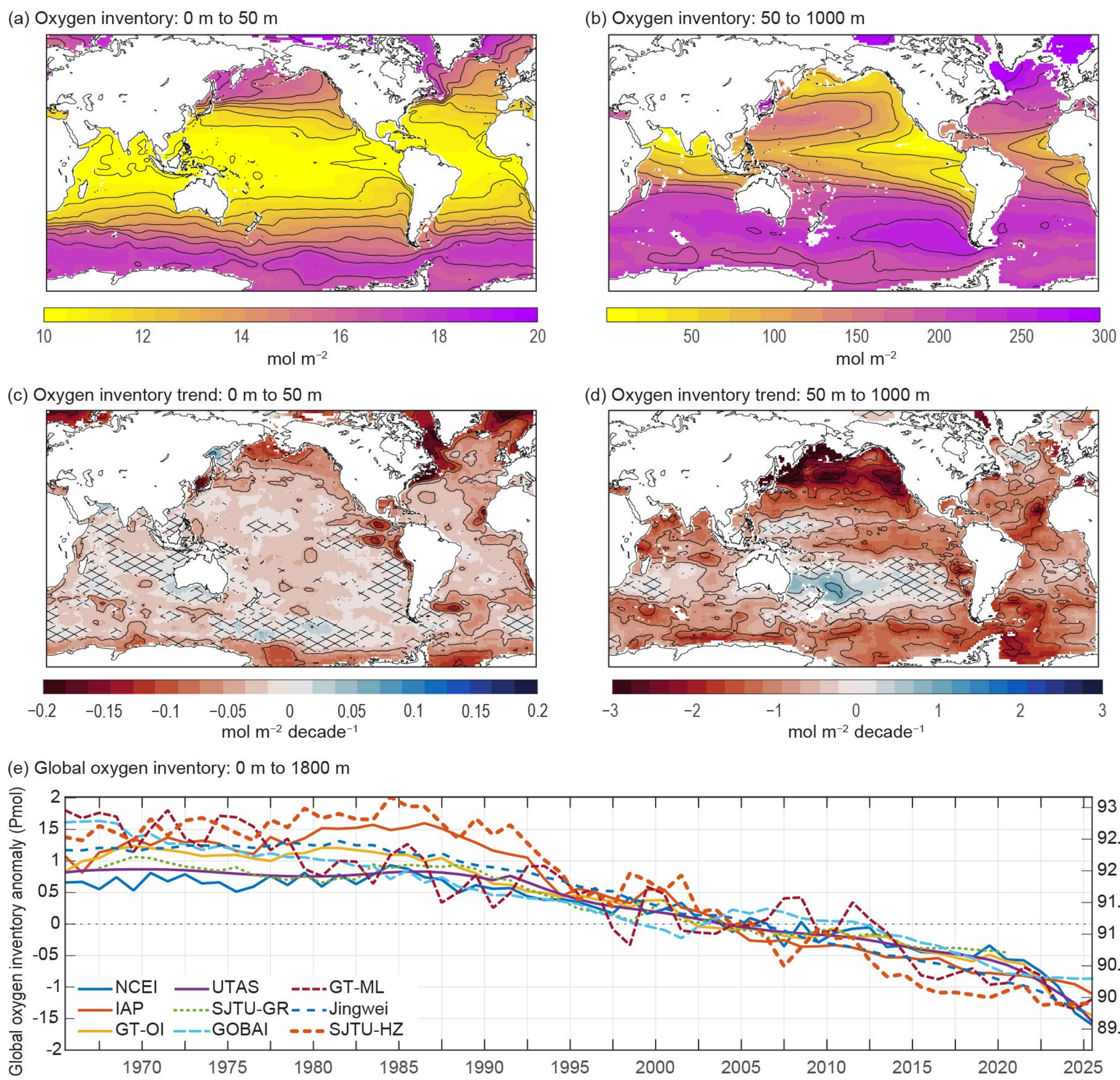

Fig. 3.32. (a),(b) Ensemble mean dissolved oxygen (O_2) inventories (mol m^{-2}) and (c),(d) trends (1965–2025; mol m^{-2} decade^{-1}) from (a),(c) 0 m to 50 m and (b),(d) 50 m to 1000 m across all nine mapping approaches. (e) Global O_2 inventory anomalies (Pmol; 1990–2020 baseline) integrated from 0 m to 1800 m for each individual approach. Areas in (c),(d) where fewer than seven out of the nine products agree on the sign of the trend are cross-hatched.

approaches. SI methods tend to relax toward the long-term mean in the absence of data, potentially contributing to weaker trends near the beginning of the time series (Fig. 3.32e) where the dominant bottle data are less widespread (Fig. 3.31b). ML approaches are inextricably tied to their predictors (e.g., gridded temperature and salinity) and have more variation in how they are implemented, potentially contributing to greater disagreement among these approaches (Fig. 3.32e). Another important consideration is the shift in observational sources toward profiling floats over time (Fig. 3.31b) and the correction applied to compensate for an apparent, global-mean negative bias (about –1.69 μmol kg^{-1}) in the profiling float dataset relative to colocated bottle and CTD measurements (Gouretski et al. 2024; Wang et al. 2025). Although the negative bias is adjusted for in the O_2 dataset, steep declines in some of the SI maps in recent years when float data are particularly dominant suggest that the +1.69 μmol kg^{-1} adjustment to the float dataset may be insufficient, or that the spatial variation in the float O_2 bias requires a more complex adjustment (Bittig and Körtzinger 2017; Maurer et al. 2021).

O_2 anomalies in 2025 (relative to 1990–2020) were broadly negative (Figs. 3.33a,b), consistent with the long-term deoxygenation trend (Figs. 3.33e,f). Strong negative anomalies from 0 m–50 m in the midlatitude western Pacific corresponded with strong positive SST, heat content, and sea level anomalies in the same region (sections 3b,c,f, respectively). Similarly, negative near-surface

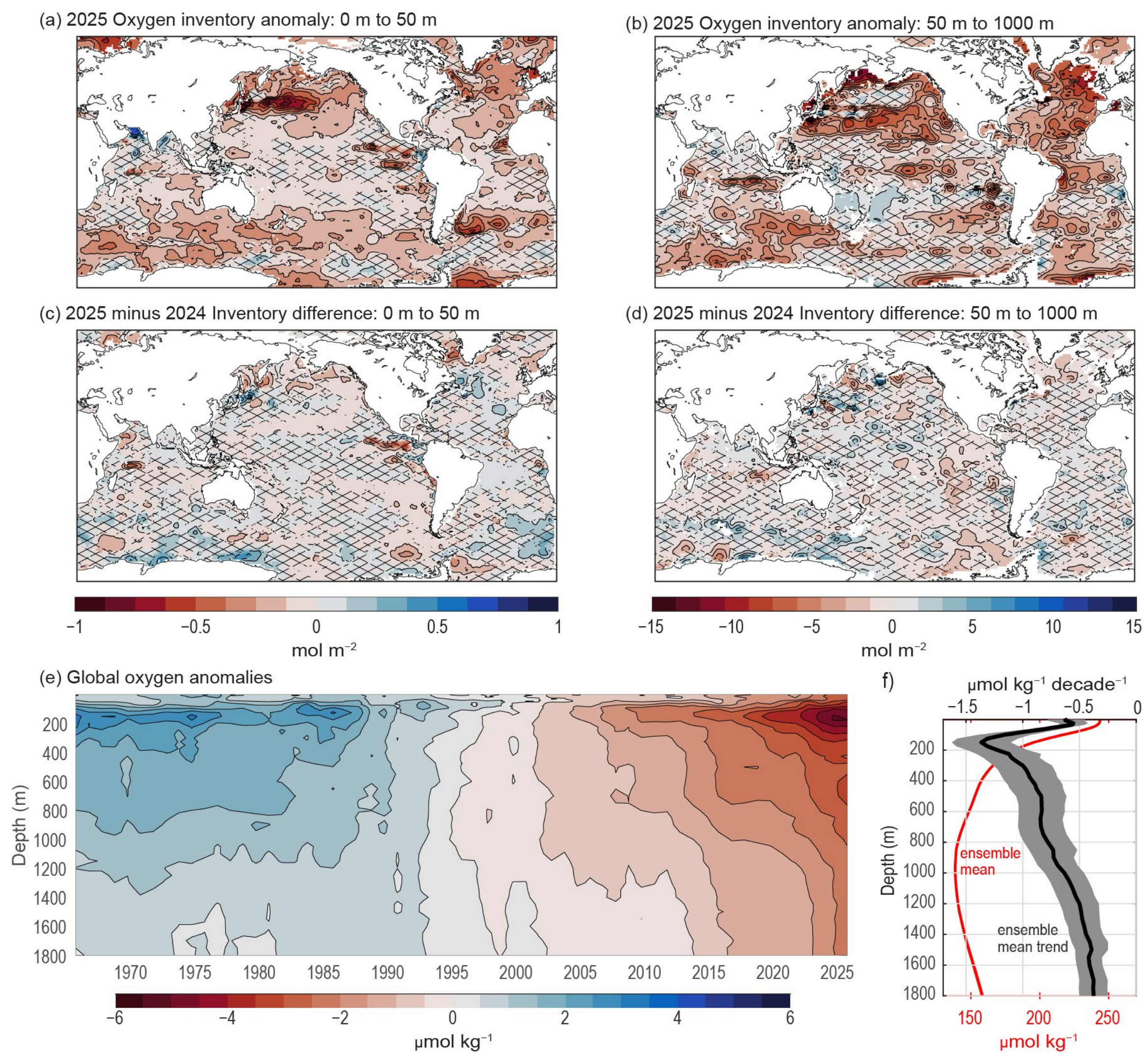

Fig. 3.33. Ensemble mean dissolved oxygen (O_2) inventory anomalies (mol m^{-2}) in 2025 compared to the 1990–2020 baseline from (a) 0 m to 50 m and (b) 50 m to 1000 m; the difference between the ensemble mean inventory in 2025 versus in 2024 (mol m^{-2}) from (c) 0 m to 50 m and (d) 50 m to 1000 m; (e) the global ensemble mean [O_2] anomaly as a function of depth over time (μmol kg^{-1}) ; and (f) the ensemble average profile of [O_2; μmol kg^{-1}; red] and decadal [O_2; μmol kg^{-1} $decade^{-1}$; black] trends (units for the x-axes are listed in the labels within the plot area). Each ensemble average map (a)–(d) is computed across eight of the nine mapping approaches (SJTU-GR excluded). Areas in the maps where fewer than six out of the eight products agree on the sign of the anomalies are cross-hatched.

anomalies are observed in the Southern Ocean from 45°S to 55°S as well as the Weddell and Ross Seas. On the contrary, near-zero O_2 anomalies from 0 m–50 m in much of the equatorial Pacific were associated with negative SST, heat content, and sea level anomalies, consistent with a weak intermittent La Niña in 2025 (see section 4b for details). From 50 m–1000 m, strong negative O_2 anomalies occurred in the North Pacific and North Atlantic, consistent with positive heat content anomalies in these regions (Fig. 3.4). Apparent positive O_2 anomalies in the subpolar North Pacific (Fig. 3.33b) surrounded by negative anomalies in both subtropical waters to the south and polar waters to the north is consistent with recent findings of a decadal northward displacement of the subtropical and subpolar gyre boundaries caused by the northward contraction of the Aleutian Low (e.g., Minobe 2025), which can be driven by the superposition of internal variability and anthropogenic trends (Abe and Minobe 2023; Long et al. 2016). A moderate positive anomaly is also observed in the western subtropical South Pacific.

Differences between the 2025 and 2024 anomalies were mostly small (Figs. 3.33c,d). The oxygen levels in the eastern equatorial Pacific are known to covary with the thermocline shoaling in the region with implications to the regional ecosystem and air–sea oxygen exchange (Eddebbar et al. 2017; Leung et al. 2019; Parouffe et al. 2025). The tropical Pacific Ocean is influenced by the interannual climate variability associated with ENSO, and the lower O_2 in the near-surface eastern equatorial Pacific in 2025 (Fig. 3.33c) may have been connected to the superposition of weak La Niña conditions with the long-term trends.

Appendix 1: Acronyms

ACC	Antarctic Circumpolar Current
ADCPs	acoustic doppler current profilers
AOML	Atlantic Oceanographic and Meteorological Laboratory
BASS	Blended Analysis of Surface Salinity
b_{bp}	particle backscattering coefficient
C_{ant}	anthropogenic CO_2
CAS	Chinese Academy of Sciences
CDS	Climate Data Store
Chl *a*	chlorophyll-*a*
CIMAR	Cooperative Institute for Marine and Atmospheric Research
Cinventory	changes in the total ocean inventory
CO_2	carbon dioxide
C_{phy}	phytoplankton carbon
CSIRO	Commonwealth Scientific and Industrial Research Organisation
CTD	conductivity temperature and depth
DCENT	Dynamically Consistent ENsemble of Temperature
DIC	dissolved inorganic carbon
DOISST	Daily OISST
EBAF	Energy Balanced and Filled
ENSO	El Niño–Southern Oscillation
fCO_{2w}	surface ocean fugacity of CO_2
FLASHFlux	Fast Longwave And Shortwave Radiative Fluxes
GCB	Global Carbon Budget
GIA	glacial isostatic adjustment
GMSL	global mean sea level
GPCP	Global Precipitation Climatology Project
GRACE	Gravity Recovery and Climate Experiment
GRACE-FO	GRACE Follow-On
HadSST	Hadley Centre Sea Surface Temperature
IAP	Institute of Atmospheric Physics
IIT	Indian Institutes of Technology
IOD	Indian Ocean dipole
ITCZ	Intertropical Convergence Zone
JPL	Jet Propulsion Laboratory
LH	latent heat flux
LW	longwave radiation
MBT	mechanical bathythermograph
MCS	marine cold spell
MHT	meridional heat transport
MHW	marine heatwave
ML	machine learning
MOC	meridional overturning circulation
MODIS-A	Moderate Resolution Imaging Spectroradiometer on Aqua
MOVE	Meridional Overturning Variability Experiment
MRI	Meteorological Research Institute
NDBC	National Data Buoy Center
NH	Northern Hemisphere
NOC	National Oceanography Centre
OC	organic carbon

OHCA	ocean heat content anomaly
ORAS5	Ocean ReAnalysis System 5
OSNAP	Overturning in the Subpolar North Atlantic Program
pCO_2	partial pressure of CO_2
PDO	Pacific Decadal Oscillation
PMEL	Pacific Marine Environmental Laboratory
PSO	permanently stratified ocean
PSS-78	Practical Salinity Scale-78
Q_{net}	net surface heat flux
RAPID	Rapid Climate Change
RFROM	Random Forest Regression Ocean Maps
SAMBA	South Atlantic MOC Basin-wide Array
SAR	synthetic aperture radar
SH	Southern Hemisphere
SI	statistical interpolation
SIO	Scripps Institution of Oceanography
SMAP	Soil Moisture Active Passive
SMOS	Soil Moisture and Ocean Salinity
SOCAT	Surface Ocean CO_2 Atlas
S_{ocean}	steady ocean CO_2 sink
SOM-FNN	self-organizing maps feed-forward neural network
SPCZ	South Pacific Convergence Zone
SSH	sea surface height
SSS	sea surface salinity
SST	sea surface temperature
SSTA	sea surface temperature anomaly
SSTAs	sea surface temperature anomalies
SSTs	sea surface temperatures
SW	shortwave radiation
SWOT	Surface Water and Ocean Topography
TAO	Tropical Atmosphere Ocean
TOA	Top-Of-Atmosphere
TPOS	Tropical Pacific Observing System
VIIRS-N20	Visible Infrared Imaging Radiometer Suite on NOAA20
VLIZ	Flanders Marine Institute
W_{EK}	Ekman vertical velocity
WHOI	Woods Hole Oceanographic Institution
XBT	Expendable Bathythermograph
ΔC_{ant}	anthropogenic accumulation
ΔC_{nat}	natural variations

Appendix 2: Dataset Tables

Section 3b Sea surface temperature

Sub-section	General Variable or Phenomenon	Specific Dataset or Variable	Source
3b	Sea Surface Temperature	Dynamically Consistent ENsemble of Temperature (DCENT) Version 1.1	https://doi.org/10.7910/DVN/ROG38Q
3b	Sea Surface Temperature	ERSSTv5	https://doi.org/10.7289/V5T72FNM
3b	Sea Surface Temperature	Hadley Centre Sea Surface Temperature Dataset (HadSST) Version 4	https://www.metoffice.gov.uk/hadobs/hadsst4/
3b	Sea Surface Temperature	NOAA Daily Optimum Interpolated Temperature (DOISST) Version 2.1	https://doi.org/10.25921/RE9P-PT57

Section 3c Ocean temperature and heat content

Sub-section	General Variable or Phenomenon	Specific Dataset or Variable	Source
3c	Ocean Heat Content	Argo	http://doi.org/10.17882/42182#125185
3c	Ocean Heat Content	Argo Monthly Climatology	https://sio-argo.ucsd.edu/RG_Climatology.html
3c	Ocean Heat Content	CLIVAR and Carbon Hydrographic Data Office	https://cchdo.ucsd.edu/
3c	Ocean Heat Content	Institute of Atmospheric Physics (IAP)/Chinese Academy of Sciences (CAS)	http://www.ocean.iap.ac.cn/pages/dataService/dataService.html
3c	Ocean Heat Content	Meteorological Research Institute (MRI)/Japan Meteorological Agency (JMA)	https://www.data.jma.go.jp/kaiyou/english/ohc/ohc_global_en.html
3c	Ocean Heat Content	NCEI	https://www.ncei.noaa.gov/access/global-ocean-heat-content/
3c	Ocean Heat Content	Pacific Marine Environmental Laboratory (PMEL)/Jet Propulsion Laboratory (JPL)/ Cooperative Institute for Marine and Atmospheric Research (CIMAR)	https://www.pmel.noaa.gov/rfrom/
3c	Ocean Heat Content	Random Forest Regression Ocean Maps (RFROM) Version 2.2	https://www.pmel.noaa.gov/rfrom/
3c	Ocean Heat Content	UK Met Office EN4.2.2	https://www.metoffice.gov.uk/hadobs/en4/download-en4-2-2.html

Sub-section	General Variable or Phenomenon	Specific Dataset or Variable	Source
3c	Ocean Heat Content	University of Colorado/ Carnegie Mellon University (CU/CMU)	https://doi.org/10.5281/zenodo.18187866
3c	Ocean Temperature	World Ocean Database	https://www.ncei.noaa.gov/products/world-ocean-database

Section 3d Salinity

Sub-section	General Variable or Phenomenon	Specific Dataset or Variable	Source
3d2	Ocean Salinity	Aquarius Version 3.0	http://podaac.jpl.nasa.gov/aquarius
3d2	Ocean Salinity	Argo	https://doi.org/10.17882/42182
3d2	Ocean Salinity	Blended Analysis for Surface Salinity	ftp://ftp.cpc.ncep.noaa.gov/precip/BASS
3d	Ocean Salinity	NCEI Salinity Anomaly	https://www.ncei.noaa.gov/access/global-ocean-heat-content/
3d2	Ocean Salinity	Soil Moisture Active Passive (SMAP)	https://podaac.jpl.nasa.gov/SMAP
3d2	Ocean Salinity	Soil Moisture Ocean Salinity (SMOS)	https://earth.esa.int/eogateway/missions/smos
3d	Ocean Salinity	World Ocean Atlas 2023	https://www.ncei.noaa.gov/products/world-ocean-atlas
3d	Ocean Salinity	World Ocean Database	https://www.ncei.noaa.gov/products/world-ocean-database

Section 3e Global ocean heat, freshwater, and momentum flux

Sub-section	General Variable or Phenomenon	Specific Dataset or Variable	Source
3e1	Air–Sea Fluxes (Shortwave/Longwave Radiation)	CERES FlashFlux	https://asdc.larc.nasa.gov/project/CERES/FLASH_SSF_NOAA20-FM6-VIIRS_Version1B
3e1	Air–Sea Fluxes (Shortwave/Longwave Radiation)	Clouds and the Earth's Radiant Energy System (CERES) Energy Balanced and Filled (EBAF) Version 4.2	https://asdc.larc.nasa.gov/project/CERES/CERES_EBAF_Edition4.2
3e1	Air–Sea Fluxes (Shortwave/Longwave Radiation)	ERA5	https://www.ecmwf.int/en/forecasts/dataset/ecmwf-reanalysis-v5
3e2	Precipitation	GPCPv2.3	https://psl.noaa.gov/data/gridded/data.gpcp.html
3e2	Evaporation	OAFLux2	https://oaflux.whoi.edu/

Sub-section	General Variable or Phenomenon	Specific Dataset or Variable	Source
3e3	Wind Stress	OAFlux2	https://oaflux.whoi.edu/
3e1	Air–Sea Fluxes (Latent Heat/Sensible Heat)	Objectively Analyzed Air–Sea Heat Fluxes (OAFlux2)	https://oaflux.whoi.edu/

Section 3f Sea Level variability and change

Sub-section	General Variable or Phenomenon	Specific Dataset or Variable	Source
3f	Sea Level / Sea Surface Height	Argo	https://sio-argo.ucsd.edu/RG_Climatology.html
3f	Ocean Heat Content	Argo Monthly Climatology	https://sio-argo.ucsd.edu/RG_Climatology.html
3f	Sea Level / Sea Surface Height	Copernicus Climate Change Service (C3S) Altimetry Data	Delayed mode: https://data.marine.copernicus.eu/product/SEALEVEL_GLO_PHY_L4_MY_008_047; Near real time: https://data.marine.copernicus.eu/product/SEALEVEL_GLO_PHY_L4_NRT_008_046
3f	Ocean Mass	Gravity Recovery and Climate Experiment (GRACE)/Grace Follow-On (GRACE-FO)	https://grace.jpl.nasa.gov/data/get-data
3f	Sea Level / Sea Surface Height	NASA Making Earth Science Data Records for Use in Research Environments (MEaSURES)	https://podaac.jpl.nasa.gov/dataset/SEA_SURFACE_HEIGHT_ALT_GRIDS_L4_2SATS_5DAY_6THDEG_V_JPL2205
3f	Sea Level / Sea Surface Height	Tide Gauge	http://uhslc.soest.Hawaiʻi.edu/

Section 3g Surface currents

Sub-section	General Variable or Phenomenon	Specific Dataset or Variable	Source
3g	Surface Velocity	Drifter/Altimetry/Wind Synthesis Product	1993-2024: https://www.aoml.noaa.gov/ftp/pub/phod/lumpkin/decomp/; 2025: https://www.aoml.noaa.gov/ftp/pub/phod/matthieu.lehenaff/decomp/
3g	Ocean Currents	Global Tropical Moored Buoy Array (GTMBA)	https://www.pmel.noaa.gov/gtmba/

Section 3h Meridional overturning circulation and heat transport			
Sub-section	**General Variable or Phenomenon**	**Specific Dataset or Variable**	**Source**
3h	Ocean Currents	Atlantic Ship of Opportunity Expendable Bathythermograph (XBT)	https://www.aoml.noaa.gov/phod/goos/xbt_network/; https://www.aoml.noaa.gov/phod/hdenxbt/index.php
3h	Ocean Currents	Argo	https://doi.org/10.17882/42182#116315; https://www.aoml.noaa.gov/argo/#argodata
3h	Ocean Currents	ERA5	https://cds.climate.copernicus.eu/datasets/reanalysis-era5-single-levels-monthly-means?tab=overview
3h	Ocean Currents	Florida Current Transport	https://www.aoml.noaa.gov/phod/floridacurrent/data_access.php
3h	Ocean Currents	Global Temperature and Salinity Profile Program (GTSPP)	https://www.ncei.noaa.gov/products/global-temperature-and-salinity-profile-programme
3h	Ocean Currents	Meridional Overturning Variability Experiment (MOVE) array	https://mooring.ucsd.edu/move/
3h	Ocean Currents	Overturning in the Subpolar North Atlantic Program (OSNAP)	https://www.o-snap.org/
3h	Ocean Currents	RAPID–Meridional Overturning Circulation and Heat-flux Array–Western Boundary Time Series (RAPID)	https://rapid.ac.uk/rapidmoc/
3h	Ocean Currents	Sea Level Anomalies	https://doi.org/10.48670/moi-00149; https://doi.org/10.48670/moi-00148
3h	Ocean Currents	Sea Surface Height (Delayed-mode)	https://data.marine.copernicus.eu/product/SEALEVEL_GLO_PHY_L4_MY_008_047/services
3h	Ocean Currents	Sea Surface Height (Near-real time)	https://data.marine.copernicus.eu/product/SEALEVEL_GLO_PHY_L4_NRT_008_046/services
3h	Ocean Currents	South Atlantic MOC Basin-wide Array (SAMBA)	https://www.aoml.noaa.gov/sam/

Section 3i Global ocean phytoplankton			
Sub-section	**General Variable or Phenomenon**	**Specific Dataset or Variable**	**Source**
3i	Daytime Sea Surface Temperature	Moderate Resolution Imaging Spectroradiometer on *Aqua* (MODIS-A) Version R2022.0	https://oceancolor.gsfc.nasa.gov/data/reprocessing/r2022/aqua/
3i	Phytoplankton Chlorophyll Particle Backscattering Coefficient	MODIS-A	https://modis.gsfc.nasa.gov/data/dataprod/chlor_a.php
3i	Phytoplankton Chlorophyll Particle Backscattering Coefficient	Sea-viewing Wide Field-of-view Sensor (SeaWiFS) Version R2022.0	https://oceancolor.gsfc.nasa.gov/data/reprocessing/r2022/seawifs/
3i	Phytoplankton Chlorophyll Particle Backscattering Coefficient	Visible Infrared Imaging Radiometer Suite (VIIRS)-NOAA20 Version R2022.0	https://data.nasa.gov/dataset/noaa-20-viirs-global-mapped-chlorophyll-chl-nrt-data-version-r2022-0

Section 3j Global ocean carbon cycle			
Sub-section	**General Variable or Phenomenon**	**Specific Dataset or Variable**	**Source**
3j3	Ocean Salinity	Argo Monthly Climatology	https://sio-argo.ucsd.edu/RG_Climatology.html
3j3	Ocean Temperature	Argo Monthly Climatology	https://sio-argo.ucsd.edu/RG_Climatology.html
3j2	Mixed Layer Depth	de Boyer Montegut (2004; 2023 update); Monthly Isopycnal & Mixed-layer Ocean Climatology (MMOC)	https://www.seanoe.org/data/00806/91774/; https://www.pmel.noaa.gov/mimoc/
3j2	Winds [Near] Surface	ERA5	https://www.ecmwf.int/en/forecasts/dataset/ecmwf-reanalysis-v5
3j2	Chlorophyll	GlobColour	https://hermes.acri.fr/index.php
3j2	Ocean Salinity	Hadley Center EN4	https://www.metoffice.gov.uk/hadobs/en4/
3j2	Atmospheric Carbon Dioxide	NOAA Greenhouse Gas Marine Boundary Layer Reference	https://gml.noaa.gov/ccgg/mbl/mbl.html
3j2	Sea Surface Temperature	NOAA OISST Version 2.1	https://www.ncei.noaa.gov/products/optimum-interpolation-sst
3j2	Ocean Carbon	Surface Ocean CO_2 Atlas (SOCAT) Version 2024	https://socat.info/index.php/version-2025/

3k Global ocean dissolved oxygen			
Sub-section	**General Variable or Phenomenon**	**Specific Dataset or Variable**	**Source**
3k	Ocean Temperature / Salinity / Oxygen	AP Global Ocean Oxygen	https://doi.org/10.12157/IOCAS.20231208.001
3k	Ocean Temperature / Salinity	EN4 Objective Analyses	https://www.metoffice.gov.uk/hadobs/en4/
3k	Ocean Oxygen	GODIP-DO Mapped Oxygen	https://doi.org/10.5281/zenodo.19892752
3k	Ocean Temperature / Salinity / Oxygen	World Ocean Database 2023	https://doi.org/10.25923/z885-h264

References

Abe, Y., and S. Minobe, 2023: Comparison of ocean deoxygenation between CMIP models and an observational dataset in the North Pacific from 1958 to 2005. *Front. Mar. Sci.*, **10**, 1161451, https://doi.org/10.3389/fmars.2023.1161451.

Adler, R. F., and Coauthors, 2018: The Global Precipitation Climatology Project (GPCP) monthly analysis (new version 2.3) and a review of 2017 global precipitation. *Atmosphere*, **9**, 138, https://doi.org/10.3390/atmos9040138.

Arcodia, M. C., E. A. Barnes, P. J. Durack, P. W. Keys, and J. Rocha, 2025: Sea surface salinity provides subseasonal predictability for forecasts of opportunity of U.S. summertime precipitation. *J. Geophys. Res. Atmos.*, **130**, e2024JD042402, https://doi.org/10.1029/2024JD042402.

Bai, Y., Y. Zhang, X. Zhang, and X. Li, 2025: A machine learning-based ocean current velocity inversion model using Sentinel-1 OCN observations. *IEEE J. Sel. Top. Appl. Earth Obs. Remote Sens.*, **18**, 9622–9635, https://doi.org/10.1109/JSTARS.2025.3554229.

Bakker, D. C. E., and Coauthors, 2016: A multi-decade record of high-quality fCO_2 data in version 3 of the Surface Ocean CO_2 Atlas (SOCAT). *Earth Syst. Sci. Data*, **8**, 383–413, https://doi.org/10.5194/essd-8-383-2016.

——, and Coauthors, 2025: Surface Ocean CO2 Atlas Database version 2025 (SOCATv2025) (NCEI Accession 0304549). NOAA NCEI, accessed 10 July 2025, https://doi.org/10.25921/648f-fv35.

Behrenfeld, M. J., and Coauthors, 2006: Climate-driven trends in contemporary ocean productivity. *Nature*, **444**, 752–755, https://doi.org/10.1038/nature05317.

——, and Coauthors, 2016: Reevaluating ocean warming impacts on global phytoplankton. *Nat. Climate Change*, **6**, 323–330, https://doi.org/10.1038/nclimate2838

Bianchi, D., J. P. Dunne, J. L. Sarmiento, and E. D. Galbraith, 2012: Data-based estimates of suboxia, denitrification, and N_2O production in the ocean and their sensitivities to dissolved O_2. *Global Biogeochem. Cycles*, **26**, GB2009, https://doi.org/10.1029/2011GB004209.

Bindoff, N. L., and Coauthors, 2019: Changing ocean, marine ecosystems, and dependent communities. *Ocean and Cryosphere in a Changing Climate*, H.-O. Pörtner et al., Eds., IPCC, 447–588.

Bittig, H. C., and A. Körtzinger, 2017: Technical note: Update on response times, in-air measurements, and in situ drift for oxygen optodes on profiling platforms. *Ocean Sci.*, **13** (1), 1–11, https://doi.org/10.5194/os-13-1-2017.

Breitburg, D., and Coauthors, 2018: Declining oxygen in the global ocean and coastal waters. *Science*, **359**, eaam7240, https://doi.org/10.1126/science.aam7240.

Broecker, W. S., 1991: The great ocean conveyor. *Oceanography*, **4**, 79–89, https://doi.org/10.5670/oceanog.1991.07.

Caldwell, P. C., M. A. Merrifield, and P. R. Thompson, 2015: Sea level measured by tide gauges from global oceans—The Joint Archive for Sea Level holdings (NCEI Accession 0019568), version 5.5. NOAA NCEI, accessed 9 February 2026, https://doi.org/10.7289/V5V40S7W.

Caron, L., and E. R. Ivins, 2020: A baseline Antarctic GIA correction for space gravimetry. *Earth Planet. Sci. Lett.*, **531**, 115957, https://doi.org/10.1016/j.epsl.2019.115957.

Carter, B. R., J. Schwinger, R. Sonnerup, A. J. Fassbender, J. D. Sharp, L. M. Dias, and D. E. Sandborn, 2025: Tracer-based Rapid Anthropogenic Carbon Estimation (TRACE). *Earth Syst. Sci. Data*, **17**, 3073–3088, https://doi.org/10.5194/essd-17-3073-2025.

——, and Coauthors, 2021: New and updated global empirical seawater property estimation routines. *Limnol. Oceanogr. Methods*, **19**, 785–809, https://doi.org/10.1002/lom3.10461.

Cetinić, I., M. J. Perry, N. T. Briggs, E. Kallin, E. A. D'Asaro, and C. M. Lee, 2012: Particulate organic carbon and inherent optical properties during 2008 North Atlantic bloom experiment. *J. Geophys. Res.*, **117**, C06028, https://doi.org/10.1029/2011JC007771.

Chambers, D. P., A. Cazenave, N. Champollion, H. Dieng, W. Llovel, R. Forsberg, K. von Schuckmann, and Y. Wada, 2017: Evaluation of the global mean sea level budget between 1993 and 2014. *Surv. Geophys.*, **38**, 309–327, https://doi.org/10.1007/s10712-016-9381-3.

Chan, D., and Coauthors, 2026: DCENT-I: A globally infilled extension of the Dynamically Consistent Ensemble of Temperature dataset. *Geosci. Data J.*, **13**, e70054, https://doi.org/10.1002/gdj3.70054.

Cheng, L., and J. Zhu, 2016: Benefits of CMIP5 multimodel ensemble in reconstructing historical ocean subsurface temperature variations. *J. Climate*, **29**, 5393–5416, https://doi.org/10.1175/JCLI-D-15-0730.1.

——, ——, R. Cowley, T. Boyer, and S. Wijffels, 2014: Time, probe type, and temperature variable bias corrections to historical expendable bathythermograph observations. *J. Atmos. Oceanic Technol.*, **31**, 1793–1825, https://doi.org/10.1175/JTECH-D-13-00197.1.

——, and Coauthors, 2020: Improved estimates of changes in upper ocean salinity and the hydrological cycle. *J. Climate*, **33**, 10 357–10 381, https://doi.org/10.1175/JCLI-D-20-0366.1.

Ciani, D., C. Fanelli, and B. Buongiorno Nardelli, 2025: Estimating ocean currents from the joint reconstruction of absolute dynamic topography and sea surface temperature through deep learning algorithms. *Ocean Sci.*, **21**, 199–216, https://doi.org/10.5194/os-21-199-2025.

Copernicus Climate Change Service, 2021: ORAS5 global ocean reanalysis monthly data from 1958 to present. ECMWF, accessed 1 July 2025, https://doi.org/10.24381/CDS.67E8EEB7.

Cummins, P. F., and T. Ross, 2020: Secular trends in water properties at Station P in the northeast Pacific: An updated analysis. *Prog. Oceanogr.*, **186**, 102329, https://doi.org/10.1016/j.pocean.2020.102329.

de Boyer Montégut, C., G. Madec, A. S. Fischer, A. Lazar, and D. Iudicone, 2004: Mixed layer depth over the global ocean: An examination of profile data and a profile-based climatology. *J. Geophys. Res.*, **109**, C12003, https://doi.org/10.1029/2004JC002378.

Deser, C., M. A. Alexander, S.-P. Xie, and A. S. Phillips, 2010: Sea surface temperature variability: Patterns and mechanisms. *Ann. Rev. Mar. Sci.*, **2**, 115–143, https://doi.org/10.1146/annurev-marine-120408-151453.

Deutsch, C., J. L. Penn, and N. Lucey, 2024: Climate, oxygen, and the future of marine biodiversity. *Ann. Rev. Mar. Sci.*, **16**, 217–245, https://doi.org/10.1146/annurev-marine-040323-095231.

DeVries, T., M. Holzer, and F. Primeau, 2017: Recent increase in oceanic carbon uptake driven by weaker upper-ocean overturning. *Nature*, **542**, 215–218, https://doi.org/10.1038/nature21068.

Domingues, C. M., J. A. Church, N. J. White, P. J. Gleckler, S. E. Wijffels, P. M. Barker, and J. R. Dunn, 2008: Improved estimates of upper-ocean warming and multi-decadal sea-level rise. *Nature*, **453**, 1090–1093. https://doi.org/10.1038/nature07080.

Dong, S., G. Goni, and F. Bringas, 2015: Temporal variability of the South Atlantic meridional overturning circulation between 20°S and 35°S. *Geophys. Res. Lett.*, **42**, 7655–7662, https://doi.org/10.1002/2015GL065603.

——, ——, R. Domingues, F. Bringas, M. Goes, J. Christophersen, and M. Baringer, 2021: Synergy of in situ and satellite ocean observations in determining meridional heat transport in the Atlantic Ocean. *J. Geophys. Res. Oceans*, **126**, e2020JC017073, https://doi.org/10.1029/2020JC017073.

Donohoe, A., R. Fajber, T. Cox, K. C. Armour, D. S. Battisti, and G. H. Roe, 2024: Model biases in the atmosphere?ocean partitioning of poleward heat transport are persistent across three CMIP generations. *Geophys. Res. Lett.*, **51**, e2023GL106639, https://doi.org/10.1029/2023GL106639.

Durack, P. J., and S. E. Wijffels, 2010: Fifty-year trends in global ocean salinities and their relationship to broad-scale warming. *J. Climate*, **23**, 4342–4362, https://doi.org/10.1175/2010JCLI3377.1.

——, ——, and R. J. Matear, 2012: Ocean salinities reveal strong global water cycle intensification during 1950 to 2000. *Science*, **336**, 455–458, https://doi.org/10.1126/science.1212222.

Eddebbar, Y. A., M. C. Long, L. Resplandy, C. Rödenbeck, K. B. Rodgers, M. Manizza, and R. F. Keeling, 2017: Impacts of ENSO on air-sea oxygen exchange: Observations and mechanisms. *Global Biogeochem. Cycles*, **31**, 901–921, https://doi.org/10.1002/2017GB005630.

Fairall, C. W., E. F. Bradley, J. E. Hare, A. A. Grachev, and J. B. Edson, 2003: Bulk parameterization of air–sea fluxes: Updates and verification for the COARE algorithm. *J. Climate*, **16**, 571–591, https://doi.org/10.1175/1520-0442(2003)016<0571:BPOASF>2.0.CO;2.

Fasullo, J. T., C. Boening, F. W. Landerer, and R. S. Nerem, 2013: Australia's unique influence on global sea level in 2010–2011. *Geophys. Res. Lett.*, **40**, 4368–4373, https://doi.org/10.1002/grl.50834.

——, R. Nerem, and B. Hamlington, 2016: Is the detection of accelerated sea level rise imminent?. *Sci. Rep.*, **6**, 31245, https://doi.org/10.1038/srep31245.

Fay, A. R., T. H. Heimdal, V. Acquaviva, A. P. Shaum, and G. A. McKinley, 2025: Sensitivity of ocean carbon sink estimates to rare observations. *Geophys. Res. Lett.*, **52**, e2025GL117961, https://doi.org/10.1029/2025GL117961.

Field, C. B., M. J. Behrenfeld, J. T. Randerson, and P. Falkowski, 1998: Primary production of the biosphere: Integrating terrestrial and oceanic components. *Science*, **281**, 237–240, https://doi.org/10.1126/science.281.5374.237.

Fofonoff, N. P., and E. L. Lewis, 1979: A practical salinity scale. *J. Oceanogr. Soc. Japan*, **35**, 63–64, https://doi.org/10.1007/BF02108283.

Font, J., and Coauthors, 2013: SMOS first data analysis for sea surface salinity determination. *Int. J. Remote Sens.*, **34**, 3654–3670, https://doi.org/10.1080/01431161.2012.716541.

Fore, A. G., S. H. Yueh, W. Q. Tang, B. W. Stiles, and A. K. Hayashi, 2016: Combined active/passive retrievals of ocean vector wind and sea surface salinity with SMAP. IEEE Trans. *Geosci. Remote Sens.*, **54**, 7396–7404, https://doi.org/10.1109/TGRS.2016.2601486.

Forster, P. M., and Coauthors, 2025: Indicators of global climate change 2024: Annual update of key indicators of the state of the climate system and human influence. *Earth Syst. Sci. Data*, **17**, 2641–2680, https://doi.org/10.5194/essd-17-2641-2025.

Friedlingstein, P., and Coauthors, 2026: Global carbon budget 2025. *Earth Syst. Sci. Data*, **18**, 3211–3288, https://doi.org/10.5194/essd-2025-659.

Fu, Y., and Coauthors, 2025: Characterizing the interannual variability of North Atlantic subpolar overturning. *Geophys. Res. Lett.*, **52**, e2025GL114672, https://doi.org/10.1029/2025GL114672.

Garcia, H. E., T. P. Boyer, S. Levitus, R. A. Locarnini, and J. Antonov, 2005: On the variability of dissolved oxygen and apparent oxygen utilization content for the upper world ocean: 1955 to 1998. *Geophys. Res. Lett.*, **32**, L09604, https://doi.org/10.1029/2004GL022286.

——., and Coauthors, 2024a: *Dissolved Oxygen, Apparent Oxygen Utilization, and Dissolved Oxygen Saturation*. Vol. 3, *World Ocean Atlas 2023*, NOAA Atlas NESDIS 91, 110 pp., https://doi.org/10.25923/RB67-NS53.

——, and Coauthors, 2024b: *User's Manual*. World Ocean Database 2023, A. V. Mishonov, Tech. Ed., NOAA Atlas NESDIS 98, 134 pp., https://doi.org/10.25923/j8gq-ee82.

Garcia, P., and Coauthors, 2025: ORCAst: Operational high-resolution current forecasts. *Artif. Intell. Earth Syst.*, **4**, e250002, https://doi.org/10.1175/AIES-D-25-0002.1.

Garcia-Soto, C., and Coauthors, 2021: An overview of ocean climate change indicators: Sea surface temperature, ocean heat content, ocean pH, dissolved oxygen concentration, Arctic sea ice extent, thickness and volume, sea level and strength of the AMOC (Atlantic meridional overturning circulation). *Front. Mar. Sci.*, **8**, 642372, https://doi.org/10.3389/fmars.2021.642372.

Ge, L., G. Chen, G. Wang, C. Cao, X. Chen, and B. Huang, 2025: Multiscale dynamics-informed deep learning reconstruction of global ocean offshore near-surface current. *GISci. Remote Sens.*, **62**, 2596455, https://doi.org/10.1080/15481603.2025.2596455.

Geider, R. J., H. L. MacIntyre, and T. M. Kana, 1997: Dynamic model of phytoplankton growth and acclimation: Responses of the balanced growth rate and the chlorophyll a: Carbon ratio to light, nutrient-limitation and temperature. *Mar. Ecol. Prog. Ser.*, **148**, 187–200, https://doi.org/10.3354/meps148187.

Good, S. A., M. J. Martin, and N. A. Rayner, 2013: EN4: Quality controlled ocean temperature and salinity profiles and monthly objective analyses with uncertainty estimates. *J. Geophys. Res. Oceans*, **118**, 6704–6716, https://doi.org/10.1002/2013JC009067.

Gordon, A. L., 1986: Interocean exchange of thermocline water. *J. Geophys. Res.*, **91**, 5037–5046, https://doi.org/10.1029/JC091iC04p05037.

Gouretski, V., and L. Cheng, 2020: Correction for systematic errors in the global dataset of temperature profiles from mechanical bathythermographs. *J. Atmos. Oceanic Technol.*, **37**, 841–855, https://doi.org/10.1175/JTECH-D-19-0205.1.

——, ——, J. Du, X. Xing, F. Chai, and Z. Tan, 2024: A consistent ocean oxygen profile dataset with new quality control and bias assessment. *Earth Syst. Sci. Data*, **16**, 5503–5530, https://doi.org/10.5194/essd-16-5503-2024.

Graff, J. R., T. K. Westberry, A. J. Milligan, M. B. Brown, G. Dall'Olmo, V. V Dongen-Vogels, K. M. Reifel, and M. J. Behrenfeld, 2015: Analytical phytoplankton carbon measurements spanning diverse ecosystems. *Deep-Sea Res. I*, **102**, 16–25, https://doi.org/10.1016/j.dsr.2015.04.006.

——, ——, ——, ——, ——, ——, ——, and ——, 2016: Photoacclimation of natural phytoplankton communities. *Mar. Ecol. Prog. Ser.*, **542**, 51–62, https://doi.org/10.3354/meps11539.

Gruber, N., 2008: The marine nitrogen cycle: Overview and challenges. *Nitrogen in the Marine Environment*, Vol. 2, Academic Press, 1–50.
——, 2011: Warming up, turning sour, losing breath: Ocean biogeochemistry under global change. *Philos. Trans. Roy. Soc.*, **A369**, 1980–1996, https://doi.org/10.1098/rsta.2011.0003.
Hamlington, B. D., and Coauthors, 2024: The rate of global sea level rise doubled during the past three decades. *Commun. Earth Environ.*, **5**, 601, https://doi.org/10.1038/s43247-024-01761-5.
Han, M., X. Xing, and Y. Zhou, 2025: Global Monthly Ocean Dissolved Oxygen (1960–2023) reconstructed to 5,902 m with BLENDR, a Bayesian-optimized ensemble learning framework. *Earth Syst. Sci. Data*, **18**, 3757–3777, https://doi.org/10.5194/essd-2025-781.
Hauck, J., and Coauthors, 2023: The Southern Ocean carbon cycle 1985–2018: Mean, seasonal cycle, trends, and storage. *Global Biogeochem. Cycles*, **37**, e2023GB007848, https://doi.org/10.1029/2023GB007848.
Held, I. M., and B. J. Soden, 2006: Robust responses of the hydrological cycle to global warming. *J. Climate*, **19**, 5686–5699, https://doi.org/10.1175/JCLI3990.1.
Helm, K. P., N. L. Bindoff, and J. A. Church, 2011: Observed decreases in oxygen content of the global ocean. *Geophys. Res. Lett.*, **38**, L23602, https://doi.org/10.1029/2011GL049513.
Henley, B. J., J. Gergis, D. J. Karoly, S. B. Power, J. Kennedy, and C. K. Folland, 2015: A tripole index for the interdecadal Pacific oscillation. *Climate Dyn.*, **45**, 3077–3090, https://doi.org/10.1007/s00382-015-2525-1.
Hersbach, H., and Coauthors, 2018: ERA5 hourly data on single levels from 1959 to present. Copernicus Climate Change Service (C3S) Climate Data Store (CDS), accessed 2 January 2024, https://doi.org/10.24381/cds.adbb2d47.
——, and Coauthors, 2020: The ERA5 global reanalysis. *Quart. J. Royal Meteor. Soc.*, **146**, 1999–2049. https://doi.org/10.1002/qj.3803.
Hobbs, W. R., and J. K. Willis, 2012: Midlatitude North Atlantic heat transport: A time series based on satellite and drifter data. *J. Geophys. Res.*, **117**, C01008, https://doi.org/10.1029/2011JC007039.
Hobday, A. J., and Coauthors, 2016: A hierarchical approach to defining marine heatwaves. *Prog. Oceanogr.*, **141**, 227–238, https://doi.org/10.1016/j.pocean.2015.12.014.
——, and Coauthors, 2018: Categorizing and naming marine heatwaves. *Oceanography*, **31** (2), 162–173, https://doi.org/10.5670/oceanog.2018.205.
Hu, C., Z. Lee, and B. Franz, 2012: Chlorophyll *a* algorithms for oligotrophic oceans: A novel approach based on three-band reflectance difference. *J. Geophys. Res.*, **117**, C01011, https://doi.org/10.1029/2011JC007395.
——, L. Feng, Z. Lee, B. A. Franz, S. W. Bailey, P. J. Werdell, and C. W. Proctor, 2019: Improving satellite global chlorophyll *a* data products through algorithm refinement and data recovery. *J. Geophys. Res. Oceans*, **124**, 1524–1543, https://doi.org/10.1029/2019JC014941.
Hu, Z.-Z., M. J. McPhaden, B. Huang, J. Zhu, and Y. Liu, 2024: Accelerated warming in the North Pacific since 2013. *Nat. Climate Change*, **14**, 929–931, https://doi.org/10.1038/s41558-024-02088-x.
Huang, B., and Coauthors, 2015: Extended reconstructed sea surface temperature version 4 (ERSST.v4). Part I: Upgrades and intercomparisons. *J. Climate*, **28**, 911–930, https://doi.org/10.1175/JCLI-D-14-00006.1.
——, and Coauthors, 2017: Extended reconstructed sea surface temperature, version 5 (ERSSTv5): Upgrades, validations, and intercomparisons. *J. Climate*, **30**, 8179–8205, https://doi.org/10.1175/JCLI-D-16-0836.1.
——, and Coauthors, 2020: Uncertainty estimates for sea surface temperature and land surface air temperature in NOAAGlobalTemp version 5. *J. Climate*, **33**, 1351–1379, https://doi.org/10.1175/JCLI-D-19-0395.1.
——, C. Liu, V. Banzon, E. Freeman, G. Graham, B. Hankins, T. Smith, and H.-M. Zhang, 2021: Improvements of the Daily Optimum Interpolation Sea Surface Temperature (DOISST) version 2.1. *J. Climate*, **34**, 2923–2939, https://doi.org/10.1175/JCLI-D-20-0166.1.
Hughes, T. P., and Coauthors, 2017: Global warming and recurrent mass bleaching of corals. *Nature*, **543**, 373–377, https://doi.org/10.1038/nature21707.
Ishii, M., Y. Fukuda, S. Hirahara, S. Yasui, T. Suzuki, and K. Sato, 2017: Accuracy of global upper ocean heat content estimation expected from present observational data sets. *SOLA*, **13**, 163–167, https://doi.org/10.2151/sola.2017-030.
Ito, T., 2022: Optimal interpolation of global dissolved oxygen: 1965–2015. *Geosci. Data J.*, **9**, 167–176, https://doi.org/10.1002/gdj3.130.
——, S. Minobe, M. C. Long, and C. Deutsch, 2017: Upper ocean O_2 trends: 1958–2015. *Geophys. Res. Lett.*, **44**, 4214–4223, https://doi.org/10.1002/2017GL073613.
——, A. Cervania, K. Cross, S. Ainchwar, and S. Delawalla, 2024: Mapping dissolved oxygen concentrations by combining shipboard and Argo observations using machine learning algorithms. *J. Geophys. Res. Mach. Learn. Comput.*, **1**, e2024JH000272, https://doi.org/10.1029/2024JH000272.
——, and Coauthors, 2025: Assessing the observational uncertainties of dissolved oxygen climatology and seasonal cycle through a coordinated intercomparison project. *Global Biogeochem. Cycles*, **39**, e2025GB008751, https://doi.org/10.1029/2025GB008751.
——, and Coauthors, 2026: Are simulated ocean deoxygenation rates consistent with the observational reconstructions? *Annu. Rev. Earth Planet. Sci.*, **54**, 239–267, https://doi.org/10.1146/annurev-earth-032524-123111.
Jersild, A. J., and P. Landschützer, 2024: A spatially explicit uncertainty analysis of the air-sea CO_2 flux from observations. *Geophys. Res. Lett.*, **51**, e2023GL106636, https://doi.org/10.1029/2023GL106636.
Johns, W. E., S. Elipot, D. A. Smeed, B. I. Moat, B. King, D. L. Volkov, and R. H. Smith, 2023: Towards two decades of Atlantic Ocean mass and heat transports at 26.5°N. Philos. *Trans. Roy. Soc.*, **A381**, 20220188, https://doi.org/10.1098/rsta.2022.0188.
Johnson, G. C., and J. M. Lyman, 2012: Sea surface salinity [in "State of the Climate in 2011"]. *Bull. Amer. Meteor. Soc.*, **93** (7), S68–S69, S72, https://doi.org/10.1175/2012BAMSStateoftheClimate.1.
——, and S. G. Purkey, 2024: Refined estimates of global ocean deep and abyssal decadal warming trends. *Geophys. Res. Lett.*, **51**, e2024GL111229, https://doi.org/10.1029/2024GL111229.
——, and J. M. Lyman, 2025: Sea surface salinity [in "State of the Climate in 2024"]. *Bull. Amer. Meteor. Soc.*, **106** (8), S190–S192, https://doi.org/10.1175/2025BAMSStateoftheClimate.1.
——, ——, J. K. Willis, T. Boyer, J. Antonov, S. A. Good, C. M. Domingues, and N. Bindoff, 2014: Ocean heat content [in "State of the Climate in 2013"]. *Bull. Amer. Meteor. Soc.*, **95** (7), S54–S57, https://doi.org/10.1175/2014BAMSStateoftheClimate.1.

——, and Coauthors, 2015: Ocean heat content [in "State of the Climate in 2014"]. *Bull. Amer. Meteor. Soc.*, **96** (7), S64–S66, S68, https://doi.org/10.1175/2015BAMSStateoftheClimate.1.

——, and Coauthors, 2025: Ocean heat content [in "State of the Climate in 2024"]. *Bull. Amer. Meteor. Soc.*, **106** (8), S186–S190, https://doi.org/10.1175/BAMS-D-25-0074.1.

Kato, S., and Coauthors, 2018: Surface irradiances of edition 4.0 clouds and the Earth's Radiant Energy System (CERES) Energy Balanced and Filled (EBAF) data product. *J. Climate*, **31**, 4501–4527, https://doi.org/10.1175/JCLI-D-17-0523.1.

Keeling, R. F., K. Arne, and N. Gruber, 2010: Ocean deoxygenation in a warming world. *Ann. Rev. Mar. Sci.*, **2**, 199–229, https://doi.org/10.1146/annurev.marine.010908.163855.

Kendon, M., and Coauthors, 2024: State of the UK climate 2023. *Int. J. Climatol.*, **44**, 1–117, https://doi.org/10.1002/joc.8553.

Kennedy, J. J., N. A. Rayner, C. P. Atkinson, and R. E. Killick, 2019: An ensemble data set of sea surface temperature change from 1850: The Met Office Hadley Centre HadSST.4.0.0.0 data set. *J. Geophys. Res. Atmos.*, **124**, 7719–7763, https://doi.org/10.1029/2018JD029867.

Keppler, L., P. Landschützer, S. K., and N. Gruber, 2023: Recent trends and variability in the oceanic storage of dissolved inorganic carbon. *Global Biogeochem. Cycles*, **37**, e2022GB007677, https://doi.org/10.1029/2022GB007677.

Kumar, P., B. Hamlington, S. Cheon, W. Han, and P. Thompson, 2020: 20th century multivariate Indian Ocean regional sea level reconstruction. *J. Geophys. Res. Oceans*, **125**, e2020JC016270, https://doi.org/10.1029/2020JC016270.

Lan, X., and Coauthors, 2023: NOAA greenhouse gas marine boundary layer reference–CO_2. NOAA GML, accessed 30 Jan 2026, https://doi.org/10.15138/DVNP-F961.

Landschützer, P., N. Gruber, D. C. E. Bakker, U. Schuster, S. Nakaoka, M. R. Payne, T. P. Sasse, and J. Zeng, 2013: A neural network-based estimate of the seasonal to inter-annual variability of the Atlantic Ocean carbon sink. *Biogeosciences*, **10**, 7793–7815, https://doi.org/10.5194/bg-10-7793-2013.

——, N. Gruber, D. C. E. Bakker, and U. Schuster, 2014: Recent variability of the global ocean carbon sink. *Global Biogeochem. Cycles*, **28**, 927–949, https://doi.org/10.1002/2014GB004853.

Leuliette, E. W., and J. K. Willis, 2011: Balancing the sea level budget. *Oceanography*, **24** (2), 122–129, https://doi.org/10.5670/oceanog.2011.32.

Leung, S., L. Thompson, M. J. McPhaden, and K. A. S. Mislan, 2019: ENSO drives near-surface oxygen and vertical habitat variability in the tropical Pacific. *Environ. Res. Lett.*, **14**, 064020, https://doi.org/10.1088/1748-9326/ab1c13.

Levin, L. A., 2018: Manifestation, drivers, and emergence of open ocean deoxygenation. *Ann. Rev. Mar. Sci.*, **10**, 229–260, https://doi.org/10.1146/annurev-marine-121916-063359.

Le Vine, D. M., E. P. Dinnat, G. S. E. Lagerloef, P. de Matthaeis, S. Abraham, C. Utku, and H. Kao, 2014: Aquarius: Status and recent results. *Radio Sci.*, **49**, 709–720, https://doi.org/10.1002/2014RS005505.

Levitus, S., and Coauthors, 2012: World ocean heat content and thermosteric sea level change (0–2000 m), 1955–2010. *Geophys. Res. Lett.*, **39**, L10603, https://doi.org/10.1029/2012GL051106.

Li, G., L. Cheng, J. Zhu, K. E. Trenberth, M. E. Mann, and J. P. Abraham, 2020: Increasing ocean stratification over the past half-century. *Nat. Climate Change*, **10**, 1116–1123, https://doi.org/10.1038/s41558-020-00918-2.

Li, L., R. W. Schmitt, C. C. Ummenhofer, and K. B. Karnauskas, 2016: North Atlantic salinity as a predictor of Sahel rainfall. *Sci. Adv.*, **2**, e150158, https://doi.org/10.1126/sciadv.1501588.

Li, S., and Coauthors, 2022: Contributions of different sea-level processes to high-tide flooding along the U.S. Coastline. *J. Geophys. Res. Oceans*, **127**, e2021JC018276, https://doi.org/10.1029/2021JC018276.

Loeb, N. G., and Coauthors, 2018: Clouds and the Earth's Radiant Energy System (CERES) Energy Balanced and Filled (EBAF) Top-of-Atmosphere (TOA) edition-4.0 data product. *J. Climate*, **31**, 895–918, https://doi.org/10.1175/JCLI-D-17-0208.1.

——, G. C. Johnson, T. J. Thorsen, J. M. Lyman, F. G. Rose, and S. Kato, 2021: Satellite and ocean data reveal marked increase in Earth's heating rate. *Geophys. Res. Lett.*, **48**, e2021GL093047, https://doi.org/10.1029/2021GL093047.

——, D. R. Doelling, S. Kato, W. Su, P. E. Mlynczak, and J. C. Wilkins, 2024: Continuity in top-of-atmosphere Earth radiation budget observations. *J. Climate*, **37**, 6093–6108, https://doi.org/10.1175/JCLI-D-24-0180.1.

Long, M. C., C. Deutsch, and T. Ito, 2016: Finding forced trends in oceanic oxygen. *Global Biogeochem. Cycles*, **30**, 381–397, https://doi.org/10.1002/2015GB005310.

Long, X., M. J. Widlansky, F. Schloesser, P. R. Thompson, H. Annamalai, M. A. Merrifield, and H. Yoon, 2020: Higher sea levels at Hawaii caused by strong El Niño and weak trade winds. *J. Climate*, **33**, 3037–3059, https://doi.org/10.1175/JCLI-D-19-0221.1.

Lozier, M. S., and Coauthors, 2017: Overturning in the subpolar North Atlantic program: A new international ocean observing system. *Bull. Amer. Meteor. Soc.*, **98**, 737–752, https://doi.org/10.1175/BAMS-D-16-0057.1.

——, and Coauthors, 2019: A sea change in our view of overturning in the subpolar North Atlantic. *Science*, **363**, 516–521, https://doi.org/10.1126/science.aau6592.

Lu, B., and Coauthors, 2024: OxyGenerator: Reconstructing global ocean deoxygenation over a century with deep learning. *Proceedings of Machine Learning Research*, Vol. 235, PMLR, 33 219–33 242.

Lumpkin, R., G. Goni, and K. Dohan, 2012: Surface currents [in "State of the Climate in 2011"]. *Bull. Amer. Meteor. Soc.*, **93** (7), S75–S78, https://doi.org/10.1175/2012BAMSStateoftheClimate.1.

——, M. Le Hénaff, F. P. Tuchen, and R. C. Perez, 2025: Surface currents [in "State of the Climate in 2024"]. *Bull. Amer. Meteor. Soc.*, **106** (8), S204–S207, https://doi.org/10.1175/BAMS-D-25-0074.1.

Lyman, J. M., and G. C. Johnson, 2014: Estimating global ocean heat content changes in the upper 1800 m since 1950 and the influence of climatology choice. *J. Climate*, **27**, 1946–1958, https://doi.org/10.1175/JCLI-D-12-00752.1.

——, and ——, 2023: Global high-resolution random forest regression maps of ocean heat content anomalies using in situ and satellite data. *J. Atmos. Oceanic Technol.*, **40**, 575–586, https://doi.org/10.1175/JTECH-D-22-0058.1.

Maritorena, S., O. H. F. d'Andon, A. Mangin, and D. A. Siegel, 2010: Merged satellite ocean color data products using a bio-optical model: Characteristics, benefits and issues. *Remote Sens. Environ.*, **114**, 1791–1804, https://doi.org/10.1016/j.rse.2010.04.002.

Maurer, T. L., J. N. Plant, and K. S. Johnson, 2021: Delayed-mode quality control of oxygen, nitrate, and pH data on SOCCOM biogeochemical profiling floats. *Front. Mar. Sci.*, **8**, 683207, https://doi.org/10.3389/fmars.2021.683207.

McCarthy, G. D., G. Hug, D. A. Smeed, K. J. Morris, and B. I. Moat, 2025: Signal and noise in the Atlantic meridional overturning circulation at 26°N. *Geophys. Res. Lett.*, **52**, e2025GL115055, https://doi.org/10.1029/2025GL115055.

McKinna, L. I. W., P. J. Werdell, and C. W. Proctor, 2016: Implementation of an analytical Raman scattering correction for satellite ocean-color processing. *Opt. Express*, **24**, A1123–A1137, https://doi.org/10.1364/OE.24.0A1123.

McPhaden, M. J., K. J. Connell, G. R. Foltz, R. C. Perez, and K. Grissom, 2023: Tropical ocean observations for weather and climate: A decadal overview of the global tropical moored buoy array. *Oceanography*, **36** (2–3), 32–43, https://doi.org/10.5670/oceanog.2023.211.

Minobe, S., 2025: Exceptional heat and basin-scale connections in the Kuroshio–Oyashio region in the early 2020s. *J. Oceanogr.*, **81**, 443–461, https://doi.org/10.1007/s10872-025-00764-w.

Mishonov, A. V., and Coauthors, 2024: World Ocean Database 2023. NOAA Atlas NESDIS 97, accessed 11 January 2026, https://doi.org/10.25923/Z885-H264.

Moat, B. I., and Coauthors, 2026: Atlantic meridional overturning circulation observed by the RAPID-MOCHA-WBTS (RAPID-Meridional Overturning Circulation and Heatflux Array-Western Boundary Time Series) array at 26N from 2004 to 2024 (v2024.1a). British Oceanographic Data Centre–Natural Environment Research Council, accessed 13 January 2026, https://doi.org/10.5285/48d0bf43-0598-ceb2-e063-7086abc062f1.

Mulet, S., and Coauthors, 2021: The new CNES-CLS18 global mean dynamic topography. *Ocean Sci.*, **17**, 789–808, https://doi.org/10.5194/os-17-789-2021.

Müller, J. D., and Coauthors, 2025: Unexpected decline in the ocean carbon sink under record-high sea surface temperatures in 2023. *Nat. Climate Change*, **15**, 978–985, https://doi.org/10.1038/s41558-025-02380-4.

Nerem, R. S., B. D. Beckley, J. T. Fasullo, B. D. Hamlington, D. Masters, and G. T. Mitchum, 2018: Climate-change–driven accelerated sea-level rise detected in the altimeter era. *Proc. Natl. Acad. Sci. USA*, **115**, 2022–2025, https://doi.org/10.1073/pnas.1717312115.

NOAA Climate Prediction Center, 2026: Indian Ocean monitoring and forecasting. Accessed 28 January 2026, https://www.cpc.ncep.noaa.gov/products/international/ocean_monitoring/indian/IO_monitoring_fcsts/io_index.shtml.

NOAA NCEI, 2026: Climate monitoring: Pacific Decadal Oscillation (PDO). Accessed 28 January 2026, https://www.ncei.noaa.gov/access/monitoring/pdo/.

Oliver, E. C. J., J. A. Benthuysen, S. Darmaraki, M. G. Donat, A. J. Hobday, N. J. Holbrook, R. W. Schlegel, and A. Sen Gupta, 2021: Marine heatwaves. *Ann. Rev. Mar. Sci.*, **13**, 313–342, https://doi.org/10.1146/annurev-marine-032720-095144.

O'Reilly, J. E., and P. J. Werdell, 2019: Chlorophyll algorithms for ocean color sensors–OC4, OC5 & OC6. *Remote Sens. Environ.*, **229**, 32–47, https://doi.org/10.1016/j.rse.2019.04.021.

Oschlies, A., O. Duteil, J. Getzlaff, W. Koeve, A. Landolfi, and S. Schmidtko, 2017: Patterns of deoxygenation: Sensitivity to natural and anthropogenic drivers. *Philos. Trans. Roy. Soc.*, **A375**, 20160325, https://doi.org/10.1098/rsta.2016.0325.

——, P. Brandt, L. Stramma, and S. Schmidtko, 2018: Drivers and mechanisms of ocean deoxygenation. *Nat. Geosci.*, **11**, 467–473, https://doi.org/10.1038/s41561-018-0152-2.

Palmer, M. D., K. Haines, S. F. B. Tett, and T. J. Ansell, 2007: Isolating the signal of ocean global warming. *Geophys. Res. Lett.*, **34**, L23610, https://doi.org/10.1029/2007GL031712.

Pan, Y., and Coauthors, 2026: Ocean heat content sets another record in 2025. *Adv. Atmos. Sci.*, https://doi.org/10.1007/s00376-026-5876-0, in press.

Parouffe, A., B. Dewitte, A. Paulmier, and V. Garçon, 2025: ENSO modulates aerobic habitat across varying hypoxia tolerance levels in the southeast Pacific throughout the twenty-first century. *Sci. Rep.*, **15**, 20670, https://doi.org/10.1038/s41598-025-06498-5.

Petit, T., J. Robson, D. Ferreira, S. Yeager, and D. G. Evans, 2025a: Coherence of the AMOC over the subpolar North Atlantic on interannual to multiannual time scales. *Geophys. Res. Lett.*, **52**, e2025GL115171, https://doi.org/10.1029/2025GL115171.

——, and Coauthors, 2025b: Evaluation of a reduced RAPID array for measuring the AMOC. *J. Geophys. Res. Oceans*, **130**, e2025JC023093, https://doi.org/10.1029/2025JC023093.

Purkey, S. G., and G. C. Johnson, 2010: Warming of global abyssal and deep Southern Ocean waters between the 1990s and 2000s: Contributions to global heat and sea level rise budgets. *J. Climate*, **23**, 6336–6351, https://doi.org/10.1175/2010JCLI3682.1.

Qiu, B., and S. Chen, 2021: Revisit of the occurrence of the Kuroshio large meander south of Japan. *J. Phys. Oceanogr.*, **51**, 3679–3694, https://doi.org/10.1175/JPO-D-21-0167.1.

——, S. Chen, N. Schneider, E. Oka, and S. Sugimoto, 2020: On the reset of the wind-forced decadal Kuroshio extension variability in late 2017. *J. Climate*, **33**, 10?813–10?828, https://doi.org/10.1175/JCLI-D-20-0237.1.

Rahmstorf, S., J. E. Box, G. Feulner, M. E. Mann, A. Robinson, S. Rutherford, and E. J. Schaffernicht, 2015: Exceptional twentieth-century slowdown in Atlantic Ocean overturning circulation. *Nat. Climate Change*, **5**, 475–480, https://doi.org/10.1038/nclimate2554.

Randolph, K., H. M. Dierssen, M. Twardowski, A. Cifuentes-Lorenzen, and C. J. Zappa, 2014: Optical measurements of small deeply penetrating bubble populations generated by breaking waves in the Southern Ocean. *J. Geophys. Res. Oceans*, **119**, 757–776, https://doi.org/10.1002/2013JC009227.

Rayner, N. A., and Coauthors, 2003: Global analyses of sea surface temperature, sea ice, and night marine air temperature since the late nineteenth century. *J. Geophys. Res.*, **108**, 4407, https://doi.org/10.1029/2002JD002670.

Reagan, J., C. Schmid, and R. Locarnini, 2025: Subsurface salinity [in "State of the Climate in 2024"]. *Bull. Amer. Meteor. Soc.*, **106** (8), S192–S194, https://doi.org/10.1175/BAMS-D-25-0074.1.

Reagan, J. R., and Coauthors, 2024: *Salinity*. Vol. 2, *World Ocean Atlas 2023*. A. Mishonov, Ed., NOAA Atlas NESDIS 90, 52 pp., https://doi.org/10.25923/70qt-9574.

——, and Coauthors, 2024: World Ocean Atlas 2023 (NCEI Accession 0270533). NOAA National Centers for Environmental Information, https://www.ncei.noaa.gov/archive/accession/0270533.

Regnier, P., L. Resplandy, R. G. Najjar, and P. Ciais, 2022: The land-to-ocean loops of the global carbon cycle. *Nature*, **603**, 401–410, https://doi.org/10.1038/s41586-021-04339-9.

Ren, L., K. Speer, and E. P. Chassignet, 2011: The mixed layer salinity budget and sea ice in the Southern Ocean. *J. Geophys. Res.*, **116**, C08031, https://doi.org/10.1029/2010JC006634.

Rhein, M., R. Steinfeldt, D. Kieke, I. Stendardo, and I. Yashayaev, 2017: Ventilation variability of Labrador Sea Water and its impact on oxygen and anthropogenic carbon: A review. *Philos. Trans. Roy. Soc.*, **A375**, 20160321, https://doi.org/10.1098/rsta.2016.0321.

Rio, M. H., S. Mulet, and N. Picot, 2014: Beyond GOCE for the ocean circulation estimate: Synergetic use of altimetry, gravimetry, and in situ data provides new insight into geostrophic and Ekman currents. *Geophys. Res. Lett.*, **41**, 8918–8925, https://doi.org/10.1002/2014GL061773.

Riser, S. C., and Coauthors, 2016: Fifteen years of ocean observations with the global Argo array. *Nat. Climate Change*, **6**, 145–153, https://doi.org/10.1038/nclimate2872.

Roach, C. J., and N. L. Bindoff, 2023: Developing a new oxygen atlas of the world's oceans using data interpolating variational analysis. *J. Atmos. Oceanic Technol.*, **40**, 1475–1491, https://doi.org/10.1175/JTECH-D-23-0007.1.

Rödenbeck, C., and Coauthors, 2015: Data-based estimates of the ocean carbon sink variability—First results of the Surface Ocean $p\mathrm{CO_2}$ Mapping intercomparison (SOCOM). *Biogeosciences*, **12**, 7251–7278, https://doi.org/10.5194/bg-12-7251-2015.

Roemmich, D., and J. Gilson, 2009: The 2004–2008 mean and annual cycle of temperature, salinity, and steric height in the global ocean from the Argo program. *Prog. Oceanogr.*, **82**, 81–100, https://doi.org/10.1016/j.pocean.2009.03.004.

——, and Coauthors, 2019: On the future of Argo: A global, full-depth, multi-disciplinary array. *Front. Mar. Sci.*, **6**, 439, https://doi.org/10.3389/fmars.2019.00439.

Schlegel, R. W., S. Darmaraki, J. A. Benthuysen, K. Filbee-Dexter, and E. C. Oliver, 2021: Marine cold-spells. *Prog. Oceanogr.*, **198**, 102684, https://doi.org/10.1016/j.pocean.2021.102684.

Schlesinger, M. E., and N. Ramankutty, 1994: An oscillation in the global climate system of period 65–70 years. *Nature*, **367**, 723–726, https://doi.org/10.1038/367723a0.

Schmidtko, S., G. C. Johnson, and J. M. Lyman, 2013: MIMOC: A global monthly isopycnal upper?ocean climatology with mixed layers. *J. Geophys. Res. Oceans*, **118**, 1658–1672, https://doi.org/10.1002/jgrc.20122.

——, L. Stramma, and M. Visbeck, 2017: Decline in global oceanic oxygen content during the past five decades. *Nature*, **542**, 335–339, https://doi.org/10.1038/nature21399.

Schmitt, R. W., 1995: The ocean component of the global water cycle. *Rev. Geophys.*, **33**, 1395–1409, https://doi.org/10.1029/95RG00184.

Shao, W. Z., S. J. Leng, Q. Zhang, and X. W. Jiang, 2025: A potential technique for SAR ocean surface current speed retrieval based on machine learning. *Eur. J. Remote Sens.*, **58**, 2600152, https://doi.org/10.1080/22797254.2025.2600152.

Sharp, J. D., A. J. Fassbender, B. R. Carter, G. C. Johnson, C. Schultz, and J. P. Dunne, 2023: GOBAI-O 2: Temporally and spatially resolved fields of ocean interior dissolved oxygen over nearly 2 decades. *Earth Syst. Sci. Data*, **15**, 4481–4518, https://doi.org/10.5194/essd-15-4481-2023.

Siegel, D. A., and Coauthors, 2013: Regional to global assessments of phytoplankton dynamics from the SeaWiFS mission. *Remote Sens. Environ.*, **135**, 77–91, https://doi.org/10.1016/j.rse.2013.03.025.

——, T. DeVries, I. Cetinić, and K. M. Bisson, 2023: Quantifying the ocean's biological pump and its carbon cycle impacts on global scales. *Ann. Rev. Mar. Sci.*, **15**, 329–356, https://doi.org/10.1146/annurev-marine-040722-115226.

Skliris, N., R. Marsh, S. A. Josey, S. A. Good, C. Liu, and R. P. Allan, 2014: Salinity changes in the world ocean since 1950 in relation to changing surface freshwater fluxes. *Climate Dyn.*, **43**, 709–736, https://doi.org/10.1007/s00382-014-2131-7.

Smeed, D. A., and Coauthors, 2026: Overturning circulation of the North Atlantic subtropical gyre computed in density coordinates at 26°N. *Geophys. Res. Lett.*, **53**, e2025GL118277, https://doi.org/10.1029/2025GL118277.

Stackhouse, P. W., D. P. Kratz, G. R. McGarragh, S. K. Gupta, and E. B. Geier, 2006: Fast Longwave and Shortwave Radiative Flux (FLASHFlux) products from CERES and MODIS measurements. *12th Conf. on Atmospheric Radiation*, Madison, WI, Amer. Meteor. Soc., P1.10, https://ntrs.nasa.gov/api/citations/20060028146/downloads/20060028146.pdf.

Stoer, A. C., and K. Fennel, 2024: Carbon-centric dynamics of Earth's marine phytoplankton. *Proc. Natl. Acad. Sci. USA*, **121**, e2405354121, https://doi.org/10.1073/pnas.2405354121.

Stramma, L., and Coauthors, 2012: Expansion of oxygen minimum zones may reduce available habitat for tropical pelagic fishes. *Nat. Climate Change*, **2**, 33–37, https://doi.org/10.1038/nclimate1304.

Sun, K., J. Liang, X. M. Li, and J. Pan, 2025: Retrieval of ocean surface currents by synergistic Sentinel-1 and SWOT data using deep learning. *Remote Sens.*, **17**, 2133, https://doi.org/10.3390/rs17132133.

Sweet, W. V., J. Park, J. J. Marra, C. Zervas, and S. Gill, 2014: Sea level rise and nuisance flood frequency changes around the United States. NOAA Tech. Rep. NOS CO-OPS 73, 66 pp.

——, A. S. Genz, M. Menendez, J. J. Marra, and J. Obeysekera, 2024: Implications of variability and trends in coastal extreme water levels. *Geophys. Res. Lett.*, **51**, e2024GL108864, https://doi.org/10.1029/2024GL108864.

Tamisiea, M. E., and J. X. Mitrovica, 2011: The moving boundaries of sea level change: Understanding the origins of geographic variability. *Oceanography*, **24** (2), 24–39, https://doi.org/10.5670/oceanog.2011.25.

Tan, W., Z-Z Hu, Y. Liu, and M. J. McPhaden, 2025: Evolution and prediction of the La Niña conditions in 2024/25. *Environ. Res. Commun.*, **7**, 125031, https://doi.org/10.1088/2515-7620/ae2e97.

Tuchen, F. P., 2025: The return of equatorial Atlantic extreme events. *CLIVAR Exchanges*, No. 84, International CLIVAR Project Office, Southampton, United Kingdom, 26–30, https://doi.org/10.36071/clivar.84.2025.

——, and Coauthors, 2025: Record warmth and unprecedented drop in equatorial Atlantic sea surface temperatures in 2024. *Geophys. Res. Lett.*, **52**, e2025GL115973, https://doi.org/10.1029/2025GL115973.

Twedt, K., N. Lei, X. Xiong, A. Angal, S. Li, T. Chang, and J. Sun, 2022: On-orbit calibration and performance of NOAA-20 VIIRS reflective solar bands. *IEEE Trans. Geosci. Remote Sens.*, **60**, 1–13, https://doi.org/10.1109/TGRS.2021.3108970.

Volkov, D. L., R. H. Smith, R. F. Garcia, D. A. Smeed, B. I. Moat, W. E. Johns, and M. O. Baringer, 2024: Florida current transport observations reveal four decades of steady state. *Nat. Commun.*, **15**, 7780, https://doi.org/10.1038/s41467-024-51879-5.

——, and Coauthors, 2025a: Meridional overturning circulation and heat transport in the Atlantic Ocean [in "State of the Climate in 2024"]. *Bull. Amer. Meteor. Soc.*, **106** (8), S208–2010, https://doi.org/10.1175/BAMS-D-25-0074.1.

——, R. H. Smith, and R. F. Garcia, 2025b: Pressure gauges and satellite altimetry ensure the continuity of Florida current transport observations. *Geophys. Res. Lett.*, **52**, e2025GL115897, https://doi.org/10.1029/2025GL115897.

von Schuckmann, K., and Coauthors, 2023: Heat stored in the Earth system 1960–2020: Where does the energy go? *Earth Syst. Sci. Data*, **15**, 1675–1709, https://doi.org/10.5194/essd-15-1675-2023.

Von Storch, H., and F. W. Zwiers, 1999: *Statistical Analysis in Climate Research*. Cambridge University Press, 484 pp.

Wahl, T., F. M. Calafat, and M. E. Luther, 2014: Rapid changes in the seasonal sea level cycle along the US Gulf Coast from the late 20th century. *Geophys. Res. Lett.*, **41**, 491–498, https://doi.org/10.1002/2013GL058777.

Walsh, K. J. E., and Coauthors, 2016: Tropical cyclones and climate change. *Wiley Interdiscip. Rev.: Climate Change*, **7**, 65–89, https://doi.org/10.1002/wcc.371.

Wang, Z., and Coauthors, 2025: Bias evaluation for sensor-based dissolved oxygen from CTD and profiling floats in the world ocean database. *J. Atmos. Oceanic Technol.*, **42**, 1263–1280, https://doi.org/10.1175/JTECH-D-25-0027.1.

Wanninkhof, R., 2014: Relationship between wind speed and gas exchange over the ocean revisited. *Limnol. Oceanogr. Methods*, **12**, 351–362, https://doi.org/10.4319/lom.2014.12.351.

——, J. Triñanes, D. Pierrot, D. R. Munro, C. Sweeney, and A. R. Fay, 2025: Trends in sea-air CO_2 fluxes and sensitivities to atmospheric forcing using an extremely randomized trees machine learning approach. *Global Biogeochem. Cycles*, **39**, e2024GB008315, https://doi.org/10.1029/2024GB008315.

Weijer, W., W. Cheng, O. A. Garuba, A. Hu, and B. T. Nadiga, 2020: CMIP6 models predict significant 21st century decline of the Atlantic meridional overturning circulation. *Geophys. Res. Lett.*, **47**, e2019GL086075, https://doi.org/10.1029/2019GL086075.

Werdell, P. J., and L. I. Mckinna, 2019: Sensitivity of inherent optical properties from ocean reflectance inversion models to satellite instrument wavelength suites. *Front. Earth Sci.*, **7**, 54, https://doi.org/10.3389/feart.2019.00054.

——, and Coauthors, 2013: Generalized ocean color inversion model for retrieving marine inherent optical properties. *Appl. Opt.*, **52**, 2019–2037, https://doi.org/10.1364/AO.52.002019.

Westberry, T. K., P. Schultz, M. J. Behrenfeld, J. P. Dunne, M. R. Hiscock, S. Maritorena, J. L. Sarmiento, and D. A. Siegel, 2016: Annual cycles of phytoplankton biomass in the subarctic Atlantic and Pacific Ocean. *Global Biogeochem. Cycles*, **30**, 175–190, https://doi.org/10.1002/2015GB005276.

Widlansky, M. J., A. Timmermann, S. McGregor, M. F. Stuecker, and W. Cai, 2014: An interhemispheric tropical sea level seesaw due to El Niño Taimasa. *J. Climate*, **27**, 1070–1081, https://doi.org/10.1175/JCLI-D-13-00276.1.

——, ——, and W. Cai, 2015: Future extreme sea level seesaws in the tropical Pacific. *Sci. Adv.*, **1**, e1500560, https://doi.org/10.1126/sciadv.1500560.

Wiese, D. N., D.-N. Yuan, C. Boening, F. W. Landerer, and M. M. Watkins, 2022: JPL GRACE and GRACE-FO Mascon Ocean, ice, and hydrology equivalent HDR water height RL06.1M CRI filtered version 3.0. PO.DAAC, accessed 13 February 2024, https://doi.org/10.5067/TEMSC-3MJ62.

Willis, J., and W. Hobbs, 2026: Atlantic meridional overturning circulation near 41N from altimetry and Argo observations. Zenodo, accessed 15 Mar 2026, https://zenodo.org/records/18238115.

Willis, J. K., 2010: Can in situ floats and satellite altimeters detect long-term changes in Atlantic Ocean overturning? *Geophys. Res. Lett.*, **37**, L06602, https://doi.org/10.1029/2010GL042372.

——, B. D. Hamlington, and S. Fournier, 2025: Global mean sea level time series, trajectory and extrapolation. Accessed 4 February 2026, https://doi.org/10.5281/zenodo.18649998.

WOD Team, 2025: World Ocean Database data product series. NOAA NCEI, accessed 15 January 2026, https://doi.org/10.25921/v92s-y066.

Wolter, K., and M. S. Timlin, 1998: Measuring the strength of ENSO events: How does 1997/98 rank? *Weather*, **53**, 315–324, https://doi.org/10.1002/j.1477-8696.1998.tb06408.x.

Wong, A. P. S., J. Gilson, and C. Cabanes, 2023: Argo salinity: Bias and uncertainty evaluation. *Earth Syst. Sci. Data*, **15**, 383–393, https://doi.org/10.5194/essd-15-383-2023.

Woodworth, P. L., and Coauthors, 2019: Forcing factors affecting sea level changes at the coast. *Surv. Geophys.*, **40**, 1351–1397, https://doi.org/10.1007/s10712-019-09531-1.

Wüst, G., 1936: Oberflächensalzgehalt, Verdunstung und Niederschlag auf dem Weltmeere. *Länderkundliche Forschung: Festschrift zur Vollendung des sechzigsten Lebensjahres Norbert Krebs*, J. Engelhorns, 347–359.

Xie, P., and Coauthors, 2014: An in situ-satellite blended analysis of global sea surface salinity. *J. Geophys. Res. Oceans*, **119**, 6140–6160, https://doi.org/10.1002/2014JC010046.

Xing, Q., S. Elipot, W. E. Johns, D. A. Smeed, B. I. Moat, and J. W. Loder, 2026: Meridionally consistent decline in the observed western boundary contribution to the Atlantic meridional overturning circulation. *Sci. Adv.*, **12**, eadz7738, https://doi.org/10.1126/sciadv.adz7738.

Yin, X., B. Huang, J. A. Carton, L. Chen, G. Graham, C. Liu, T. Smith, and H.-M. Zhang, 2024: The 1991–2020 sea surface temperature normals. *Int. J. Climatol.*, **44**, 668–685, https://doi.org/10.1002/joc.8350.

Yu, L., 2011: A global relationship between the ocean water cycle and near-surface salinity. *J. Geophys. Res.*, **116**, C10025, https://doi.org/10.1029/2010JC006937.

——, 2019: Global air–sea fluxes of heat, fresh water, and momentum: Energy budget closure and unanswered questions. *Annu. Rev. Mar. Sci.*, **11**, 227–248, https://doi.org/10.1146/annurev-marine-010816-060704.

——, and R. A. Weller, 2007: Objectively analyzed air–sea heat fluxes for the global ice-free oceans (1981–2005). *Bull. Amer. Meteor. Soc.*, **88**, 527–540, https://doi.org/10.1175/BAMS-88-4-527.

Zhou, Y., H. Gong, and F. Zhou, 2022: Responses of horizontally expanding oceanic oxygen minimum zones to climate change based on observations. *Geophys. Res. Lett.*, **49**, e2022GL097724, https://doi.org/10.1029/2022GL097724]